

University of Nottingham
UK | CHINA | MALAYSIA

Magnetoencephalographic dynamics and adaptive brain networks across multiple timescales

Kanad Mandke, MSc

A thesis submitted to the School of Psychology, University of Nottingham, in partial fulfilment of the requirements for the degree of Doctor of Philosophy

November 2019.

*Stay at the wicket and runs will come! **

** The origins of this quote, to the best of my knowledge, remain unknown. Legendary cricketers including Vijay Merchant and Sunil Gavaskar have been attributed to it, but I have mostly heard it from my father, an avid cricket fan. In the most difficult of times during this Ph.D., these words have provided me with the necessary reassurance.*

For Aaji

TABLE OF CONTENTS

Table of contents iii

Abstract viii

Acknowledgements: Funding, data, and declaration x

Thesis contributions xi

Personal acknowledgements xiii

Chapter 1 1

1 General introduction and thesis overview 1

1.1 Introduction *1*

1.2 Scales of measurement and MEG *4*

1.3 Aims and objectives *5*

1.4 Thesis overview *7*

Chapter 2 9

2 MEG: Neurophysiological origins and instrumentation 9

Précis *9*

2.1 Anatomy and physiology of neurons *9*

2.1.1 Laminar organisation: Cortical subdivisions 12

2.2 Neuronal communication *14*

2.2.1 Resting membrane potential 14

2.2.2 Action potential (AP) 15

2.2.3 Postsynaptic potentials (PSP) 16

2.3 MEG signals: Origins *18*

2.3.1 What can we measure using MEG? 19

2.4 Instrumentation: MEG *23*

Chapter 3 **30**

3 Source analysis of MEG data **30**

Précis *30*

3.1 Introduction *30*

3.2 Forward problem *31*

3.3 Inverse problem *32*

3.3.1 Beamforming 33

Chapter 4 **38**

4 Prefrontal theta and alpha power increases to attended auditory oddballs **38**

Précis *38*

4.1 Introduction *39*

4.2 Methods *42*

4.2.1 Participants 42

4.2.2 Stimuli and experimental task 42

4.2.3 Data acquisition 43

4.2.4 Data analysis 43

4.2.5 Source reconstruction using beamforming 44

4.3 Results *47*

4.3.1 Sensor level analysis 47

4.3.2 Source analysis: N100 latency window 49

4.3.3 Source analysis: P300 latency window 53

4.4 Discussion *57*

4.4.1 Frontal ERS responses to oddballs 57

4.4.2 Theta and alpha band components 58

4.4.3 Time- (Phase-) locked responses 59

4.4.4 Processes underlying P300 60

Chapter 5 **62**

5 From functional connectivity to multilayer networks **62**

Précis *62*

5.1 Estimating functional connectivity *62*

5.1.1 Signal leakage 63

5.1.2 Amplitude envelope correlation 65

5.2 Primer on graph theory *67*

5.3 Extracting functional brain networks *70*

5.3.1 Defining nodes of the network 71

5.3.2 Identifying relationships between the nodes 72

5.3.3 Representing a graph 72

5.3.4 Quantifying the network behaviour 73

5.4 Graph metrics *74*

5.4.1 Degree 74

5.4.2 Path length 74

5.4.3 Clustering coefficient 75

5.4.4 Small worldness 75

5.4.5 Betweenness centrality 76

5.5 Towards an integrative approach *77*

5.6 Primer on multilayer networks *78*

5.7 Quantifying multilayer networks: Multilayer graph metrics *79*

5.7.1 Distance class metrics 81

5.7.2 Connection class metrics 81

5.7.3 Spectral class metrics 85

5.7.4 Between layer dependency 86

5.8 Generative models for multilayer networks *88*

5.8.1 Non-linear preferential attachment for multilayer networks 88

5.8.2 Synthetic multilayer community networks 89

Chapter 6 **90**

6 Comparing multilayer brain networks between groups **90**

Précis *90*

6.1 Introduction *91*

6.2 Methods *93*

6.2.1 Empirical MEG and fMRI networks 93

6.3 Schemes for the correction of network biases *96*

6.3.1 MST 97

6.3.2 ECO 98

6.3.3 Effective graph resistance cost minimisation 98

6.3.4 SVD normalisation 99

6.4 Results *101*

6.4.1 Uncorrected multilayer networks are affected by average link weight or link density 101

6.4.2 Applying correction schemes to multilayer networks as a whole 102

6.4.3 Applying correction schemes to individual layers in multilayer networks 104

6.4.4 Nodal community assignment in multilayer networks after applying correction schemes 105

6.4.5 Sensitivity to genuine alterations in multilayer network organisation – correction applied to multilayer networks as a whole 106

6.4.6 Sensitivity to genuine alterations in multilayer network organisation – correction applied to individual layers in multilayer networks 109

6.4.7 Sensitivity for identification of group differences 111

6.5 Discussion *113*

6.5.1 Further discussion on methodological choices and findings 116

Chapter 7 **120**

7 Musical training-related differences in brain's resting state **120**

Précis *120*

7.1 Introduction *121*

7.2 Methods *124*

7.2.1 Participants and MEG data pre-processing 124

7.2.2 Source localisation using an atlas based beamformer 125
7.2.3 Functional connectivity calculation 126
7.2.4 Single-layer analysis using Network-Based Statistics 127
7.2.5 Multilayer network construction 128
7.2.6 Graph analysis of multilayer networks 130

7.3 Results *133*

7.3.1 Functional connectivity and Network Based Statistics 133
7.3.2 Graph analysis of the multilayer networks 135

7.4 Discussion *139*

7.4.1 Methodological considerations for multilayer networks (interlayer coupling) 143
7.4.2 Conclusion 144

Chapter 8 **146**

8 Concluding remarks and future directions **146**

8.1 General discussion and future directions *146*

8.1.1 MEG for cortical dynamics at multiple time scales 146
8.1.2 Network neuroscience-based biomarkers 149

9 Appendix **154**

9.1 Appendix to chapter 7 – Degree correlations *156*

List of figures **160**

List of tables **167**

References **168**

ABSTRACT

The human brain is a complex network of interconnected neurons which function on various scales of time and space. The observable behaviour produced by the human brain is the result of a cascade of several neuronal events that occur over a wide temporal scale. The project investigated processes near the two ends of the temporal scale using magnetoencephalography (MEG), a non-invasive neuroimaging method with high temporal resolution.

As an example of temporal dynamics over the millisecond scale, auditory event-related responses were investigated. To this end, MEG data were recorded as participants performed an auditory oddball task. The data were analysed using Linearly Constrained Minimum Variance beamformer, applied to study non-phase-locked and phase-locked event-related responses. Neuronal sources of sensory-evoked responses, corresponding to phase-locked and non-phase-locked responses, were localised in the bilateral primary auditory cortices and auditory belt area. Whereas, neuronal sources of late, cognitive responses (occurring 300ms after stimulus onset) were localised in modality specific and supra-modal areas, such as the temporo-parietal junction, inferior frontal gyrus, and prefrontal cortex.

As an example of dynamics over years, the project searched for changes in the organisation of brain networks following years of musical training. This research question required the development of a novel method based on graph theory and in particular, the multilayer network framework. This framework treats the human brain as a "network of networks", allowing us to integrate information from different MEG frequency bands (or imaging modalities) in a unified network description. The central contribution from this thesis is the development of a normalisation method, which allows us to perform multilayer network group comparisons (such as control group vs experimental/clinical group). The efficacy of this method was tested by using simulated brain networks as ground truth.

Subsequently, using the newly developed method, the effects of training related plasticity were investigated in resting-state MEG recordings, without a task requiring the trained skill. Here, we identified that musicians show an integrated network configuration when compared with non-musicians. Furthermore, it was also

demonstrated that multilayer networks provide information that more traditional approaches of network analysis cannot, highlighting the benefits of multilayer network analysis in between-group studies.

The thesis concludes with a general discussion on how the multilayer network framework can potentially be used further for studies of cortical dynamics, specifically, multimodal data integration to obtain a holistic picture of the human brain.

ACKNOWLEDGEMENTS: FUNDING, DATA, AND DECLARATION

First and foremost, I would like to thank the University of Nottingham for awarding me the Vice Chancellor's scholarship, the work that I have undertaken in the last four years would not have been possible without the generous financial support.

The data used in **Chapter 6** were collected as part of the University of Nottingham Multimodal Imaging Study in Psychosis, funded by the Medical Research Council (MR/J01186X/1). I, therefore, express my thanks to all those involved in data collection, particularly Dr. Emma Hall, Dr. Sian Robson, and Dr. Jyothika Kumar. I would also like to thank Dr. Prejaas Tewarie for making this data available to me.

The data used in **Chapter 7** are available as part of the Open MEG Archive (Niso et al., 2016).

This thesis is the candidate's own work, and has not, in the same or different form been submitted to this or any other University for a degree.

This candidate performed all the data analysis.

THESIS CONTRIBUTIONS

Conference presentations –

BACN, Budapest, 2016

Mandke, K., O'Neill, G., Adjamian, P., Schürmann, M. Prefrontal oscillatory responses in auditory oddball task. F1000Research 2018, 7:265 (poster) (doi: 10.7490/f1000research.1115288.1)

MEG-UK, York, 2016

Mandke, K., O'Neill, G., Tewarie, P., Adjamian, P., Schürmann, M. MEG signatures of auditory change detection. F1000Research 2018, 7:266 (poster) (doi: 10.7490/f1000research.1115289.1)

MEG-Nord, Aarhus, Denmark (2017)

Mandke, K., Brookes, M. J., Hillebrand, A., Meier, J., O'Dea, R., Van Mieghem, P., F., Stam, C., J., Tewarie, P. Comparing multilayer brain networks between groups. F1000Research 2018, 7:264. (poster) (doi: 10.7490/f1000research.1115287.1)

Publication(s) –

See chapter 4

Mandke, K., Adjamian, P., Schürmann, M. Prefrontal theta and alpha power increases in neuro-magnetic responses to attended auditory oddballs (in prep).

See chapter 5 and 6

Mandke, K., Meier, J., Brookes, M. J., O'Dea, R. D., Van Mieghem, P., Stam, C. J., Hillebrand, A., Tewarie, P. (2018). Comparing multilayer brain networks between groups: Introducing graph metrics and recommendations. NeuroImage, 166, 371–384. https://doi.org/10.1016/j.neuroimage.2017.11.016

See chapter 7

Mandke, K., Tewarie, P., Adjamian, P., Meier, J., Schürmann, M. Musical training related differences in brain's resting state: Multilayer network analysis of MEG data (under revision).

PERSONAL ACKNOWLEDGEMENTS

I would like to sincerely thank my primary supervisor Dr Martin Schürmann for his constant support throughout my PhD. Thank you for giving me the independence and freedom to pursue various ideas at my own pace, sometimes, however slow that might have been. I am also grateful to my secondary supervisor Dr Peyman Adjamian, for offering timely practical advice on many things and also continually reminding me to keep an eye on the "big picture".

Beyond my supervisory team, I am forever indebted to three key individuals – Dr George O'Neill, Dr Prejaas Tewarie and, Dr Jil Meier.

George, thanks for all the technical help and snippets of code, especially in the early days of my PhD

Prejaas, thanks a lot for introducing me to the world of network science and never saying no to a healthy debate/discussion on neuroscience, religion, politics and pretty much anything (which often followed with locally sourced Thai food). You have been a great role model!

Jil, while we don't work in the same lab, thanks for taking an interest in my projects, verifying some of my codes and also for your timely comments on our papers. I hope this is just the beginning of a long, productive collaborative work.

The three of you are incredible scientists!

Thanks, are also due to my wonderful friends, Sarah, Becca, Richard, Hilmar, Giuliano, Miguel, Luke who made coming in to work so much fun and making Nottingham, my second home. 12 pm lunch will never be the same without you two, Sarah and Becca! I am incredibly lucky to have met all of you.

At this stage, Geoffrey Chapman deserves a special mention. Thanks for being the greatest friend and always being available to listen to my rants. I will forever cherish our conversations over countless coffees, beers, whiskeys, and cricket matches (not necessarily in the same order).

I also thank Vikram Sampath for insightful non-thesis related discussions and invaluable advice on writing.

I would not be here if it were not for the unwavering support and encouragement from my parents, my grandmother, Aniruddha, Manisha, and Anvika. Thanks for continually pushing me to aim higher. The occasional care packages of home-cooked food and our Sunday skype calls have made all the difference.

Finally, Snigdha, thanks for keeping me grounded. Throughout the last four years, you have provided me with nothing but unconditional love and support. Thanks especially for your support and understanding in the last year of thesis writing, when I was almost certain I would give up.

I could not have done this without any of you.

CHAPTER 1

1 General introduction and thesis overview

1.1 Introduction

The average human brain is about 2% of the total body weight, and yet it consumes 20% of the total glucose uptake. The brain houses over a billion neurons and a trillion synapses making it the most complex systems known to us. However, how does this organ produce observable and adaptive behaviour remains a mystery. Neuroscience, i.e., the scientific study of the nervous system, is a multidisciplinary branch of science that attempts to address some of these questions. The last three decades, in particular, have seen exponential growth in the number of publications that are involved in the investigation of various aspects of the nervous system (**Figure 1-1**). These investigations range from microscopic to macroscopic levels of the human and animal nervous system. Having said that, the interest in the functioning of the human brain is hardly a recent one. The oldest reports date back to ancient Egypt, the *Edwin Smith Papyrus*, an Egyptian medical text, which provides evidence that Egyptians used various surgical procedures to cure ailments of the head (Mohamed, 2008). Furthermore, the ancient Egyptians used the human heart and mind synonymously and believed that depression was a "fever in the heart" (Mohamed, 2008). Fast-forwarding to the present day, our understanding of the human brain has become far more sophisticated. We now know various underlying physiological and anatomical principles, and we most certainly do not believe that the heart is the centre of "mind."

The foundations of modern neuroscience were laid by the heated debate[1] between Santiago Ramon y Cajal and Camillo Golgi at the turn of the 20th century. In the late

1 Golgi and Cajal shared the Nobel Prize in 1906. The transcripts of their Nobel Prize lectures offer an entertaining summary of this debate.

1800s, Golgi developed a silver staining method using which he proposed the reticular theory. From his initial observations, he stated that the neurons in the brain appear to have long processes, which form a continuous web, known as the reticulum, that is responsible for the neuronal communication.

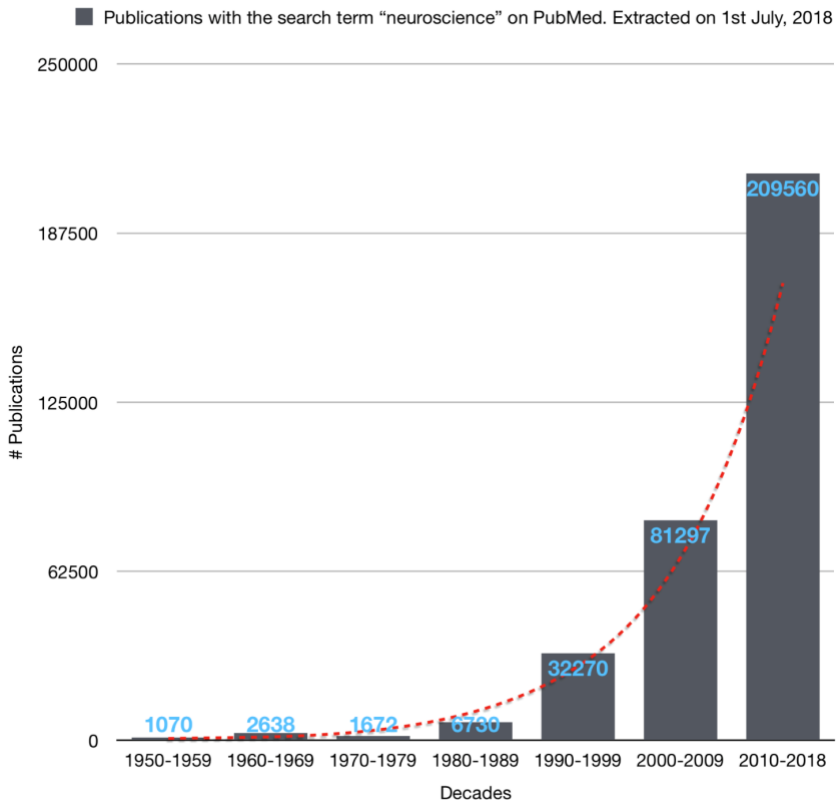


Figure 1-1 *Exponential growth in the number of scientific publications in neurosciences over the decades.*

Cajal on the other hand, refined on Golgi's staining method and proposed that neurons are discrete units of the nervous system, which terminate over a small distance and somehow communicate with dendrites of other neurons, which was termed as the neuron theory (see review: Jones, 1999). Subsequently, building on Cajal's work, physiologist Charles Sherrington first reported the presence of synapses that underlie the communication between two neurons. However, none of the

Camillo Golgi – Nobel Lecture: The Neuron Doctrine Theory and Facts: https://goo.gl/n8bf13; Santiago Ramón y Cajal – Nobel Lecture: The structure and Connexions of Neurons: https://goo.gl/2RG3PP

staining methods allowed investigations of living tissues or the entire functioning brain as a whole. This changed with Hans Berger's pioneering work in the 1920s (Berger, 1929).

In 1929, Berger demonstrated that the ongoing electrical activity in the brain could be recorded non-invasively using surface electrodes. Before this breakthrough, a majority of the investigations on the human brain relied on clinical interviews (i.e., symptomatology in the pathological conditions) or post-mortem reports. Hans Berger's work on electroencephalography for the first-time allowed clinicians to study the living human brain non-invasively. In the following decades up to the 1980s, electroencephalography (EEG) remained the gold standard method for identification of brain tumours (e.g., Walter, 1936). Subsequently, the 1970s and 1980s saw the rise of other brain imaging modalities such as magnetoencephalography (MEG; Cohen, 1968, 1972), magnetic resonance imaging (MRI; Lauterbur, 1973; Mansfield, 1977; Mansfield & Grannell, 1973), positron emission tomography (PET; Fox, Mintun, Raichle, & Herscovitch, 1984). The rise of various brain imaging methods has tightly been linked with advancements in other disciplines such as physics, mathematics, and computer science. Non-invasive measurements of brain functioning, in particular, have helped us better understand the human brain both in health and in disease. A focus of the investigations in functional neuroimaging in the last three decades has been on the development of various signal processing strategies (e.g., Ashburner & Friston, 2005; Friston et al., 1995; Smith et al., 2004) and the development of statistical frameworks for data interpretation (e.g., Friston et al., 1995; Worsley et al., 1996).

All the neuroimaging methods only offer a snapshot of brain functioning at any given time at different scales of time and space. Therefore, before any further discussion on brain dynamics, it is essential to define the scales of measurement clearly.

1.2 Scales of measurement and MEG

To produce adaptive behaviour, large ensembles of neurons in the human brain work in concert. The neuronal communication occurs within several milliseconds, but they produce behaviour that can last over seconds. We can measure this activity both directly and indirectly using various methods at various scales of time and space. **Figure 1-2** shows a plethora of methods that are available to neuroscientists. Neuroscientists typically use only one method at a time, which offers a trade-off between spatial and temporal resolutions. Therefore, the selection of a measurement technique depends on the research question at hand.

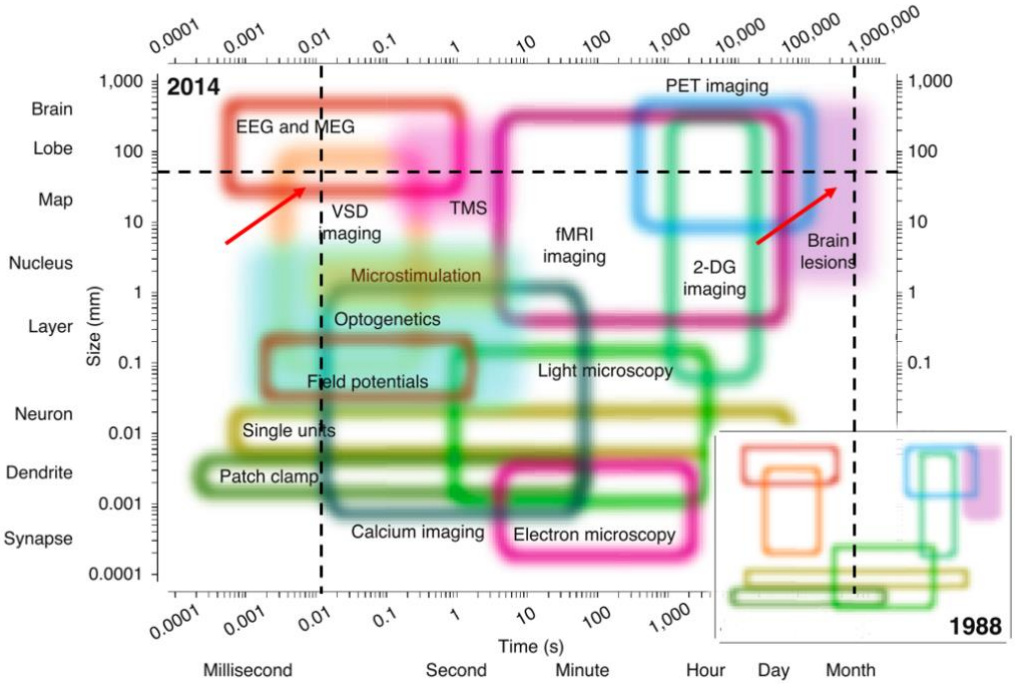


Figure 1-2 *Spatiotemporal scales of various neuroscientific methods. The X-axis shows the spatial scale and Y-axis shows the temporal scale. In this thesis, brain dynamics at two ends of the temporal spectrum were investigated using MEG. These are the two points where the horizontal dotted line intersects with the two vertical dotted lines. As an example of cortical dynamics over milliseconds, auditory evoked responses were studied. The study of cortical dynamics over years was achieved by studying group differences in MEG resting-state data. The inset shows the availability of neuroscientific methods in the year 1988. Figure adapted from Sejnowski et al. (2014).*

This thesis focuses primarily on using MEG to investigate brain dynamics occurring at the two ends of the temporal spectrum (as highlighted in **Figure 1-2**), i.e., cortical dynamics occurring over milliseconds and cortical dynamics occurring over the years (changes in ongoing activity due to training).

MEG is a non-invasive functional neuroimaging method that allows us to measure magnetic fields generated by electrical activity occurring in the brain. Although measurements performed using fMRI, provide an unmatched spatial resolution; have a temporal resolution of the order of seconds, which is very slow for studying neural dynamics. The activity measured with fMRI is an indirect measure and is a result of neurovascular coupling (Huettel, Song, & McCarthy, 2009). On the other hand, MEG provides a superior temporal resolution and comparable spatial resolution and is a direct measure of the electrical activity of the brain (Baillet, 2017; Baillet, Mosher, & Leahy, 2001). The biophysical principles of signal generation for both EEG and MEG are the same, i.e., both the techniques measure the same underlying activity. However, in comparison with EEG, MEG proves to be superior as the magnetic fields generated by the flow of electrical current in pyramidal neurons, are unperturbed by skull, meninges, and scalp. This property proves to be a unique advantage for source localisation. Due to the smearing of electrical activity by the skull, the spatial resolution achieved with EEG (even with a high-density electrode array) is of the order of few centimetres, whereas the spatial resolution of MEG is of the order of 5-10 millimetres (Hillebrand et al., 2005). By reducing the head movement in the scanner, recent studies have demonstrated that a finer spatial resolution can be achieved with MEG (e.g., Meyer et al., 2017). This is not to say that EEG does not offer us any useful information, it remains one of the most widely used methods both in research and in various medical setups.

1.3 Aims and objectives

This thesis explores cortical dynamics occurring at two ends of the temporal scale as measured non-invasively, i.e., event-related responses occurring over milliseconds,

and effects of long-term sensorimotor training on brain connectivity, in particular, effects on task-free resting-state activity.

Cortical dynamics occurring over milliseconds can be studied using many different ways. Here, the focus was on studying event-related responses; this is merely the modulation of ongoing activity elicited by an external stimulus. Auditory evoked responses were a test case. The chief reasons behind this are as follows. First, unlike fMRI, MEG acquisition is completely silent and does not interfere with auditory stimulation. Second, the temporal resolution offered by MEG is comparable with that of the auditory system. And third, although the auditory cortex is an anatomically convoluted structure, the dipoles located in the superior temporal region are tangential and as a result easily discernible by MEG. To this end, we take a classical approach of source localisation. The aim was to localise both phase-locked and non-phase-locked responses involved in the generation of auditory evoked potentials, specifically, the auditory P300 response to task-related oddball tones within a sequence of standard tones.

The human brain can undergo structural and functional changes with years of specialised training, and it has robustly been demonstrated using structural neuroimaging, resting state and task fMRI. Recently, an EEG study showed differences in resting-state connectivity in musicians and non-musicians (Klein et al., 2016). However, the study had a crucial limitation in that the data were analysed as functional networks in isolated frequency bands (i.e., theta: 6.5-8 Hz, alpha1: 8.5-10 Hz; alpha2: 10.5-12 Hz), which ignored the pan-spectral nature of M/EEG frequency bands (i.e., between band/network communication). To overcome this limitation, a novel method of network analysis (multilayer network framework) was utilised, which integrates multiple frequency bands in a unified description. The aim was to identify the differences in the multilayer network organisation of musicians and non-musicians, as a signature of sensory-motor training. Using the novel framework, it was demonstrated how resting-state network organisation differs between musicians and non-musicians.

1.4 Thesis overview

Chapter 2 of the thesis introduces MEG, including signal generation and recording hardware. MEG offers a unique balance of spatiotemporal resolution, making it an excellent tool for the non-invasive measurement of brain activity. Subsequently, **chapter 3** discusses how the MEG data can be analysed further. It reviews the theory of MEG source localisation and discusses beamforming, which has been used throughout this thesis.

In **chapter 4** we put these concepts together to investigate cortical dynamics occurring over the millisecond scale. To this end, MEG data were recorded as participants performed an auditory oddball task. The data were analysed using Linearly Constrained Minimum Variance (LCMV) beamformer, which was applied to both continuous and averaged data to study non-phase-locked and phase-locked nature of event-related responses respectively.

To measure the changes in brain activity at rest following years of musical training required the development of a novel method. **Chapter 5** introduces the basics of graph theory and in particular, the recently introduced multilayer network framework. A multilayer network treats the human brain as a "network of networks", allowing us to integrate information from different MEG frequency bands in a unified network description. The use of the multilayer network framework for between-group comparisons (such as control group vs. experimental group, a typical scenario in cognitive neuroscience) is addressed in **chapter 6**. Using empirical data, it was demonstrated that such group comparisons are biased due to differences in average connectivity. To correct for such biases, new methods are introduced and validated using simulated data.

In **chapter 7**, the new bias correction method is applied to multilayer networks to study the effects of training related plasticity using resting-state MEG recordings.

Here, musicians showed an integrated network configuration when compared with healthy controls. Furthermore, it was also demonstrated that multilayer networks provide more information than traditional single-layer approaches.

Finally, **chapter 8** provides a summary of the findings and how multilayer networks can be used further to integrate information from multiple imaging modalities to study brain networks both in health and in disease.

CHAPTER 2

2 MEG: Neurophysiological origins and instrumentation

Précis

The human brain houses over a billion neurons and a trillion synapses making it the most complex biological systems known to us. The neurons sitting inside the bony skull communicate with each other using electrical signals via synapses. It is this communication that manifests itself in observable behaviour (e.g., language, perception, speech, etc.). Therefore, to truly understand the inner workings of the human brain, it makes sense to probe the electrical communication employing non-invasive measurement techniques. Studying the magnetic fields associated with the underlying electrical fields offers certain unique advantages. Measurement of magnetic fields is achieved by a non-invasive method known as MEG. To appreciate how we can make sense of the data obtained from MEG, we first need to answer some fundamental questions – 1) What signal can we measure using MEG? 2) Where does the signal come from? And 3) How can we measure the signal? To this end, the present chapter discusses the anatomy and physiology of neurons, how large ensembles of neurons give rise to the signals measured using MEG and covers the basics of MEG hardware.

2.1 Anatomy and physiology of neurons

The human brain primarily is composed of neurons and glial cells. Neurons can be thought of as the building blocks of the human brain. The glial cells provide the necessary structural and metabolic support to the neurons. While there are several

different types of neurons, there are some common features seen across all of them, viz., a cell body (or soma), dendrites, and axons. The dendrites are the long extensions that originate from the cell body as seen in (**Figure 2-1**). The neurons of interest for MEG are the pyramidal neurons. These give rise to the signal as measured with M/EEG. The pyramidal neurons tend to have a large number of dendritic spines and a single axonal body. The pyramidal neurons, named because of the pyramid-like shape of the soma, have apical and basal dendrites.

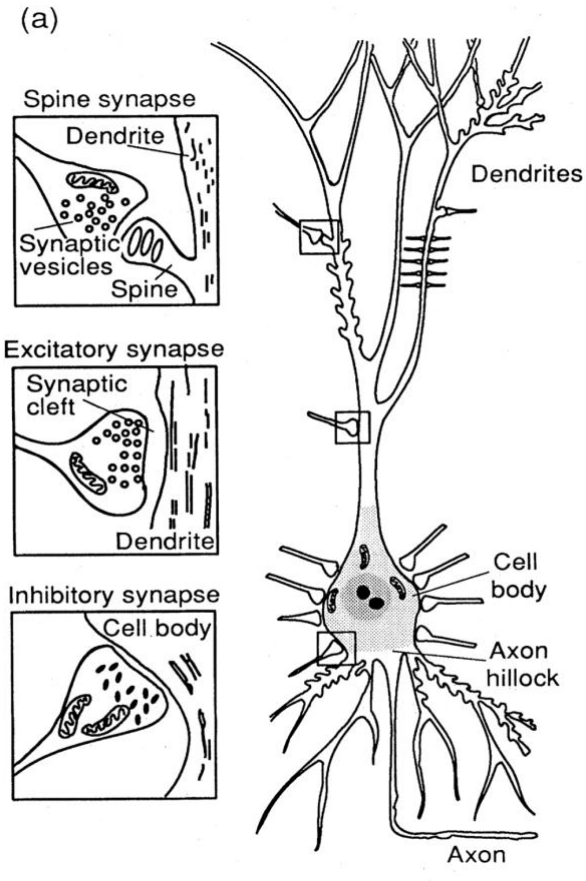


Figure 2-1 *A schematic of a pyramidal neuron. The image is taken from Hämäläinen et al. (1993).*

The cell body of a neuron receives inputs from the dendrites, making neurons the most fundamental unit of a neuronal "network". The cell body or the soma of a neuron, like the majority of the cells in the human body, contains a nucleus. The nucleus of the cell packs all the relevant genetic information. The soma also contains

the Golgi body and mitochondria; these two are involved in neurotransmission and energy production respectively.

The output of the neuron is carried via the axon. The inputs from other neurons converge at the axon hillock, which is at the base of the soma. Depending on the type of neuron, the axons can be myelinated or unmyelinated. The myelin sheath is rich in lipids and surrounds the axons, which facilitates higher transmission speeds. The gaps in myelination, as shown in (**Figure 2-2**), where the axon is exposed to extracellular space are called nodes of Ranvier. These nodes have a rich supply of ion channels, allowing them to participate in the regeneration of action potentials (AP). The axon terminates at axon terminals that form synapses (or connections) with the dendrites or soma of other neurons. It is at the synapses that information exchange takes place.

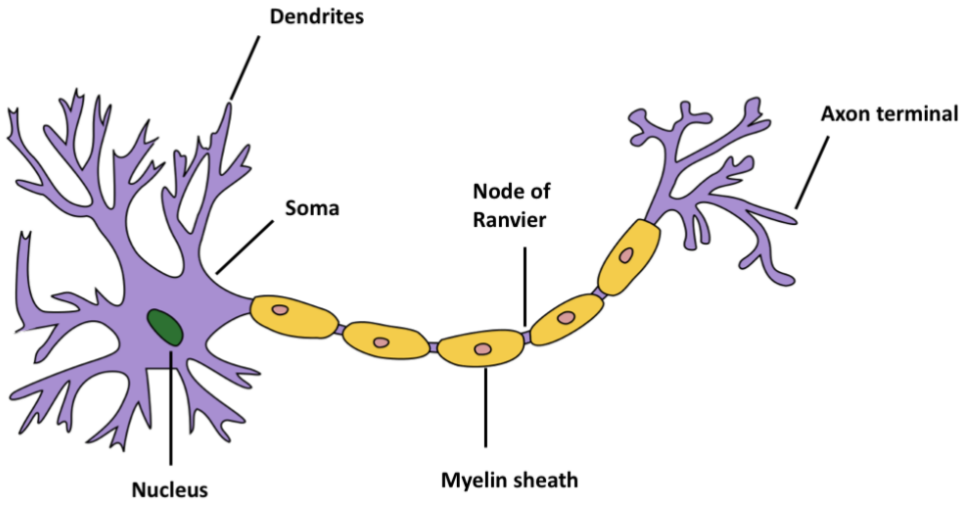


Figure 2-2 *Schematic representation of a typical neuron. Image extracted and adapted from https://en.wikipedia.org/wiki/Myelin#/media/File:Neuron_Hand-tuned.svg (creative commons).*

2.1.1 Laminar organisation: Cortical subdivisions

The cortical neurons (somata, dendrites, and axons) are typically arranged in 6 layers. The outermost is layer I, and the innermost is layer VI, which is deep-seated (**Figure 2-3**).

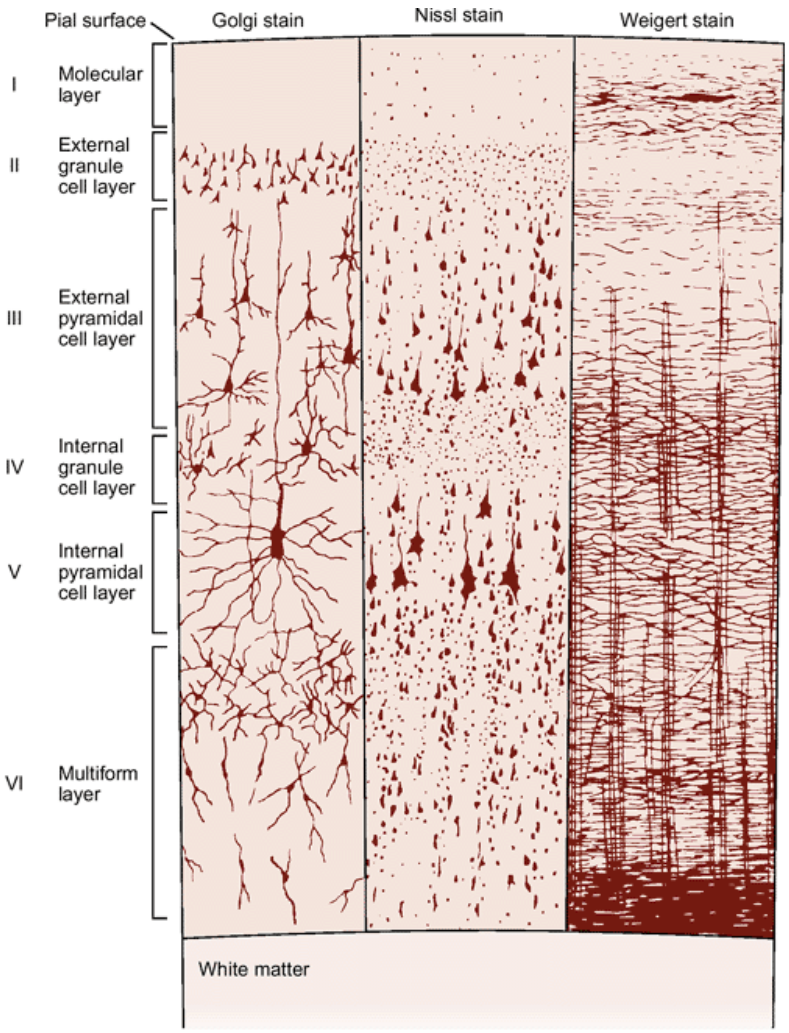


Figure 2-3 *Laminar organisation of the cortex from layer I to layer VI. Various staining methods reveal different cell types. Figure from Kandel, Schwartz, and Jessell (2000)*

Layer I: It is also known as the molecular layer. It primarily contains apical dendrites of pyramidal neurons and horizontal axons. This horizontal arrangement of dendrites allows for connections to be formed between different regions of the cortex.

Layer II: It is called the external granular layer, and it mostly contains pyramidal neurons.

Layer III: The external pyramidal layer chiefly contains small pyramidal neurons and also non-pyramidal neurons with vertical axonal projections. The layers I-III are principally involved in mediating the intracortical communication.

Layer IV: Also known as the internal granular layer contains different types of stellate and pyramidal neurons. This layer chiefly receives sensory thalamic input. As an anatomical landmark, layer IV separates supra-granular layers (I-III) from infra-granular layers (V-VI).

Layer V: Also known as the internal pyramidal layers, which contains large pyramidal neurons. The major projections from this layer make connections with other cortical and subcortical regions.

Layer VI: The polymorphic or multiform layer contains few large pyramidal neurons. The layer VI predominantly projects to the thalamus, establishing reciprocal connectivity between the thalamus and the cortex.

The laminar organisation described above contributes differently to electrophysiological recordings. Based on the invasive animal recordings, it has been suggested that the deeper layers contribute to slower oscillations (e.g., alpha waves; 8-13 Hz), whereas the more superficial layers produce faster oscillations (e.g., gamma oscillations; 30-80 Hz) (Buffalo et al., 2011; Dougherty et al., 2017).

2.2 Neuronal communication

2.2.1 Resting membrane potential

The information propagation across neurons occurs through a combination of electrical and chemical (diffusive) processes. The cell membrane contains several types of ion channels, which allow the movement of sodium (Na^+), potassium (K^+) and chlorine (Cl^-) ions in and out of the cell. These ion channels are either voltage-gated or ligand-gated. The voltage-gated ion channels open when a threshold or electrical potential is met. On the other hand, the ligand-gated ion channel serves as a binding site for neurotransmitters, and they open only when a specific neurotransmitter binds to it. For a given cell and ion, the *equilibrium potential* is the voltage across the membrane at which the electrical and chemical processes balance each other. As an exemplary, the equilibrium potential for potassium ion can be calculated using the Nernst equation:

$$E_K = \frac{RT}{zF} ln \frac{K_o}{K_i} \quad \textbf{(2.1)}$$

R = Thermodynamic gas constant

T = absolute temperature

z = valence of the ion

F = Faraday's constant

K_i = Potassium ion concentration inside the cell, K_o = Potassium ion concentration outside the cell

The resulting *equilibrium potentials* for sodium, potassium, and chlorine ions varies. However, the typical resting membrane potential depends on the type of the cell, but it is around -70mV. The resting membrane potential is calculated as a weighted

sum from the intra- and extracellular concentrations of the three contributing ions, taking into account the respective membrane permeabilities for these ions.

2.2.2 Action potential (AP)

If the potential at the axon crosses a certain threshold (around -55mV), this leads to a whole cascade of events. The first among which is the opening of voltage-gated ion channels. Following this, Na^+ ions start to flow inside the cellular space, while the K^+ ions move out to the extracellular space, which causes the sodium conductivity to change, leading to a rapid influx of Na^+ ions into the cellular space. It depolarises the membrane and raises the potential to around 40mV typically within <2ms. The sudden change in potential difference is called the AP. This cascade of events changes potentials across neighbouring membranes leading to subsequent APs which are conducted along the axon. After a sudden change in the membrane potential due to Na^+, the K^+ start to move in the intra-cellular space repolarising the membrane, which brings back the membrane to its resting state potential.

However, the magnetic fields generated by the APs are unlikely to be detected over the surface of the scalp. Firstly, the propagation of APs can be modelled as a quadrupole, i.e., two opposing dipoles separated by a small distance. The magnetic field of a quadrupole falls with a cube of distance, i.e., the magnetic fields generated by the APs are too small to be detectable over the surface of the scalp. Secondly, the APs are short-lived (<2ms), meaning they are unlikely to achieve synchrony across larger areas. Taken together, APs are unlikely to contribute to the overall MEG signal.

2.2.3 Postsynaptic potentials (PSP)

At synaptic junctions, the communication is mediated by chemical processes (i.e., neurotransmission) and not electrical processes. Once an AP arrives at the synaptic junction, it triggers the release of neurotransmitters. The neurotransmitters subsequently diffuse into a small area known as the synaptic cleft (**Figure 2-1**) to reach the postsynaptic neuron. Neurotransmitters then bind at their binding site, opening the ligand-gated channels, which leads to a flow of ions via the membrane, which causes a change in the membrane potential. However, the increase or decrease in the membrane potential depends on the type of the junction. If these ion channels allow movement of Na^+ or K^+ ions, which increases the potential, then it is called an excitatory postsynaptic potential (EPSP). On the other hand, if the channels allow movement of Cl^- ions then it decreases the potential, and so they are called inhibitory postsynaptic potentials (IPSPs). The probability that a neuron will fire an AP depends on the sum of EPSPs and IPSPs reaching a critical threshold. The postsynaptic activity creates intra-cellular currents resulting in flow across the synaptic junctions and further along the dendritic spines towards the soma. The resulting currents have dipolar magnetic patterns, which follow the *inverse square law*, i.e., the magnetic field reduces with doubling of the distance, and when compared with APs, they last over 10ms. As a result, the magnetic fields produced by the PSPs are much stronger at the surface of the scalp than those produced by APs. Plus, given that these events are longer-lived achieving synchrony across larger regions is possible, which makes them the most likely candidate source of the signals recorded by M/EEG. While in practice, MEG is said to be a direct measure of underlying electrical currents, it is an indirect measure of synaptic activity. Once the PSP starts to travel down the dendrite, the cell membrane must return to their resting membrane potential. To achieve this, ion channels pump ions out in the extracellular space. This process results in the generation of the extracellular current field called volume or impressed currents. Volume currents are typically in the opposite direction to the primary postsynaptic currents (**Figure 2-4)**.

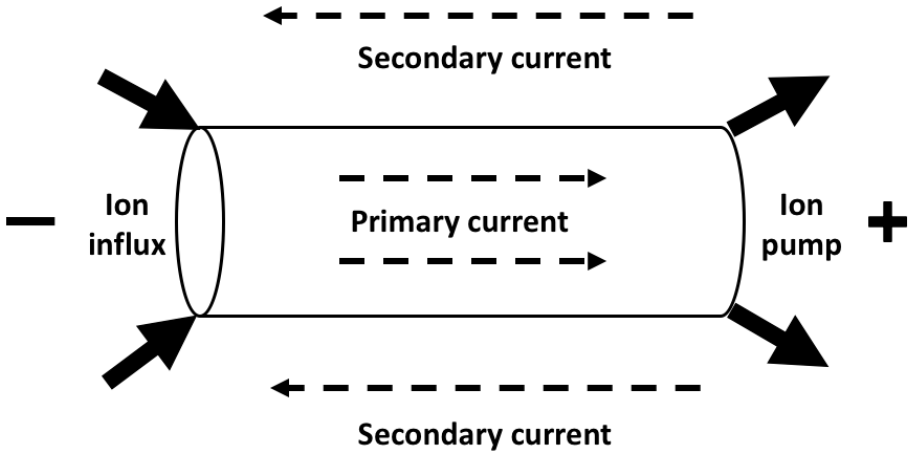


Figure 2-4 *A schematic representation of postsynaptic current flowing along a dendrite. The primary current is the direct result of an influx of ions. The secondary currents or volume currents are a result of electric fields generated as ions are released.*

2.3 MEG signals: Origins

As discussed in the previous section, the most likely generators of the MEG signal are the synchronised postsynaptic potentials (PSPs) in the dendritic spines of pyramidal neurons. A PSP generates a primary current and a volume current in the extracellular space that flows in opposite directions (**Figure 2-4**) above. Using the right-hand rule, it can be inferred that a magnetic field is orthogonal to the direction of current flow (**Figure 2-5**).

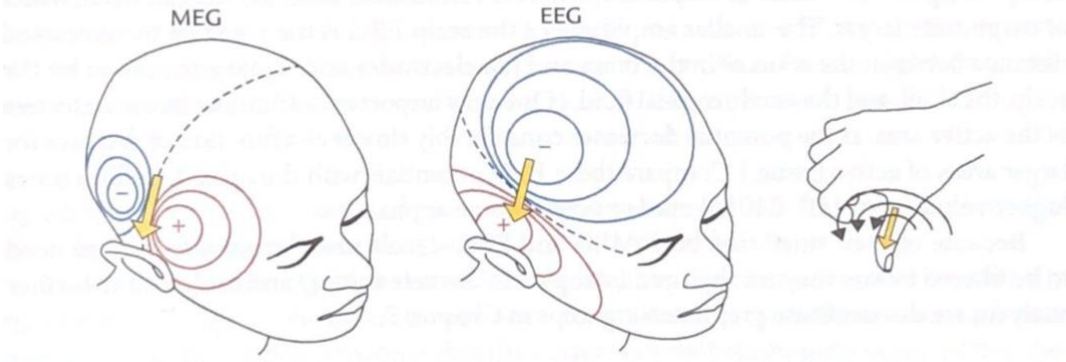


Figure 2-5 *The example shows a simple dipole in the temporal region producing magnetic fields as measured using MEG and electric fields as measured using EEG. It can be noted that the magnetic field patterns are orthogonal to the electric fields and can be explained using the right-hand rule. The image is taken from Hari and Puce (2017).*

The membrane of the dendritic spine does not constrain the volume currents generated by the PSP; as a result, they readily spread in the local extra-cellular fluid. The volume current generates changes in the electrical potential as measured by EEG over the surface of the scalp. Naturally, this electric current also has a magnetic field accompanying it, which in a spherical conductor is invisible to MEG, but the human head is not a perfect spherical conductor, and therefore some of the signal measured by MEG is made from the volume currents. However, it is thought that the dendritic PSPs of pyramidal neurons are the most significant contributor to the activity recorded by MEG. Firstly, the pyramidal neurons have a non-symmetric columnar

arrangement, where the neurons are perpendicular to the cortical surface. In other neurons, such as the stellate, the dendrites have a radially symmetric organisation, as a result, the electrical field spread occurs in the equal and opposite direction, effectively cancelling each other out. The arrangement of pyramidal neurons means that the magnetic field from multiple dendritic currents exhibits an additive property. Secondly, the rate of current flow in axons (<2ms) in much faster than it is in dendrites (~10ms). Making synchronisation of large numbers of axonal APs an unlikely event. Thirdly, the field from axonal currents modelled as a quadrupole follows a $1/r^3$ relationship. As against, the field from dendritic PSP modelled as a dipole follows a $1/r^2$ relationship (r = distance). Therefore, the magnetic field produced by PSPs over the surface of the scalp is much higher than the one produced by axonal APs.

2.3.1 What can we measure using MEG?

The data recorded using MEG has a high temporal (and spectral) resolution, and it can be analysed using many different ways. Here, two broad analysis types are discussed.

2.3.1.1 Spontaneous activity

The easiest measurement that can be performed using M/EEG is the measurement of spontaneous/ongoing activity. Berger (1929), performed the first measurements of spontaneous electrical activity using EEG and observed that oscillations occurred at a characteristic frequency (8-13 Hz) over the occipital lobe. An interesting observation from this study was that the spontaneous activity could be modulated by just closing and the opening of the eyes. These results were replicated by Cohen (1972) using a superconducting magnetometer.

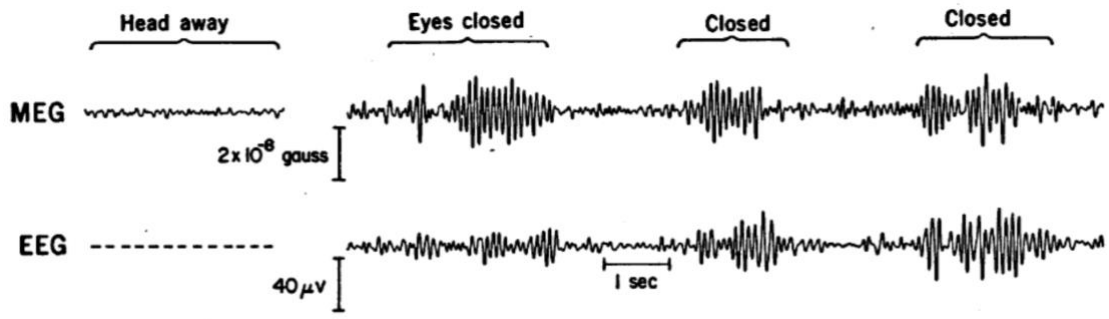


Figure 2-6 *The very first traces of alpha rhythm recorded using a superconducting magnetometer from the occiput of a healthy subject. The modulation of alpha activity on the opening and closing of the eyes can be seen in both electrical and magnetic traces. Image from Cohen (1972).*

This pioneering finding has been the basis of much of the human electrophysiological research (see **Table 2-1**, M/EEG frequency bands). Since then, significant progress has been made in characterising various oscillatory phenomena and their physiological role. The oscillatory components typically range from low frequencies (Delta, 1-4 Hz; Theta, 4-8 Hz), to high (Alpha, 8-13 Hz; Beta, 13-30 Hz; Gamma > 30 Hz). There have been some attempts at detecting even higher frequencies (>80 Hz, e.g., Buzsáki et al., 1992). However, delta to gamma is the most commonly used frequency range in most electrophysiological studies. In terms of their physiological roles, each frequency band has been shown to be involved in distinctly different physiological functions. For instance, the delta band has been shown to be involved in sleep (Hobson & Pace-Schott, 2002), the theta band in episodic memory (Lega, Jacobs, & Kahana, 2012), the alpha band in attention modulation and visual tasks (Jensen & Mazaheri, 2010; Palva & Palva, 2007; van Diepen et al., 2016), the beta band in motor function (Baker, 2007), and gamma-band in visual perception and integration (Singer & Gray, 1995). It has also been shown that the ongoing activity can be modulated in the presence of a task, for example, post-movement beta rebound (Jurkiewicz et al., 2006; Pfurtscheller et al., 2005).

Beyond some of the physiological roles described above, it has also been postulated that neuronal oscillations sub-serve communication between brain regions via coherence (see review: Fries, 2005). It has been argued that for there to be efficient communication between brain regions they have to oscillate in synchrony.

Table 2-1 *Summary of human electrophysiological frequency bands*

Frequency band	First detection
Delta (1-4 Hz)	Grey Walter, 1936
Theta (4-8 Hz)	Grey Walter, 1936
Alpha (8-13 Hz)	Hans Berger, 1929
Beta (13-30 Hz)	Hans Berger, 1929
Gamma (>30 Hz)	Herbert Jasper & Howard Andrews, 1938

The table is taken from Hari and Puce (2017)

2.3.1.2 Evoked and induced responses

Going beyond the spontaneous activity described above, M/EEG studies also commonly utilise external stimuli and observe changes in the ongoing activity that are time and phase-locked to the stimulus onset or offset. The presence of external stimuli results in a characteristic change in the electrical (as measured by EEG) and magnetic (as measured by MEG) field. A typical study using evoked responses involves the repeated presentation of a stimulus over multiple trials. These trials are subsequently averaged in time, which cancels out any random, non-phase-locked activity, leaving a large evoked signal, which has peaks and troughs, indicating changes in the underlying field strength over time (**Figure 2-7**). Evoked responses can be elicited using an external stimulus in auditory, visual, somatosensory, and olfactory modalities (Luck, 2005).

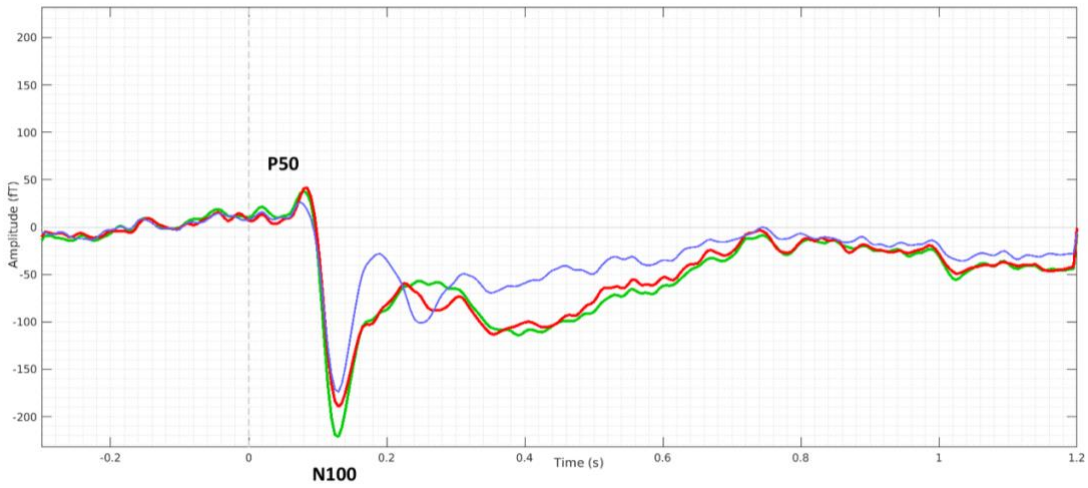


Figure 2-7 *An example of event-related responses to auditory stimulation recorded using MEG, showing positive (P50) and negative peaks (N100). Auditory stimuli were pure tones (frequency: 1000 Hz, duration: 100ms), which were presented at a regular interval of 1.5sec. For the purpose of illustration, the traces were averaged in MEG sensor space across 10 subjects. The three traces represent different sensors. X-axis: Time in seconds, Y-axis: Amplitude in fT.*

On the other hand, a stimulus-related change in the ongoing oscillatory brain activity that is time-locked but not phase-locked is referred to as an induced response (Pfurtscheller & Lopes da Silva, 1999). Up until recently, induced responses have often been considered noise, however, many studies have shown a functional role of induced oscillations. For example, event-related desynchronization is seen in beta band (over sensorimotor cortex) following a movement (abduction of index finger) (Jurkiewicz et al., 2006) or the gamma-band power changes following the presentation of high contrast and luminance visual gratings (Adjamian, Hadjipapas, Barnes, Hillebrand, & Holliday, 2008; Adjamian et al., 2004). These results provide evidence that induced oscillatory activity is important for both perception and action. As the induced responses are not phase-locked, they are not detectable in averaged responses. Typically, an induced response can be obtained by band-pass filtering and squaring the signal of interest, retaining oscillatory power changes. While this method was popular in the past, in recent times, the Hilbert transform is commonly

used. Hilbert transform extracts the oscillatory envelope of the signal. In both these processing strategies, power envelope is typically averaged across a number of trials, which minimises the noise even further and allows appropriate extraction of induced responses. To further increase the signal to noise ratio, both in evoked and induced responses the signal of interest is baseline corrected by subtracting activity from a period of no interest (e.g., pre-stimulus baseline).

2.4 Instrumentation: MEG

MEG is a non-invasive brain imaging technique that allows the measurement of the magnetic fields generated by the brain over the surface of the scalp (for schematic see **Figure 2-8A)**. The first recordings of the magnetic fields of the brain using a superconductor were performed in the '70s (Cohen, 1972); however, the advancements in MEG have been relatively recent, and these have been tightly linked with advancements in the other disciplines, such as superconductivity (Zimmerman, Thiene, & Harding, 1970) and computing. The invention of Superconducting QUantum Interference Devices (SQUIDs), allowed Cohen (1972) to measure the magnetic fields without the use of copper coils. Since then, the instrumentation has become a lot more sophisticated and has allowed scientists to record activity over the entire surface of the brain with hundreds of sensors (Hari & Salmelin, 2012). These sensors are typically placed in a helmet-shaped vessel where the subject can place their head for measurements (Hämäläinen et al., 1993; Hari & Puce, 2017; Hari & Salmelin, 2012). The underlying mechanism or the biophysics, which generates magnetic fields as recorded by MEG or electrical fields as recorded by EEG, is the same. During both the measurements, we measure postsynaptic activity in the pyramidal neurons (Baillet, 2017; Baillet et al., 2001). The magnetic fields of the brain are in the femtotesla (10^{-15} Tesla) region, which is about a billion times smaller than the Earth's magnetic field.

Figure 2-8B shows the sources of various magnetic fields and their strength. Apart from the environmental sources of interference, the participant's biological

processes can contaminate our signal of interest. During MEG data acquisition, the magnetic fields generated by the participant's heartbeat and eye blinks are the most significant sources of interference. As a result, we need very sensitive equipment (SQUIDs) and strategies for interference rejection (i.e., magnetically shielded rooms or MSR). Here, a clear distinction must be made between sources of interference and noise. Magnetic interference is caused by magnetic fields of no interest (e.g., eye blinks, heartbeat) or by a piece of lab equipment that is inside the MSR and it tends to affect all the sensors. On the other hand, the source of noise could be internal (e.g., internal SQUID noise) and will likely affect some sensors more than the others.

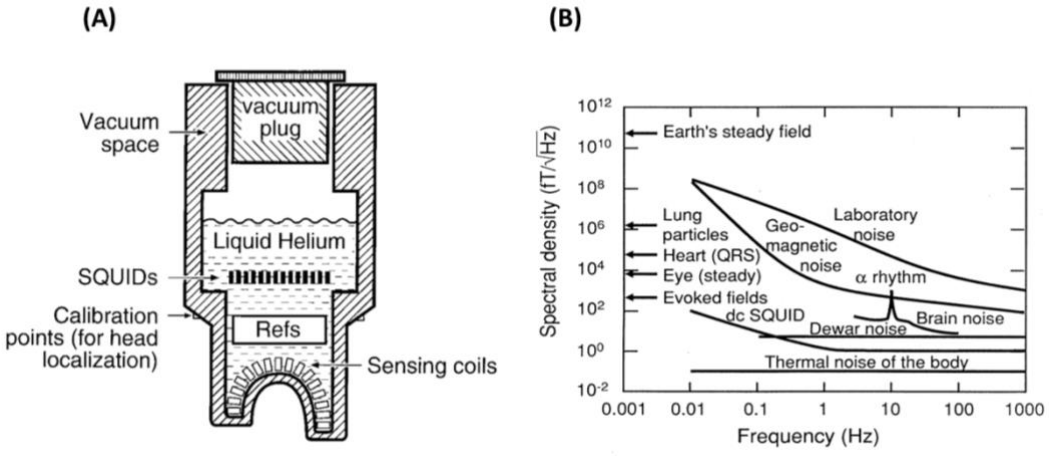


Figure 2-8 (A) *Schematic of a typical MEG scanner (Figure from Vrba & Robinson, 2001)* ***(B)*** *Various sources of magnetic interference and their corresponding field strengths. It is worth noting that both biological and environmental sources of interference are several magnitudes higher than the activity of the brain (the alpha rhythm for reference). This figure demonstrates the need for effective shielding strategies. The figure is taken from Hämäläinen et al. (1993).*

All materials show some intrinsic resistance to the flow of electric current, however, when some materials are cooled below a "critical temperature", they lose their electrical resistance and become superconductors. This means that a current flowing in a superconductor will flow for an infinite amount of time as long as the temperature stays constant. Beyond the temperature, a superconductor has two critical conditions, viz., critical applied magnetic field and current. Exceeding these

limits results in the material returning to its non-superconducting state. The commonly used material to construct SQUIDs is niobium, which is immersed in liquid helium to achieve its superconducting state. The superconducting state is produced by pairing of electrons, which forms Cooper pairs. Josephson (1962) was the first to predict tunnelling of superconducting Cooper pairs through a thin electrical insulating barrier. These Josephson Junctions (JJ) or *weak links*, allow for the measurement of flux dependent current across the SQUID. The SQUID assemblies are typically very small and therefore are connected to flux transformers which offer larger surface areas. The increased surface area offers an increase in sensitivity. However, this reduces the spatial selectivity of the measurements as the brain signals are picked from a large area at the same time.

The flux transformers have pick up coils that are close to the surface of the head. The magnetic fields produced by the brain induce currents in the pickup coil coupled to a SQUID. By feeding a constant bias current through the SQUID, time-varying changes in the magnetic field may be detected as modulations in the measured voltage across the SQUIDs (**see Figure 2-9**). The use of a constant bias current achieves the following – 1) It prevents the SQUID sensor from reverting to a resistive state and 2) SQUID measures a time-varying fluctuation in the feedback current instead of measuring the absolute field (Hämäläinen et al., 1993; Hari & Puce, 2017).

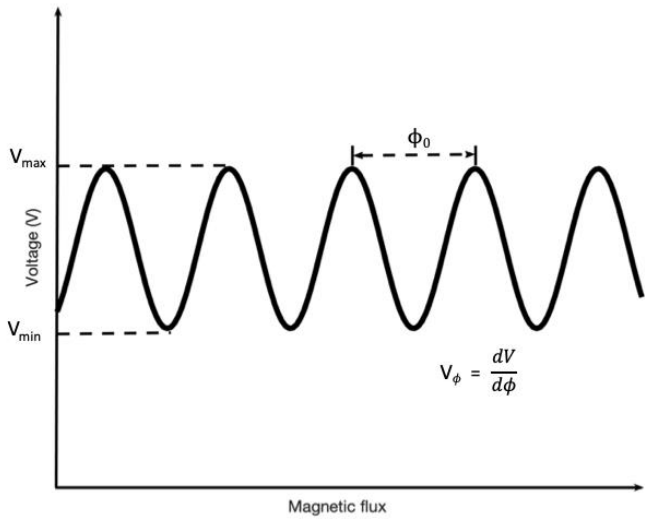


Figure 2-9 *The voltage (V), in the SQUID sensor is a sinusoidal function of magnetic flux (ϕ). The sensor is kept in its optimum working area by a feedback loop. Figure adapted from Hari and Puce (2017).*

While the MSR attenuates a majority of the environmental noise, the biological noise (e.g., eye blinks, heartbeats) can be attenuated further by making some changes in the design of the pick-up coils.

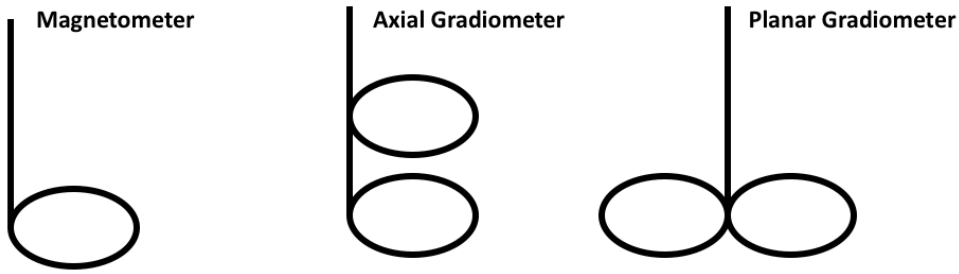


Figure 2-10 *Three commonly used configurations of MEG pick up coils. CTF-MEG system used in this thesis uses the axial gradiometer configuration.*

Magnetometers

Magnetometers (**Figure 2-10**) are the most basic form of pick up coils used in MEG systems. They utilise a single loop, which measures changes in magnetic flux that are

perpendicular to its plane, which makes the assembly highly susceptible to extraneous noises. As a result, it relies extensively on the MSR for interference rejection.

Gradiometers

Gradiometers (**Figure 2-11**) rely on the principle that magnetic fields reduce with the square of the distance. This principle also applies to extraneous noise sources, i.e., magnetic field gradients are largest for sources that closest to the sensors than sources that are farthest from the sensors. Therefore, by measuring the magnetic field gradient rather than the absolute magnetic field results in an improved SNR. While this approach successfully reduces interference from sources farther from the sensors, they can also be less sensitive to deeper neuronal sources.

The CTF MEG system used in this thesis uses a first-order axial gradiometer assembly (**Figure 2-10**). In this hardware setup, a compensation coil (wired loop) is connected to the pick-up coil. The compensation coil produces a flux that is opposite to that of the pick-up coil. As the pick-up coils are closer to the surface of the head (i.e., closer to the sources), the magnetic field reduces with the square of the distance between the coils thereby generating a current only at the pick-up coils. The distance between the coils is referred to as the baseline distance (**Figure 2-11**). The CTF system typically uses a baseline distance of approximately 5cm, which provides the golden mean between sensitivity to sources and the interference rejection properties.

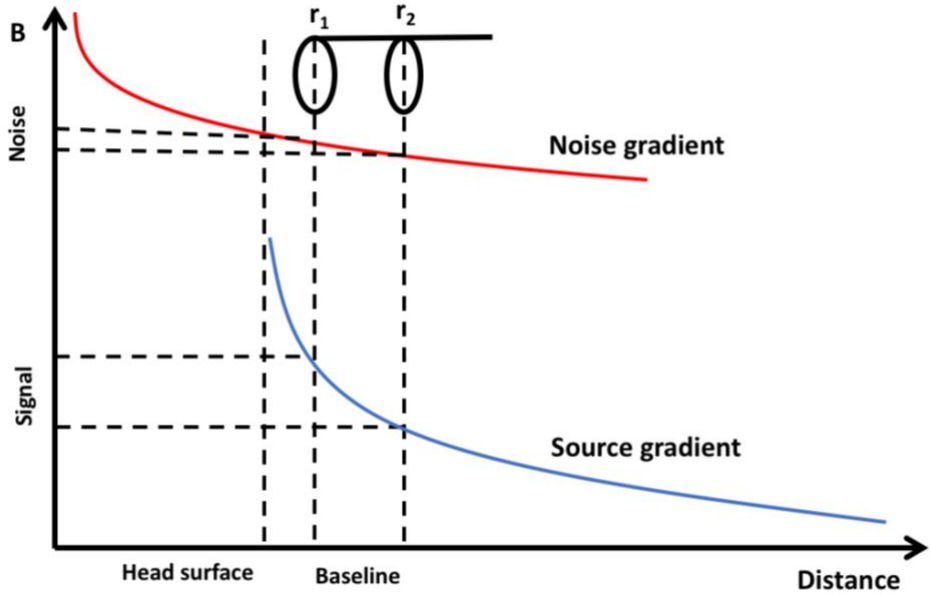


Figure 2-11 *An illustration showing the effect of first-order gradiometers. Due to the baseline distance, the interfering noise is attenuated. Baseline distance = r_2-r_1, X-axis: Distance, Y-axis: Magnetic field (B)*

For typical sources of magnetic interference that are away from the subject's head, the magnetic field decay is small across both the coils. The extraneous noise sources produce current levels that are equal and opposite across both the coils cancelling each other out, which significantly minimises the interference.

In addition to axial gradiometers, some MEG systems use planar gradiometers (**Figure 2-10**). This arrangement uses two coils that are organised tangentially; this means that the planar gradiometers occupy more space in the sensor array than axial gradiometers. Therefore, to accommodate more sensors the baseline distance is very small, which offers a lower sensitivity to deeper sources.

The CTF MEG system houses 29 reference sensors that are placed inside the dewar above the helmet (**Figure 2-8A**). The reference sensors only monitor external magnetic interference and not neuromagnetic signals (Vrba & Robinson, 2001). The output produced by the reference array is combined and subtracted from the output as measured by the sensor array. This has been shown to be useful in reducing low-frequency artefacts (Vrba & Robinson, 2001).

In summary, this chapter offers a comprehensive overview of the neuromagnetic phenomena, from origins to its measurements. Given the timescale of APs and PSPs, the signals measured by MEG are likely produced because of the synchronisation of PSPs. Further, its measurement is made possible by the use of SQUIDs. However, the measurement is extremely sensitive to both environmental and subject-specific (biological) sources of noise. The first level of interference rejection is achieved by housing the MEG inside an MSR. Moving from magnetometers to first-order axial gradiometers offers further interference rejection. Furthermore, using the synthetic gradiometers approach reduces the low-frequency interference.

CHAPTER 3

3 Source analysis of MEG data

Précis

Once the brain activity is measured using MEG, the next step is to accurately estimate the spatiotemporal dynamics of the underlying currents that generate the magnetic fields. Unlike the BOLD responses measured by fMRI, which provide an indirect index for the underlying neuronal activity via neurovascular coupling, the source images produced using M/EEG are a direct measurement of the underlying electrical activity generated by populations of neurons. To estimate this activity in source space, we first need to address two problems – 1) Forward problem, and 2) Inverse problem. The present chapter provides an overview of these problems and their solutions. Here, we mainly focus on beamforming.

3.1 Introduction

Once the MEG data has been recorded, the next obvious step is to identify the underlying neuronal substrates that gave rise to the activity, which is achieved by source analysis. Furthermore, to identify functional connectivity, it is recommended that we use source localised MEG data, as it aids the accurate interpretation of the results. This is not to say that connectivity analysis cannot be performed in sensor space. However, the former overcomes some of the limitations posed by the latter. The limitations of the sensor space analysis can be found in Schoffelen and Gross (2009), these include field spread, superposition of waves and external interference. Before the development of advanced source analysis methods, sensor space analysis was the norm; nowadays it is rather an exception. To move into the source space, two problems must be addressed (**Figure 3-1**). First, the forward problem, which is,

'given a known current distribution in the head, can we estimate the magnetic field outside of the brain?' Second, the inverse problem, which is, *'given a known magnetic field distribution outside of the head, can we estimate the current distribution inside the brain?'* The forward problem is a well-posed problem, i.e., there exists a unique solution. On the other hand, the inverse problem is ill-posed, which means that there is no unique solution to it, as infinite configurations of the underlying sources may give rise to the same measured magnetic field pattern (*sensors << sources*). However, by making some assumptions about how the data are generated, we can arrive at a solution which provides a reasonable approximation of the underlying currents.

3.2 Forward problem

The forward problem is well-posed, i.e., a single unique solution exists. As the magnetic permeability of the head is the same as that of free space, the forward problem can be simplified further by treating the entire cranium as a homogeneous medium. Consequently, the solution of the forward problem for MEG is considerably simpler than for EEG where the scalp, skull, and meninges have different conductive properties resulting in a distortion of scalp-surface detected electrical potentials. Computationally intensive methods such as the boundary element method are necessary to create an accurate model for each of the surfaces separately for EEG based source localisation.

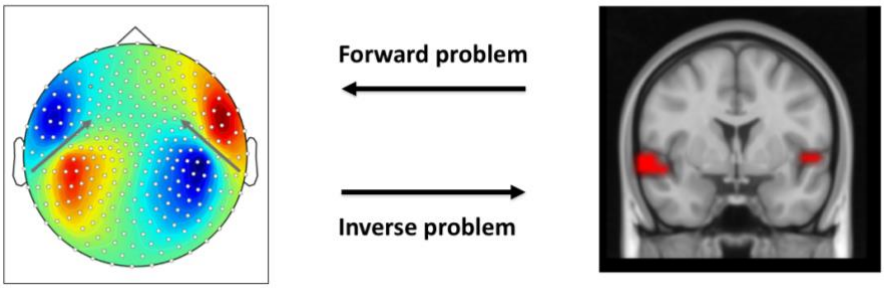


Figure 3-1 *Relationship between the forward and the inverse problem. The* ***left panel*** *shows orientation and the field patterns of the dipoles (i.e., recorded data) and the* ***right panel*** *shows the location of the two dipoles in source space (i.e., estimated current distribution).*

The magnetic field produced as a result of the synchronous firing of populations of neurons, flowing through the dendrites of pyramidal neurons (see **section 2.3**) can be modelled after a simple current dipole (separation of positive and negative charges). As the magnetic permeability of the cranium is uniform, it can be modelled as a single sphere. It was demonstrated that this is a reasonable assumption to make as the secondary volume currents (see **section 2.2.3**) do not contribute to the magnetic fields detected on the surface of the scalp (Sarvas, 1987).

However, the head is hardly a perfect sphere, and due to the advances in computing, it is now more common to use realistic head models. The experimental choice about the forward model is very critical as the calculation of lead fields (explained in **section 3.3**) depend on this. Throughout this thesis, a multiple spheres head model was used (Huang, Mosher, & Leahy, 1999), which is anatomically more accurate than the single sphere model. Multiple spheres model works by fitting overlapping spheres for every MEG sensor.

3.3 Inverse problem

The inverse problem is ill-posed, i.e., an infinite number of dipole configurations may give rise to the observed magnetic field patterns. Several approaches now exist that can identify inverse solutions that are more likely than the others. For example, beamforming (Barnes et al., 2006; Brookes et al., 2008; Hillebrand & Barnes, 2005; Hillebrand et al., 2005), minimum norm estimates (Dale et al., 2000; Hauk, 2004; Hauk, Wakeman, & Henson, 2011; Hincapié et al., 2017), and Bayesian approaches (Friston et al., 2008; Lopez et al., 2012; Wipf & Nagarajan, 2009; Woolrich et al., 2011). Here, the emphasis will be on beamforming, as this method has been used throughout the thesis.

3.3.1 Beamforming

Beamforming methods were primarily used in radar technology, to selectively enhance signals coming from target locations while attenuating the signals coming from the other locations. This technology has seen applications in consumer electronics, for example, WiFi routers and microphones. Beamforming works by weighting the contribution of every sensor in the overall output. M/EEG researchers have capitalised on the ability to selectively weight sensors to enhance activity coming from some regions. However, to successfully retrieve any activity using beamformers they assume that no two sources are correlated. In the presence of perfectly correlated sources, beamformers retrieve no power. Correlated sources are common in auditory tasks, in such scenarios, researchers prefer using other source localisation methods that do not make the same assumptions (Brookes et al., 2007; Diwakar et al., 2011; Gascoyne et al., 2016; Moiseev & Herdman, 2013).

As mentioned in section 3.3, several approaches have now been developed to solve the inverse problem. However, calculating the lead fields is a necessary step in most approaches. In essence, a lead field vector $(\boldsymbol{l}_\theta)$ is a column vector that contains the measurements of each MEG sensors for a single dipole. As CTF data are used in this thesis, a lead field for a single dipole would correspond to a 275-element column vector. Typically, a whole-head MEG system has nearly 300 sensors and based on the voxel size decided for the analysis it is possible to have more than 15,000 locations for dipoles with orientations along the 3 axes. This can be written mathematically as follows:

$$\boldsymbol{m}(t) = \boldsymbol{L}\boldsymbol{q}(t) + \varepsilon \qquad \textbf{(3.1)}$$

Here, ***m*** corresponds to the measured magnetic field at time *t* from all the sources across the entire brain volume, ***L*** is the lead field, ***q*** represents the magnitude of the dipoles, and ε represents the error term.

This means that the inverse problem is estimating ***q*** based on measured magnetic fields and lead fields.

Beamforming, a spatial filtering approach, uses a weighted sum of the signals at all the MEG sensors to calculate changes in the underlying dipole strength at any one location/orientation in the brain. The spatial filter estimates neural activity at the given location (e.g., a voxel in brain space) while attenuating signals from other locations. Activity at other location often includes biological artefacts (e.g., subject's heartbeat, eye blink, muscle artefact etc) and activity from other brain regions. This strong artefact rejection property of beamformers is quite useful in accurately capturing underlying neural dynamics.

Mathematically, the weighted sum to estimate dipole strength at given location θ, $\hat{\boldsymbol{q}}_\theta(t)$ at time t can be written as

$$\hat{\boldsymbol{q}}_\theta(t) = \boldsymbol{w}_\theta^T \boldsymbol{m}(t) \qquad \textbf{(3.2)}$$

Here, $\boldsymbol{w}_\theta$ represents the sensor weights at the source location θ and ***m(t)*** is the column vector of measured magnetic fields. For accurate source reconstruction, estimating the sensor weights is the most crucial step. Incorrect sensor weighting will lead to mislocalisation of sources.

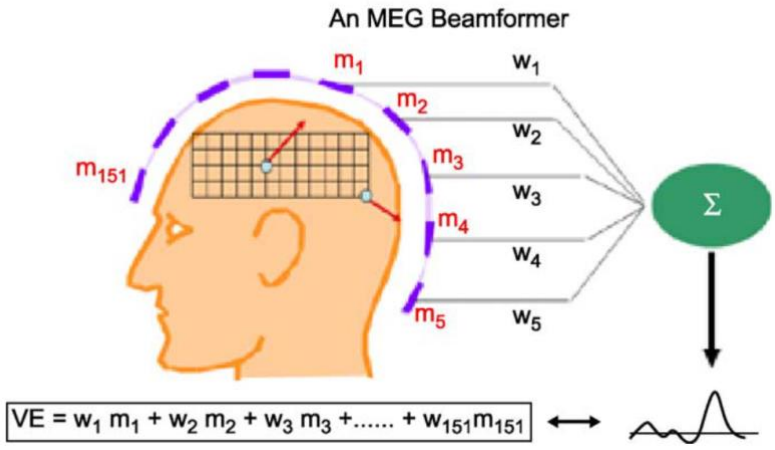


Figure 3-2 *Illustration of beamforming. To estimate the virtual electrode (VE) output, the signal at a region of interest is reconstructed as a weighted sum of the MEG sensors (shown for a 151-channel system; the CTF system used in the thesis has 275*

channels). The weights are assigned such that signal from the region of interest is maximised, while attenuating sources of noise from other regions. This step is sequentially run for every region in the brain (resulting in a VE output for each of the pre-defined grid points. VE is the same as $\hat{\boldsymbol{q}}_\theta(t)$ in equation 3.2). Figure from Hillebrand and Barnes, (2005).

For illustration purposes, we will assume the head as a single sphere volume conductor (Sarvas, 1987) and a single equivalent current dipole, with known orientation as our source of interest. As can be seen in (**Figure 3-2**), the measured neural signal (or virtual electrode output) originating from our region of interest can be reconstructed as a weighted sum of the MEG sensor measurements. The weights are chosen such that signal originating from our region of interest contributes the most to the overall output, while signals from all the other locations are suppressed (expressed as the minimisation problem). Mathematically it is as follows:

$$min_{W_\theta}|\langle\hat{\boldsymbol{q}}_\theta^2\rangle|; \text{ subject to } \boldsymbol{w}_\theta^T\boldsymbol{l}_\theta = 1 \qquad \textbf{(3.3)}$$

As the CTF MEG system has 275 sensors, $\boldsymbol{w}_\theta$ is the [275 x 1] sensor weighting matrix, $\boldsymbol{l}_\theta$ is the lead field vector, $\hat{\boldsymbol{q}}_\theta^2$ is the dipole variance. The linear constraint $\boldsymbol{w}_\theta^T\boldsymbol{l}_\theta = 1$ is applied from the definition of lead fields, i.e., the retrieved power for a given location remains at unity.

The sensor weights $\boldsymbol{w}_\theta$ can be estimated as follows:

$$\boldsymbol{w}_\theta = \frac{\boldsymbol{C}^{-1}\boldsymbol{l}_\theta}{\boldsymbol{l}_\theta^T\boldsymbol{C}^{-1}\boldsymbol{l}_\theta} \qquad \textbf{(3.4)}$$

$\boldsymbol{C}^{-1}$ is the inverse of the data covariance matrix, l_θ is the lead field for the current dipole at location θ. Covariance matrix $\boldsymbol{C}$ is computed as

$$\boldsymbol{C} = \langle\boldsymbol{m}(t)\boldsymbol{m}(t)^{\boldsymbol{T}}\rangle \qquad \textbf{(3.5)}$$

$\boldsymbol{C}$ is a diagonal matrix with each element in the matrix corresponding to a location θ, $\langle x \rangle$ refers to average over time.

The typical differences seen in various source localisation algorithms depend on the assumptions about source covariance (Hillebrand & Barnes, 2005; Mosher, Baillet, & Leahy, 2003). Furthermore, the Linearly Constrained Minimum Variance (LCMV) (van Veen et al., 1997) beamformer coupled with a method that optimises source orientation is called the Synthetic Aperture Magnetometry (SAM, Singh, Barnes, & Hillebrand, 2003; Vrba & Robinson, 2001). The source optimisation is performed by selecting an orientation where the retrieved power is maximum.

As the brain activity is continuously changing over time, the aim of beamforming (or any source localisation method) is to generate images of the brain that reflect changes in the activity. To derive images of changing signal strength (*Z*) across the entire brain space for any given location θ, *Z* can be computed as

$$Z_\theta = \frac{(\boldsymbol{w}_\theta^T \boldsymbol{C} \boldsymbol{w}_\theta)}{(\boldsymbol{w}_\theta^T \boldsymbol{w}_\theta)} \quad \textbf{(3.6)}$$

Beamforming can be used to estimate brain activity during an active time window, by contrasting it with a period of rest (control window). Typically, MEG data are first filtered in the frequency band of interest. In the second step, beamforming is used to contrast the activity between an active and a control window. The data covariance is estimated separately for the two windows and beamformer weights are estimated. A pseudo-*t*-statistic image is estimated as –

$$T = \frac{P_{active} - P_{control}}{N_{active} + N_{control}} \quad \textbf{(3.7)}$$

P_{active} = Power in active window, $P_{control}$ = Power in control window

N_{active} = Noise in active window, $N_{control}$ = Noise in control window

The beamformer output (**equation 3.7**) is generated for each of these windows (i.e., a difference of source power in the given time windows), to generate a pseudo-*t*-statistic image.

In **chapter 4**, to study oscillatory power changes and phase-locked activity as participants performed the auditory oddball task, we utilised LCMV beamformer for both continuous and averaged data. In **chapters 6** and **7**, continuous resting-state data are studied using LCMV beamformer.

It is worth mentioning that MEG only measures brain function and therefore, prior to performing any source analysis, the MEG data has to be co-registered to an anatomical MRI of the participant. In this thesis, the following steps were used.

First, the positions of the fiducial markers (nasion, left preauricular and right-preauricular) were used to obtain information about the position of the participant's head relative to the MEG scanner.

Second, a 3D surface was extracted using edge detection from the anatomical scans.

Third, the digitised head shapes obtained using the Polhemus 3D digitiser system (https://polhemus.com), were aligned with the sensor positions using an iterative closest point algorithm. All the anatomical images used in this thesis were acquired at 3T 1mm^3 isotropic resolution.

CHAPTER 4

4 Prefrontal theta and alpha power increases to attended auditory oddballs

Précis

In this chapter, cortical dynamics occurring over the millisecond temporal scale were investigated. To this end, this study investigated the neural sources of auditory oddball responses at ~300ms (P300) latency, using the high spatiotemporal precision of MEG. Event-related responses are modulations of ongoing brain activity elicited by an external stimulus, which can be either phase-locked and non-phase-locked. Oscillatory band power changes and averaged phase-locked activity were studied in MEG data recorded from 10 participants as they performed an auditory oddball task. The data were analysed using SAM to localise oscillatory band power changes (as event-related synchronisation or ERS). Group analysis of SAM images was performed using statistical non-parametric mapping (SnPM). Furthermore, linearly constrained minimum variance (LCMV) beamformer analysis was also applied to averaged data, to localise neural sources of averaged phase-locked activity. SAM-SnPM and LCMV analysis of averaged data localised neural sources of ~100ms (N100) in bilateral auditory belt area, demonstrating a convergence between both phase-locked and non-phase-locked sources of N100.

At P300 latency, neural sources of ERS in P300 window were found over frontal and frontocentral regions. Neural sources of phase-locked averaged activity in the same window were found in the frontal and middle prefrontal cortex. The ERS activity was widespread, whereas, the phase-locked activity was focal. Auditory oddball responses at P300 latency arise from multiple regions in the brain. Studying both the phase-locked and non-phase-locked responses, has allowed us to obtain a comprehensive source representation of the elusive auditory P300.

4.1 Introduction

P300 (P3), an event-related potential (ERP), is elicited by using an oddball paradigm, in which two different stimuli (in auditory domain either different in frequency or intensity) are presented in a randomised sequence, with one occurring frequently (standard) and the other less frequently (deviant). The listener is asked to respond only to the deviant stimulus either by keeping a mental count or by pressing a button. When the brain activation is measured using electro- or magnetoencephalography (EEG, MEG), responses to deviant tones – recorded as averaged event-related responses – depending on the instructions given to the participant. Unattended deviant tones elicit mismatch negativity (MMN, see review: Näätänen et al., 2007), reflecting sensory trace and involuntary attentional switch. Whereas, attended deviant tones elicit a P300 wave (in this case, P3b), a deflection (positive-going in EEG) reaching a peak between 250 and 500ms after stimulus onset (see reviews: Kok, 2001; Polich, 2007; Verleger, 1988).

Although P300 waves were first reported more than 50 years ago (Sutton et al., 1965) and have been widely studied since then, their neural sources remain elusive. Of particular interest are the contributions of auditory cortex (in the superior temporal lobe) vs. extra auditory, modality-independent brain areas. For example, an EEG study by Winterer et al. (2001) found neural generators of P300 (240-420ms post-stimulus) in temporo-parietal lobes, anterior and posterior cingulate cortex and the prefrontal cortex. There are also equivocal reports indicating the involvement of the hippocampus (O'Donnell et al., 1993; Polich & Squire, 1993). The interpretation of these results is hampered by the problem of volume conduction, resulting in distortion of the electrical current distribution over the surface of the scalp as measured by EEG. On the other hand, the magnetic fields as measured by MEG are not affected by the problem of volume conduction (Hämäläinen et al., 1993). Therefore, for non-invasive source localisation (in particular for cortical sources),

MEG proves to be an optimal method, which offers a unique balance of spatio-temporal resolution.

In M/EEG data, event-related responses can be analysed in the following ways –

1) Through analysis of averaged, phase-locked responses (P300 waves averaged in the time domain), varying in amplitude, latency, and scalp topography (review: Polich, 2007).
2) Through the analysis of frequency components of averaged, phase-locked responses (review: Başar-Eroglu et al., 1992), the frequency bands are either chosen individually per participant (Başar et al., 1997; Stampfer & Başar, 1985) or according to classic EEG frequency bands, such as delta (0.5-4 Hz), theta (4-8 Hz) and alpha (8-13 Hz).
3) Through the analysis of single-trial induced (non-phase-locked and phase-locked) responses in the P300 time window, typically with changes in M/EEG oscillations quantified as M/EEG band power (in frequency bands as above). An increase of band power relative to a control window is called event-related synchronization (ERS), and a decrease is called event-related desynchronization (Cheyne, 2013; ERD review: Pfurtscheller & Lopes da Silva, 1999).

ERS/ERD in the P300 latency window, comprising of phase-locked and non-phase-locked single-trial responses, have been reported using EEG (Yordanova & Kolev, 1998a, 1998b) or in MEG (Ishii et al., 2009). As oddball responses, the latter study found frontal ERS in the delta, theta, and alpha (with additional ERD sources related to motor execution during subjects' task-related button presses). Inferior and middle frontal gyri were also among the activated sites in an fMRI study of auditory oddball responses (Kiehl et al., 2001). It is noteworthy, in the context of M/EEG methods; phase-locked responses (time-domain averages) on the one hand, and ERS/ERD, on the other hand, offer complementary information and studying them in isolation only offers one aspect of the underlying physiological process. To this end, the present

study aims to study both the phase-locked responses and ERS/ERD at P300 latency with the high spatio-temporal resolution of MEG.

Searching for neural sources of event-related responses in MEG means to solve the ill-posed problem, which can be made well-posed by constraining the inverse solution. A commonly used assumption for this purpose is that MEG signals are a consequence of a small number of focal, temporally uncorrelated neural sources. These assumptions are at the basis of spatial filtering techniques such as beamforming (Hillebrand & Barnes, 2005; Robinson & Vrba, 1998). SAM (Robinson & Vrba, 1998), a beamforming technique, allows estimation of band power changes across the whole-brain during a given task. Instead of relying on phase-locked averaged responses, SAM uses information from single trials, which makes it ideal for the study of non-phase-locked responses as in ERS/ERD. However, by investigating only the continuous data, we might miss out on information present in the averaged data. To this end, an event-related beamformer was used to localise neural sources of the averaged activity in the auditory P300 time window.

The present study aims to localise neural generators of band power changes (ERS/ERD) as well as phase-locked responses during P300 latency by source localising both continuous and averaged data. Band power changes can occur in frequency ranges corresponding to the main frequency contents of the averaged ERP (see Demiralp et al., 1999, for single-trial events and Ishii et al., 2009 for delta ERS) or – in other frequency ranges – might reveal processes that are not detectable in the averaged P300 wave. For better spatiotemporal precision of measurement, MEG was used instead of EEG. The current study goes beyond earlier MEG studies of P300 (Nishitani et al., 1998), where the following were quantified: (a) oscillatory responses in ERS/ERD, regardless of phase and (b) phase-locked responses in the same participants. While stimuli are as in an earlier MEG study (Ishii et al., 2009), with equally task-relevant oddballs, the instruction is different: instead of responding to targets by a button press, participants in this study had to count targets mentally. Consequently, this study aimed to identify the neural sources of activity (both ERS/ERD and time-locked averaging) seen in the P300 window.

4.2 Methods

4.2.1 Participants

Ten healthy right-handed volunteers (5 females), in the age range 22-28 years participated in the study. All the participants had bilateral clinically normal hearing thresholds (as defined by the British Society of Audiology), assessed by pure tone audiometry, with no history of otological, neurological or psychiatric conditions. Before the study, all of the participants gave informed consent. The study was approved by the University of Nottingham, School of Psychology ethics committee.

4.2.2 Stimuli and experimental task

A two-tone, frequency deviant, auditory oddball task was designed and presented with NeuroBS Presentation software (http://www.neurobs.com). The sequence contained 1000 Hz (standard) and 2000 Hz (deviant) tones, each 100ms in duration (10ms rise/fall time). Out of a total of 600 trials, standards were presented 80% of the time, i.e., 480 trials and the remaining 20%, i.e., 120 trials were deviants. The order of presentation was pseudo-randomised. A fixed interval of 1500ms between stimulus onsets was used. Stimuli were presented binaurally using Etymotic ER-3A insert earphones at comfortable listening levels (65-70 dB HL), delivered via 1.5m long plastic tubes to reduce large magnetic artefacts. To ensure participants were attentive throughout the experiment, they were instructed to keep a mental count of the deviant tones whilst ignoring the standard tones. At the end of the experiment, participants were asked about the counted number of deviants. During the experiment, participants were also asked to keep their eyes open and to fixate their gaze on a fixation cross – to reduce eye-movement-related artefacts.

4.2.3 Data acquisition

MEG data were recorded using a whole-head 275-channel CTF-MEG (MISL, Coquitlam, Canada) housed in a magnetically shielded room, at a sampling rate of 600 Hz, and a 150 Hz anti-aliasing filter was used with third-order synthetic gradiometers. For the recording – the participants were in the supine position with their head inside the helmet; the head position was localised by three fiducial markers (nasion, left and right pre-auricle), which were energised at the start and end of the experiment to track subject motion. Should a participant move further than 8 mm from their initial position their data were discarded. In addition, both vertical and horizontal electrooculogram (EOG) and electrocardiogram (ECG) were acquired for artefact detection. To co-register the MEG data with individual anatomy, the head shape was digitised prior to MEG data acquisition (Polhemus Isotrak, Colchester, VT) and matched to the extracted scalp surface of the participant's T1 weighted anatomical data, using an iterative closest point algorithm. Anatomical images were obtained using a 3T MRI system (MPRAGE, 1 x 1 x 1 mm^3 resolution).

4.2.4 Data analysis

The data analysis was performed using MATLAB 2014b. To capture the non-phase-locked oscillatory components in the P300 time window, SAM beamformer was used. To capture the phase-locked components in the same time window, LCMV beamformer was applied to the averaged data. For source analysis, a multiple local sphere head model was used (Huang et al., 1999). The MEG data were visually examined for artefacts; trials with large artefacts were excluded from further analysis. The data were band-pass filtered in the 0.5-30 Hz range. For each participant, 100 artefact-free trials for standard, and deviant condition each (i.e., 200 in total) were randomly selected (out of 480 standards and 120 deviants trials) to ensure equal trial numbers across conditions. The sensor space data were baseline

corrected (-300ms to 0ms) and averaged in each condition to identify latency windows for further analysis.

4.2.5 Source reconstruction using beamforming

Source localisation of the frequency filtered data was achieved using a SAM beamformer (Robinson & Vrba, 1998), in order to estimate time courses of electrical activity on the vertices of a predefined 8 x 8 x 8 mm^3 grid. After source localisation, a volumetric pseudo-T-statistic (Vrba & Robinson, 2001) image is then obtained as:

$$T = \frac{P_{active} - P_{control}}{N_{active} + N_{control}}$$

where P_{active} and $P_{control}$ represent beamformer source reconstructed power at a given location and N_{active} and $N_{control}$ represent beamformer noise estimates for active and control windows respectively (see section **3.3.1**). For localising cortical sources associated with N1m, standard trials were contrasted in a 0 to 200ms active window and a -200 to 0ms control window (pre-stimulus baseline). For resolving the neuronal components associated with P300, the same broadband data were used. An active window was selected from deviant tones and a control window was selected from standard tones (both windows 300ms-700ms). Window limits were defined based on visual inspection of the data (**Figure 4-2**).

Prior to group analysis, SAM volumes and individual T1 weighted images were normalised to a standard MNI template using SPM8 routines (Litvak et al., 2011; http://www.fil.ion.ucl.ac.uk/spm/). These normalised SAM volumes were analysed at the group level using statistical non-parametric mapping (SnPM13, http://warwick.ac.uk/snpm Nichols & Holmes, 2001) to obtain statistical maps. Although SnPM has been developed and extensively used in PET and fMRI literature, it has also been applied for MEG data (Singh et al., 2003). The voxel-level analysis was performed using multiple subjects one sample design. Permutations tests were

performed after applying variance smoothing, with a Gaussian kernel of 8mm width. For the analysis of responses from auditory cortex and auditory belt area in the 0-200 ms window, the analysis was restricted to the superior and middle temporal gyrus as anatomically defined regions of interest, using a mask image from the AAL atlas (Tzourio-Mazoyer et al., 2002) as available in the MarsBaR toolbox (Matthew Brett, http://marsbar.sourceforge.net). For all analyses, significantly active voxels were computed using 1024 permutations at $p<0.05$ (FWE-corrected), and were overlaid on a standard MNI template using Freeview routines (http://surfer.nmr.mgh.harvard.edu), at this stage source data obtained separately from the right and left hemisphere channels were combined for visual display.

4.2.5.1 Event-related beamformers

An additional implementation of beamforming referred as the Event-Related Beamformer (ERB) was used to specifically study the phase-locked responses to both standard and deviant tones. The exact implementation of ERB is available as part of the BrainWave toolbox (Jobst, Ferrari, Isabella, & Cheyne, 2018). For details, the reader is directed to (Cheyne, Bakhtazad, & Gaetz, 2006; Cheyne, Bostan, Gaetz, & Pang, 2007), but here a summary of the analysis has been provided (see **Figure 4-1** for a schematic). Same as the SAM analysis, a multiple local sphere head model was used (Huang et al., 1999).

The normalised beamformer weights are estimated for each location in the brain from the covariance matrix of the individual trial data. Noise levels are estimated directly from the individual trial data by employing a singular value decomposition (SVD), to identify the smallest singular value of the data across the time windows. This has been shown to capture a stable noise estimate across participants (Cheyne et al., 2006). The normalised beamformer weights are subsequently used to produce a virtual electrode output for a given location (as shown in **Figure 4-1**). To arrive at an averaged phase-locked response, the time series are averaged (relative to stimulus onset). Similar to the statistical process employed for SAM beamformer, the

volumetric images generated by the event-related beamformer were subjected to permutations testing to identify statistically significant regions. To localise sources of N100m (0-200ms), standard trials were averaged and to localise the sources of P300 (300-700ms), deviant trials were averaged.

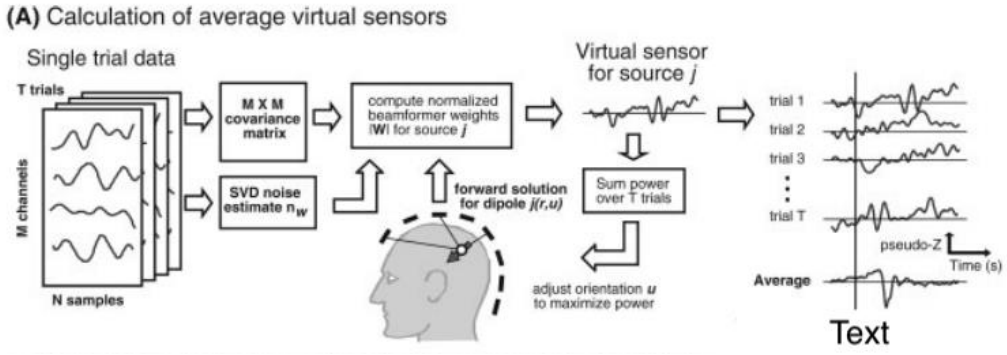


Figure 4-1 *The schematic shows the estimation of an averaged virtual electrode output using an event-related beamformer for a given location in the brain. Figure adapted from Cheyne et al. (2006).*

4.3 Results

4.3.1 Sensor level analysis

At the end of the experiment, all the participants were asked about their mental count of the deviant tones. The mental count was compared against 120 deviant trials present in the experiment to obtain percentage correct scores. All but one participant reported at least 114 out of the 120 deviant trials present in the experiment (95%, one participant at 90%). None of the subjects reported more than 120 deviants. These counts indicate that the participants were attentive through the length of the experiment.

After pre-processing, the MEG data for both standard and deviant conditions were averaged in sensor space (100 trials in each condition). Visual inspection of the grand average response to the standard tones (mean latency: 122ms, SD: ± 5, mean amplitude: 90.40 fT, ± 17.98) showed a response peaking around 120ms, corresponding with N100m (see **Figure 4-2**, plot D and corresponding topographies A-C). In response to deviant tones, broadly similar N100m (mean latency: 127ms, ± 5, mean amplitude: 97.27 fT ± 20.55) latency amplitude was seen (see **Figure 4-2**, plot E and corresponding topographies F-H). In the statistical analysis of N100m, the latency (p=0.03, paired t-test) and amplitude (p=0.02, paired t-test) were found to be significantly different between the two conditions. However, this activity is outside of the P300 latency window of interest. Comparison of averaged responses between deviants and standards showed target-only responses in the 300ms-700ms time window, reaching a peak around 380ms. The analysis of deviant tones across all the subjects revealed responses comprising of successive peaks at 235ms ± 10 (mean amplitude: 98.00 fT, ±31.93) corresponding with N2 component, and at mean latency of 380ms, ± 64 (mean amplitude: 75.86 fT, ± 10.82) corresponding with the P300 component. This step confirmed the latency windows that have consistently been reported for both N100m and P300. Only activity inside the pre-defined P300

window (300-700ms) was studied in the subsequent source analysis, contrasting deviant vs. standard responses.

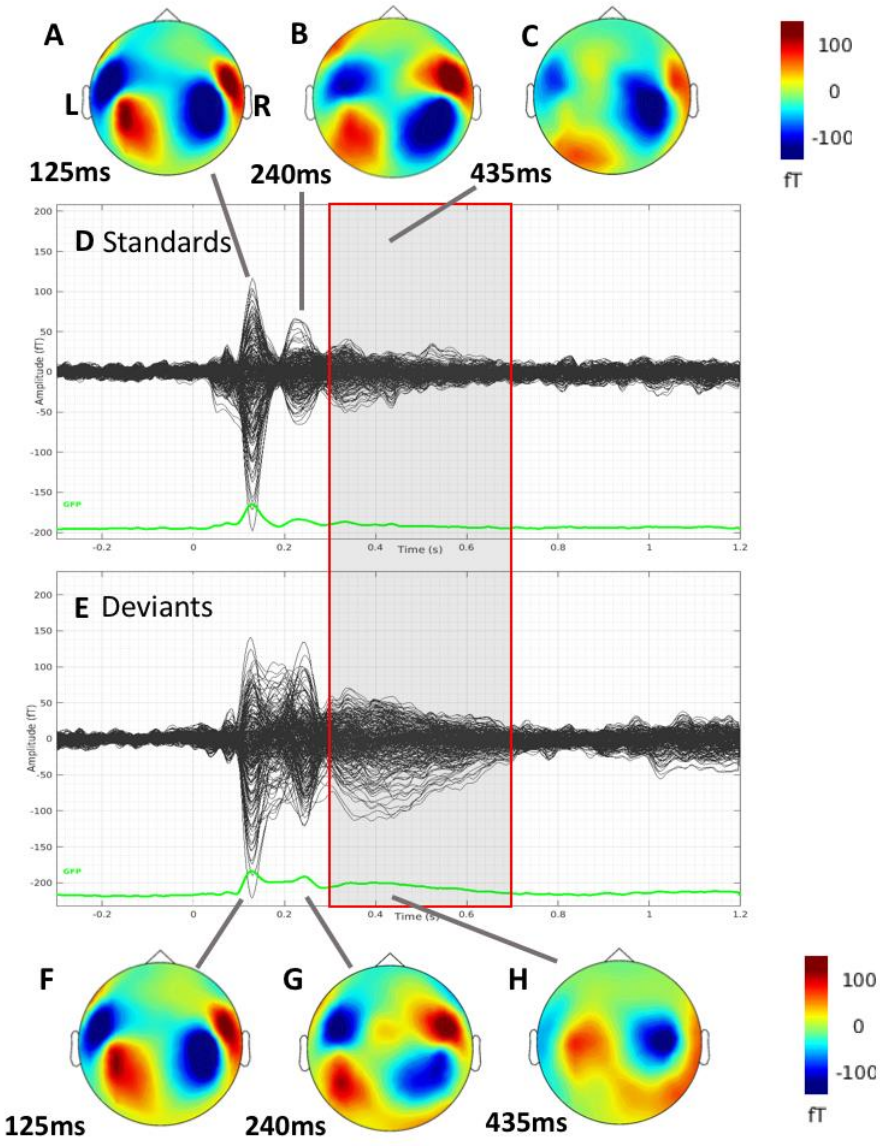


Figure 4-2 *Plot D and E show sensor space grand averages (N=10 participants) of standard and deviant tones (100 trials each). Plots A-C show field topography for standard tones and plots F-H show field topography for deviant tones. The shaded box in panels D and E shows the P300 time window. The colour bar ranges between -150 fT (blue) to +150 fT (red). L: Left, R: Right*

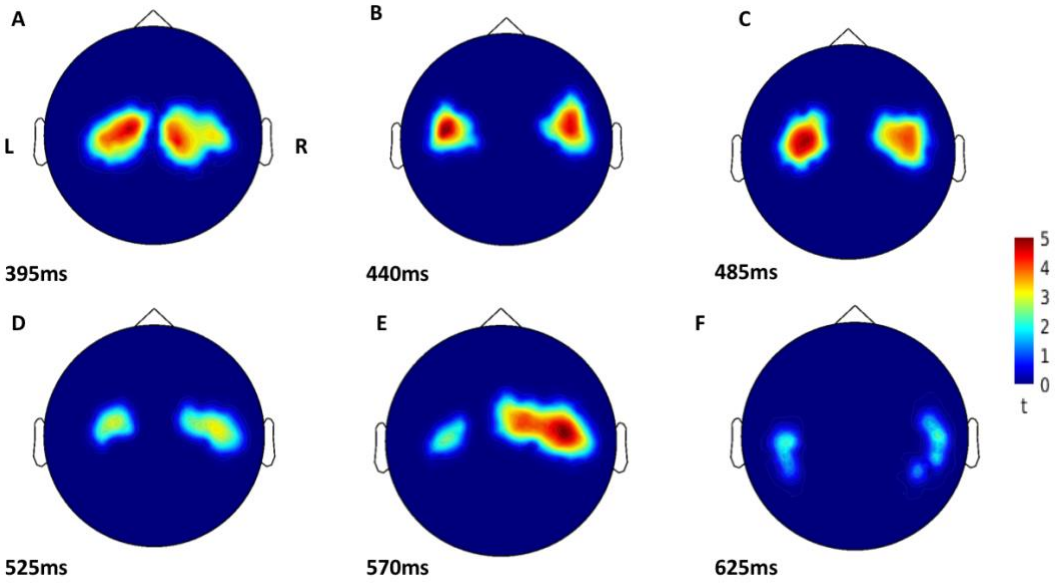


Figure 4-3 *Plots A-F show group results (N=10 participants) of cluster permutations testing (sensor x time) plotted on sensor layouts at corresponding time stamps. The plots show statistically significant activity between standard and deviant condition, with red colour corresponding to positive t-values (deviant > standard). L: Left, R: Right*

Visual inspection of the averaged responses revealed activity in the P300 time window (300-700ms) with marked differences between deviant and standard conditions. To statistically confirm this, a cluster permutations test (Maris & Oostenveld, 2007) was performed on sensor level data by contrasting standard and deviant conditions. **Figure 4-3** shows the results of this analysis. It shows strong differences spanning the temporal, central and frontal channels (p<0.05, FDR-corrected).

4.3.2 Source analysis: N100 latency window

Neural sources of band power changes at N100m latency were identified through SAM-SnPM group analysis – as statistically significant clusters (p<0.05, FWE-corrected). To localise the neural sources of N100m for standard tones using SAM, the post-stimulus interval of 0-200ms was compared against the pre-stimulus interval of -200-0ms. **Figure 4-4** shows ERS over bilateral superior and middle

temporal gyri or the auditory belt area (see coordinates in **Table 4-1**). This source localisation is consistent with sensor level field topography seen for peak N100m (**Figure 4-2**, plot A) and with existing literature on N100m (phase-locked responses: Mäkelä & Hari, 1990; Hari et al., 1980; ERS/ERD: Steinsträter et al., 2007).

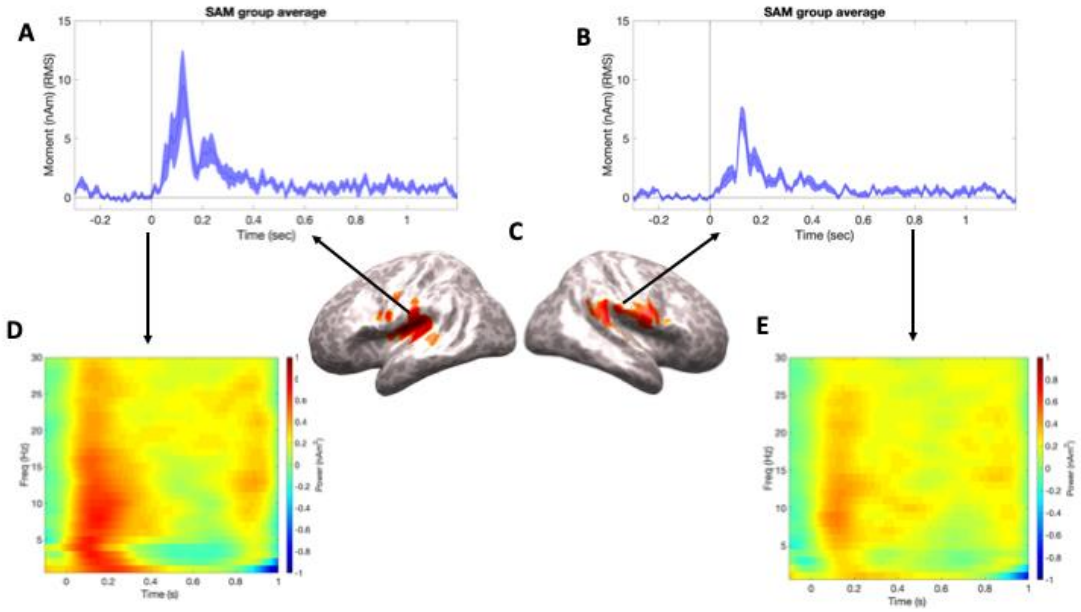


Figure 4-4 *Group results (N=10 participants) of SAM analysis showing statistically significant (p<0.05, FDR-corrected), regions of ERS to standard tones (plot **C**). Plot **A** and **B** show reconstructed virtual electrode (VE) output from the peak voxel in the superior temporal region in the left and right hemisphere respectively (shaded area showing SD). The results were obtained by contrasting post-stimulus window (0-200ms) against a pre-stimulus window (-200-0ms) of the standard tones. Plot **D** and **E** showcase averaged spectrograms obtained after transforming the individual VE output in time-frequency domain using Hilbert transform.*

Table 4-1 *Anatomical locations of peak clusters (p<0.05, FDR-corrected) found using SAM-SnPM analysis (N100 time window: 0-200ms).*

Anatomical Locations	**Frequency bands (Hz)**	**Time window (ms)**	**MNI co-ordinates mm (X Y Z)**
Left auditory cortex	1-30	0-200	-54 -32 6
Right auditory cortex	1-30	0-200	58 -48 14

Neural sources of averaged activity corresponding with N100m latency were identified using event-related beamformer. Results in ***Figure 4-5*** were obtained by averaging the standard trials in source space. The results localised the averaged activity in the bilateral auditory cortices. For N100m, the extent of response was visually larger for averaged responses than ERS (**Figure 4-4**). Cluster permutations test was performed to identify regions with statistically significant activity (see ***Figure 4-5***). This analysis localised the neural sources in the bilateral auditory belt areas, showing an overlap between the neural sources of band power changes (see **Figure 4-4**) and averaged activity.

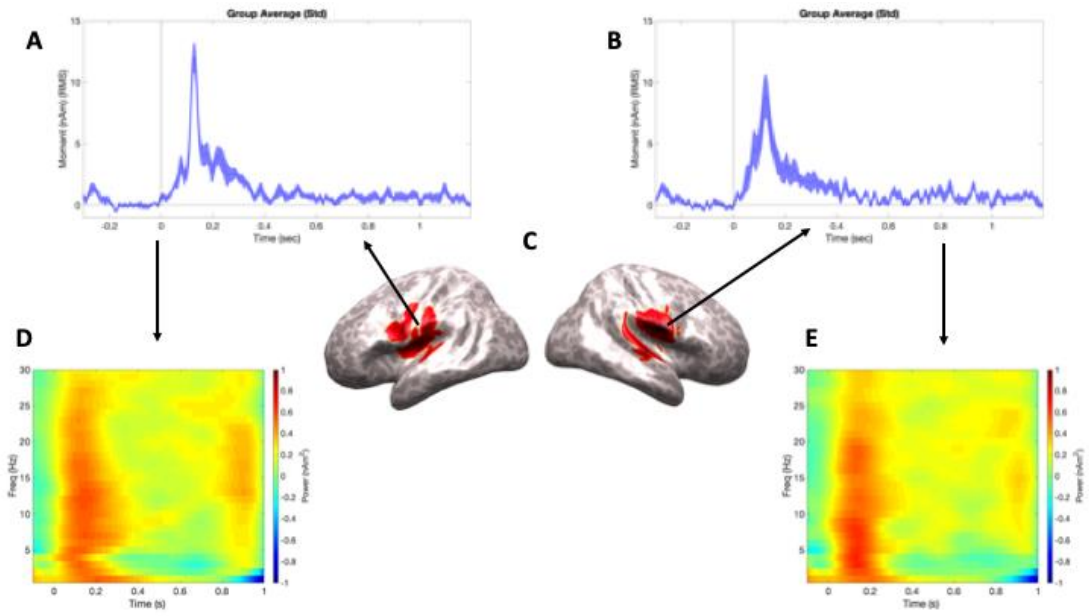


Figure 4-5 *Group results of the event-related beamformer analysis showing statistically significant regions (p<0.05, FDR-corrected) to standard tones (plot **C**). Plot **A** and **B** show reconstructed virtual electrode (VE) output from the peak voxel in the superior temporal region in the left and right hemisphere respectively (shaded area showing SD). The results were obtained by contrasting averaged post-stimulus window (0-200ms) against a pre-stimulus window (-200-0ms) of the standard tones. Plot **D** and **E** showcase averaged spectrograms obtained after transforming the individual VE output in time-frequency domain using Hilbert transform.*

Table 4-2 *Anatomical locations of peak clusters (p<0.05, FDR-corrected) found using event-related beamformer (N100m).*

Anatomical Locations	**Frequency bands (Hz)**	**Time window (ms)**	**MNI co-ordinates mm (X Y Z)**
Left auditory cortex	1-30	0-200	-54 -24 14
Right auditory cortex	1-30	0-200	58 -16 14

4.3.3 Source analysis: P300 latency window

To localise the neural sources of ERS in the P300 latency window, group-level SAM-SnPM analysis was performed by contrasting deviant tones with standard tones, both at 300-700ms post-stimulus intervals. To identify the underlying oscillatory dynamics, this analysis was performed for the 0.5-30 Hz signal. An increase in power or ERS was seen bilaterally in bilateral inferior frontal gyri, with sources extending to the dorsal prefrontal cortex in the left hemisphere (p<0.05, FWE-corrected, **Figure *4-6***). As seen from the spectrograms, the activity was seen across all the frequency bands but it was highly localised in theta and alpha bands with the biggest cluster primarily in the theta band.

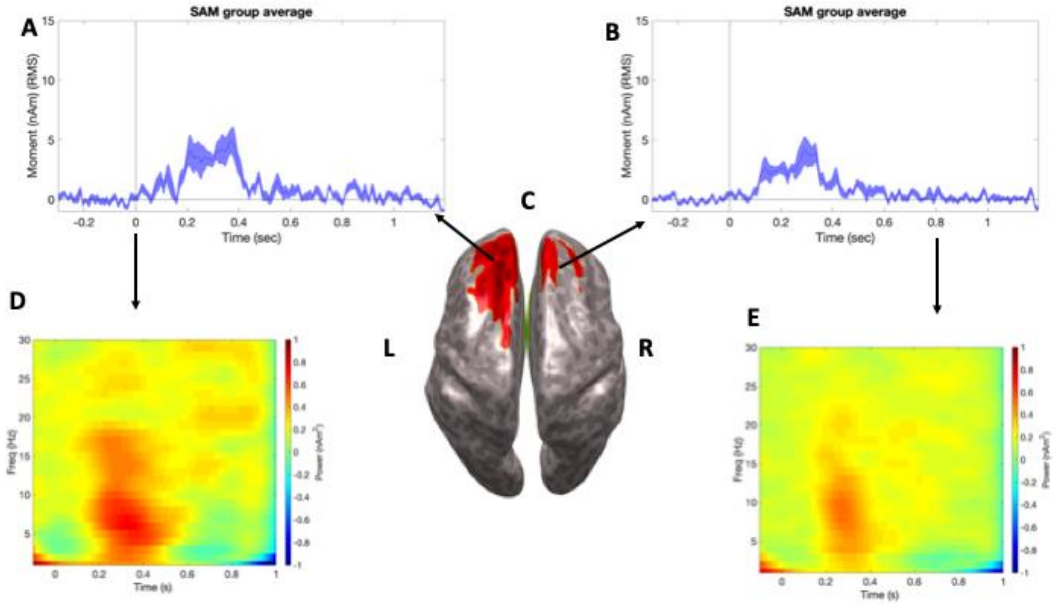


Figure 4-6 *Results of SAM analysis showing statistically significant (p<0.05, FWE-corrected), regions of ERS in theta band (4-8 Hz) for deviant tones, in frontal and prefrontal regions (plot C). Plot **A** and **B** show reconstructed virtual electrode (VE) output from the peak voxel in the bilateral inferior frontal gyri (shaded area showing SD). The results were obtained by contrasting post-stimulus window (300-700ms) of deviant tones against the post-stimulus window (300-700ms) of standard tones. The group activity maps (N=10 participants) have been overlaid on the template brain. Plot **D** and **E** showcase averaged spectrograms obtained after transforming the individual VE output in the time-frequency domain using Hilbert transform.*

The analysis did not reveal any neural sources of ERD in our pre-defined window. These results also show a large left lateralised response for ERS (peak locations in **Table 4-3**).

Table 4-3 *Anatomical locations of peak clusters (p<0.05, FDR-corrected) found using SAM-SnPM analysis (P300).*

Anatomical Locations	**Frequency bands (Hz)**	**Time window (ms)**	**MNI co-ordinates mm (X Y Z)**
Left IFG	1-20	300-700	-22 40 26
Right IFG	1-20	300-700	18 40 26

IFG: Inferior frontal gyrus

The time-locked (or phase-locked) averaged responses in the P300 time window were localised using event-related beamforming. This analysis revealed highly focal

neural sources mainly in prefrontal cortex (**Figure 4-7**). As it can be seen from the spectrograms, the activity was mainly in theta and alpha band (with some spread even in higher frequencies).

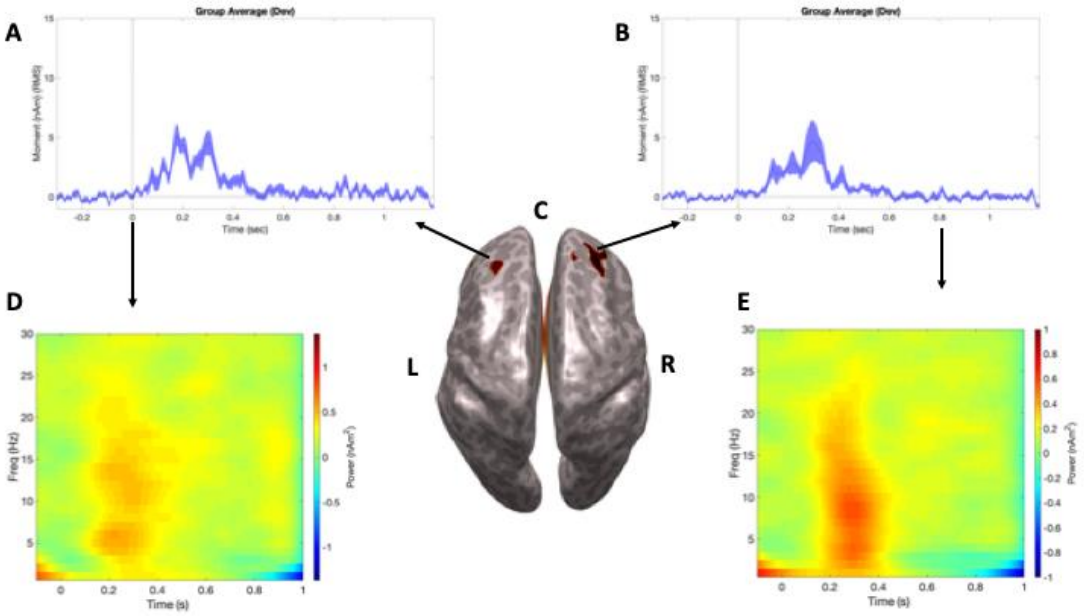


Figure 4-7 *Group results of the event-related beamformer analysis showing statistically significant (p<0.05, FDR-corrected) to deviant tones (plot **C**). Plot **A** and **B** show reconstructed virtual electrode (VE) output from the peak voxel in the prefrontal cortex in the left and right hemisphere respectively. The results were obtained by contrasting averaged post-stimulus window of deviant tones (300-700ms) against a post-stimulus window of standard tones (300-700ms). Plot **D** and **E** showcase spectrograms obtained after transforming the VE output in the time-frequency domain using Hilbert transform.*

Table 4-4 *Anatomical locations of peak clusters (p<0.05, FDR-corrected) found using event-related beamforming (P300).*

Anatomical Locations	**Frequency bands (Hz)**	**Time window (ms)**	**MNI co-ordinates mm (X Y Z)**
Left IFG	1-30	300-700	-22 40 26
Right IFG	1-30	300-700	18 40 26

IFG: Inferior frontal gyrus

4.4 Discussion

The current study investigated the neural sources of P300-latency responses to mentally counted auditory oddballs using MEG. The activity in the P300 latency window (300-700ms) was quantified by studying band power changes and phase-locked responses in the same participants. As the central result of this study, the SAM-SnPM analysis identified frontal theta and alpha ERS (in attended deviants relative to standards), in line with earlier EEG and MEG studies (Ishii et al., 2009; Yordanova & Kolev, 1998b, 1998a). It must be noted that the spectral activity was seen across the frequency bands, however, it was highly time-locked with stimulus onset. ERS to targets in P300 time window was spatially distinct from ERS in N100 time window, observed for deviants > standards in the bilateral and middle superior temporal regions (auditory belt areas) in line with sources found from averaged evoked auditory responses (Mäkelä & Hari, 1990; Hari et al., 1980). The use of event-related beamformer to study the averaged responses in the P300 time window, allowed us to localise highly focal responses in the prefrontal cortex, which show right laterality. The results indicate that unlike sensory-evoked responses such as the N100m, the cognitive evoked responses involve more than just the sensory cortices. Therefore, to better understand P300's underlying physiological process, it is important to study both ERS and the time-locked responses.

4.4.1 Frontal ERS responses to oddballs

For the frequency range studied here, theta and alpha, the sources of oddball responses were frontal, in line with an earlier ERS-based study (Ishii et al., 2009), which used a task with button presses to elicit P300. However, the activation found in the present study was more widespread than what has previously been reported. Frontal areas were among the sources found from averaged P300 responses in MEG (Nishitani et al., 1998). Frontal sources have also been found for change detection without task relevance, manifest in MMN responses to oddballs (as sources of ERS in wide-band filtered data at MMN latency, Lappe et al., 2013) and as sources of

averaged MMN responses (Cheng et al., 2013). In EEG, phase-locked responses to attended targets are typically maximal over parieto-temporal sites (P3b), and responses to novel deviants are maximal over frontocentral sites (P3a review: Polich, 2007). As a common feature across the earlier MEG study (Ishii et al., 2009), and the current experiment, deviant vs. standard tone discrimination was very easy (2000 Hz vs. 1000 Hz). Subjects would have attended only to the deviants and suppressed the standards, without any effortful listening. It is conceivable that a more complex task could have elicited parietal responses as well.

4.4.2 Theta and alpha band components

The current MEG data demonstrated a robust oddball related theta ERS at P300 latency in dorsolateral prefrontal regions, in line with earlier MEG oddball responses with button press task (Ishii et al., 2009). The result is also in line with the topography of EEG responses to auditory oddballs: theta ERS is strongest at frontal sites (Fz) compared with Cz and Pz (Yordanova & Kolev, 1998a).

In the alpha frequency range, bilateral frontal ERS was observed – again as in an earlier MEG study with button press task (Ishii et al., 2009), and also in line with frontal alpha ERS to auditory oddballs in an EEG study (Yordanova & Kolev, 1998a). It is conceivable that prolonged alpha responses are manifest in ERS (Başar et al., 1997; Öniz & Başar, 2009; Stampfer & Başar, 1985). Such alpha ERS is not detectable from averaged P300 responses, which are dominated by delta and theta frequencies (Başar et al., 1997). However, in our data, we do see activity across the frequency spectrum (time-locked to event onset) but more prominently in the theta and alpha range. Alpha ERS has been linked to sensory gating through inhibition (Jensen & Mazaheri, 2010). For example, during lateralized spatial attention, alpha increases in parieto-occipital areas ipsilateral to the attended visual hemifield (Capotosto et al., 2009), and in somatosensory cortex ipsilateral to the attended hand during tactile stimulation (Haegens et al., 2010). Furthermore, alpha ERS is observed in the somatosensory cortex during visual attention (Bauer et al., 2012). The pattern of

alpha decreases in areas processing the attended modality and increases in areas processing the unattended modality seems to be particularly prominent when active blocking is needed due to high task demands (Frey et al., 2015). However, unlike the above studies, the current experiment – like Ishii et al., (2009) – required participants to detect a target stimulus that was not spatially separate from standards, occurred in the same modality as standards, and was easy to detect. Accordingly, selective attention within a modality as in the present experiment is not directly comparable to conditions in the above studies.

4.4.3 Time- (Phase-) locked responses

The source configuration of phase-locked responses was investigated using event-related beamformer. Auditory cortex, with standard activity compared against the baseline in the beamformer analysis (0 to 200ms vs. -200 to 0ms), has been identified as a source region of activity in fMRI (Kiehl et al., 2001; Yoshiura et al., 1999). In the analysis, the neural sources of phase-locked responses (at P300 latency, 300-700ms) were highly focal than sources of band-power changes seen with SAM-SnPM analysis. Temporoparietal sources, for phase-locked responses, have been implicated with P300 based on lesion studies. Reduction of P3b in auditory modality has been reported after the temporo-parietal lesions (Knight et al., 1989; Verleger et al., 1994). The source region implicated with P300, inferior frontal gyri and prefrontal cortex, were found here in source analysis from averaged responses and also in SAM analysis for band-power changes. It is also worth noting that neural sources obtained by localising the averaged activity showed a right dominance, whereas it was left lateralised for the SAM analysis. The prefrontal cortex has been implicated with P300 based on an fMRI study (Kiehl et al., 2001). Responses from midline structures found here for phase-locked responses only could correspond to activation in posterior cingulate, reported in fMRI study by (Kiehl et al., 2001) as a source region for target P3.

4.4.4 Processes underlying P300

The P300 event-related response reflects cortical activity related to the processing of task-relevant ongoing stimuli. Upon completion of the early sensory evaluation of the stimulus, there is an active attention-led comparison between the sensory representation of the previous stimulus and the incoming stimulus. This process is distinctly different from MMN as a stimulus feature mismatch response (Näätänen et al., 2007). However, if no stimulus-related change is detected then the sensory trace is maintained; and only the evoked responses, which are lower in the hierarchy of events, are recorded (Polich, 2007), *viz*., the sensory-evoked responses, such as N100 or P200.

While P300 responses can also occur after unexpected stimuli (P3a with a fronto-central maximum in EEG), the current study addresses the "classic" P300 waves elicited by task-relevant stimuli (P3b with parieto-central maximum). As a process underlying P300, it has been postulated that each stimulus is compared with a working memory representation of the preceding stimulus and subsequently – in case of oddballs – the mental model of the stimulus environment is updated (Polich, 2007). Other proposed processes are the closure of a structured sequence of stimuli by an expected event (Verleger, 1988) or event categorization – a decision whether or not a stimulus matches a template (Kok, 2001). Beyond these processes – all related to stimulus evaluation – it has been suggested that P300 occurs when stimulus classification is transformed into a response (Verleger et al., 2005). To better understand the role of non-phase-locked neural oscillations, comparison with other tasks is needed.

First, memory processes are required within context updating and during mental counting. Using EEG, frontal theta ERS has been observed during successful encoding and during correct retrieval from memory (Klimesch et al., 1997). Second, it is possible that selective attention drives theta responses. The contribution of memory processes to P3b has been questioned on the basis of neuropsychological (lesion) data (Verleger, 2008). Stronger frontal theta ERS for oddball detection vs. 1-back task

was found in the visual modality, suggesting a basic attentional (rather than working memory) correlate of frontal ERS in EEG (Krause et al., 2000; Missonnier et al., 2006). Also, medial prefrontal activation has been found in MEG as a correlate of focused attention (Ishii et al., 2014). The exact role of higher frequency activity seen with both the source analysis approaches is less clear and cannot be directly probed. Of major interest for future studies would be theta band connectivity between brain structures. A recent MEG study revealed theta-band connectivity between the ventromedial prefrontal cortex and the hippocampus during MMN, a response that is distinct from P300, which involves change detection (Garrido et al., 2015). Also during MMN, increased theta phase-locking in the right frontal channels was observed in MEG sensor space (Hsiao et al., 2009).

In conclusion, analysis of band power changes (ERS) in the P300 window revealed higher clusters of activity primarily in theta and alpha band with neural sources in the prefrontal and midline regions. Whereas, analysis of the phase-locked responses in source space revealed highly focal activity in the prefrontal cortex, with a right lateralised response. The profile of regional activation differed between ERS and phase-locked responses. Consequently, different source localisation methods contributed to comprehensive source analysis of the elusive auditory P300.

CHAPTER 5

5 From functional connectivity to multilayer networks

Précis

It has become increasingly common to model the human brain as a network, which can further be studied using graph theoretical approaches. This chapter presents the basics of functional connectivity analysis and basics of graph theory as applied to systems neuroscience (or network neuroscience). A generalised analysis pipeline is presented, which can easily be applied to a range of brain imaging modalities. Building on these concepts, the chapter also introduces the multilayer network framework (i.e., a network of networks) and various multilayer network metrics. Graph theoretical methods will be applied in the following two chapters (**6 and 7**). Studying the effects of sensorimotor training on resting-state MEG data (**chapter 7**) required the development of a novel normalisation method. This chapter lays the theoretical foundation on which the normalisation method was developed and tested in **chapter 6**.

5.1 Estimating functional connectivity

Once the sensor space data is projected in source space, it can be analysed further by means of functional connectivity. Functional connectivity is defined as the statistical dependency between two or more spatially distinct regions in the brain (see review: Friston, 2011). In the case of fMRI, functional connectivity can be determined by estimating Pearson's correlation of BOLD time courses (as in **section 6.2.1**). However, in the case of MEG, due to its inherent rich spectral nature, functional connectivity can be determined by multiple different methods.

Source reconstruction gives rise to a significant confound called signal leakage. Due to the ill-posed nature of the inverse problem, source reconstruction often leads to blurring of the signal in source space. In other words, a point source appears to spread over a finite source space. This problem can become more pronounced due to errors in forward modelling or co-registration or failure to meet the assumptions of the inverse solution. Any combination of these errors can have an immense impact on MEG functional connectivity estimates.

This section briefly addresses the problem of signal leakage and the proposed correction schemes. Subsequently, the measurement of functional connectivity from source projected MEG data by using amplitude envelope correlations (AEC). Out of the connectivity metrics recently evaluated by Colclough et al. (2016), AEC was shown to have highest reliability. Plus, there is also evidence that suggests a spatial overlap between functional networks extracted using AEC in MEG and fMRI (Brookes et al., 2011a; Brookes et al., 2011b). This feature is of particular interest in **chapter 6**, where resting-state fMRI and MEG data obtained in the same participants are evaluated. As a result, this thesis primarily focused on AEC as a measure of functional connectivity for MEG data (**chapters 6 and 7**) and Pearson's correlation coefficient for fMRI data used in **chapter 6**.

5.1.1 Signal leakage

Resting-state analysis of MEG data has provided independent validation of functional networks typically reported with fMRI. By applying connectivity analysis tools directly from fMRI to MEG, there is a risk of identifying spurious correlations.

This is chiefly because of the ill-posed inverse problem, as few hundred SQUID sensors cannot accurately estimate an unknown number of source configurations. The reconstructed activity often manifests itself as the zero-phase-lag correlation between any two regions of interest, whereas a genuine signal will always exhibit some temporal delay. This is typically referred to as signal leakage, as reconstructed time courses often appear to spread over a small source space. Therefore, signal

leakage proves to be a hurdle for whole-brain connectivity analysis as it impairs an appropriate interpretation of the data. The extent of signal leakage is heavily dependent on the assumptions of the inverse solution, source strength, and source location. Beamformers have been shown to be more effective at restricting the field spread than minimum norm solutions (Schoffelen & Gross, 2009), but neither of the source localisation methods is fully accurate.

The aim of an atlas-based method is to estimate connectivity between larger patches of the cortex. However, this approach makes signal leakage highly likely as neighbouring voxels often have similar temporal characteristics. It is precisely for this reason that signal leakage correction is of paramount importance when estimating any functional relationships between ROIs in a whole-brain analysis. Signal leakage correction is typically applied by removing all the zero-phase-lag correlations between all the ROIs. In this thesis, a multivariate symmetric orthogonalisation method is used (Colclough et al., 2015). This method, for every ROI, produces an independent set of orthogonal time course. The solution thus produced after orthogonalisation, is unique and is only slightly different from the original time courses. Typical analysis steps involved in leakage correction are as follows –

First, the closest orthogonal time courses (for which there exists a simple analytical solution) are identified. Second, using an iterative approach, the solution is optimised until the corrected vectors are close to the original uncorrected time courses. By definition, the orthogonalization procedure removes all zero-phase-lag correlations between all the ROIs. Therefore, any remaining correlations (after correction) between the amplitude envelopes of the ROIs are thought to demonstrate a true biological coupling. After the correction, AEC is used to derive functional coupling for each time course in frequency bands of interest across all the participants resulting in a 78 x 78 adjacency matrix for every frequency band for every participant. Typically, these adjacency matrices are averaged over subjects within each band to generate a group level representation.

5.1.2 Amplitude envelope correlation

As stated before, functional connectivity is a statistical dependency between two-time courses. For source projected MEG signal, it can be measured using either amplitude envelope coupling (i.e., power relation between the two signals) or by measuring the phase synchronisation (phase coupling) (see review: Engel et al., 2013). While phase-based, and amplitude-based methods tend to focus on distinctly different aspects of the MEG signal, they serve as a proxy for the same underlying functioning. Functional connectivity analysis has recently seen rapid growth in electrophysiological research. However, this analysis has primarily been developed in the context of fMRI research. Early research has robustly demonstrated a presence of spatial correspondence between patterns of connectivity seen in fMRI and oscillatory activity as recorded by electrophysiological measures (Brookes et al., 2011; Hipp et al., 2012).

The oscillatory interactions can be investigated by estimating the relationship between source-projected time courses. This is achieved by first decomposing the time-based information into a spectro-temporal representation and then extracting the amplitude envelopes. There are several signal processing methods that can be used to extract the amplitude envelopes, such as Morlet transform or Fourier transform but the most commonly used in electrophysiological research is the Hilbert transform. Here, the spectro-temporal representation is estimated by decomposing the signal into small frequency bins (bandpass signals) and then by estimating an analytic signal of each of those components. A correlation is then estimated between the analytical signals to identify similarities. In the presence of a higher correlation, the regions are said to be functionally connected. There are several other connectivity metrics that have specifically been used in M/EEG research, for example, coherence (phase synchronisation), phase-locking value, phase-amplitude coupling, etc., (see review: Bastos & Schoffelen, 2016). In **chapters 6 and 7** where AEC has been used, it was computed for 78 cortical regions defined using the Automated Anatomical Labelling (AAL) atlas (Tzourio-Mazoyer et al., 2002). Time courses of

activity were generated for each of the 78 regions using beamformers for MEG and by estimating average BOLD time series for fMRI. Connectivity analysis was then performed on the 78 representative time courses. The details of this method and how it has been applied within the specific context of the experimental work has been explained in the individual experimental chapters (**chapters 6 and 7**).

5.2 Primer on graph theory

The human brain is widely considered to be a complex network that can be studied by graph-theoretical approaches. In such a description, nodes in the network correspond to anatomical regions, and links typically refer to either structural or functional connections between those regions. Graph or network theory has been applied successfully to networks derived from a wide range of modalities, for example from fMRI (Bassett et al., 2008), MEG (Stam, 2014), EEG (Stam et al., 2007), diffusion tensor imaging (DTI, Iturria-Medina et al., 2008), and structural covariance (He, Chen, & Evans, 2007). A key advantage of such an approach is that network theory enables characterisation of both the spatial organisation and the strength of the network connections (Bassett & Sporns, 2017). Using this reductionist approach, neuroscientists often distil the complexity of the human brain to a handful of nodes; this offers a mathematically concise description of brain regions and all the possible interactions between them. The distilled mathematical description is often referred to as the human connectome or simply, the wiring diagram of the human brain. Various metrics, describing both nodal and global topological network characteristics, have been shown to provide useful quantitative descriptions of networks in order to reveal common pathways across diseases (Crossley et al., 2014), and to differentiate brain states during cognitive tasks (Braun et al., 2015; Micheloyannis et al., 2006).

The idea of the human brain as a complex network that exists on various spatial and temporal scales has been supported by a plethora of research studies (see review: Betzel & Bassett, 2017). At a macroscopic level, the human connectome characterises a network of myelinated fiber tracts, that provide a anatomical infrastructure for brain regions. The structural infrastructure is at the heart of resulting functional networks, which describe statistical dependencies between brain regions (see **section 5.1**).

By investigating functional brain connectivity, one can only infer the strength of connections between brain regions, but by modelling them as graphs, we can study the patterns of these connections (basics of graphs are summarised in **Figure 5-1**). In this regard, graph theory can be viewed as a common language that can be used to study networks across various disciplines. Naturally, like any other language, graph theory comes with its own syntax and semantics. To understand how principles from graph theory can be applied to brain connectivity data, it is useful to define some key concepts. These include 1) nodes, edges, graphs, 2) unweighted and weighted graphs and, 3) directed graphs.

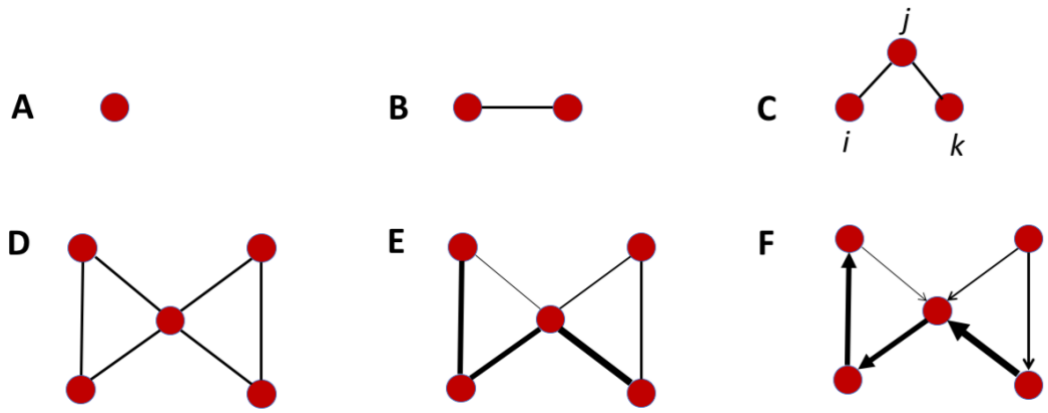


Figure 5-1 *Building blocks of graphs. A: node or vertex, B: a simple graph showing the presence of an edge or link between the two nodes, C: degree: number of connections incident on a given node (node j has a degree of 2), path length: distance from node i to node k (2); D: undirected, unweighted graph; E: undirected, weighted graph (weights correspond to the thickness of lines); F: directed, weighted graph.*

1) Nodes, edges, and graphs

A node or vertex is the most fundamental unit of a graph (**Figure 5-1A**). In the context of systems neuroscience, a node would correspond to a brain region. An edge or link (**Figure 5-1B**) indicates a presence of connections between given nodes. Putting these concepts together, a graph G is a set of nodes N and a set of edges E_{ij} (1<=i, j <=n, i~=j), where edges describe some relationship between the nodes.

2) Unweighted and weighted graphs

An unweighted graph simply indicates the presence or absence of connections between nodes (**Figure 5-1D**). On the other hand, a weighted graph is the one for which edges have some weights associated with them (**Figure 5-1E**). For example, the weights in these graphs could be quantitative estimates of functional connectivity derived from M/EEG or fMRI.

3) Directed graphs

A directed graph is the one that has directed edges, designating a directionality in information flow (**Figure 5-1F**). For example, a graph representing a causal relationship between brain regions.

5.3 Extracting functional brain networks

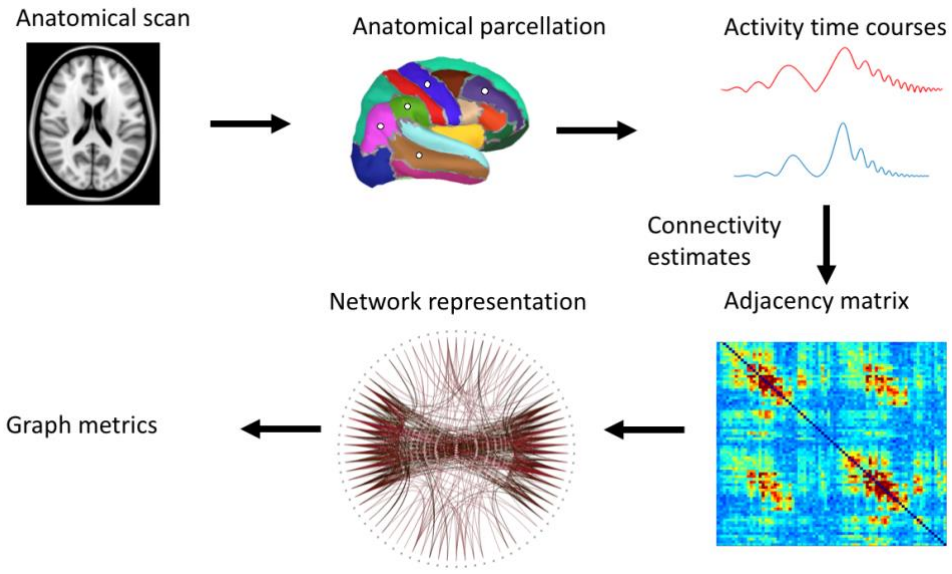


Figure 5-2 *Schematic representation of a typical analysis pipeline used in graph-theoretical analysis of brain imaging data. Based on anatomical scans. the brain is parcellated into regions (here 78 regions based on AAL atlas). For each of the 78 regions, activity time courses are obtained (in the case of MEG: amplitude envelopes for 2 out of 78 time courses shown). 78 x 78 connectivity values are computed, displayed here (a) in adjacency matrix where each of 78 x 78 node is coloured according to connection strength (red: strongest connections) and (b) as network representation where 78 regions are ordered in a circular plot and connections are shown as connecting lines. The network is then evaluated using various graph metrics.*

This section describes a general-purpose analysis pipeline that can be used to model the human brain as a network using various brain imaging modalities. It must be noted that the inferences drawn from this analysis would depend on the methodological constraints posed by the method used to record the brain activity. Limitations of brain imaging methods are not limitations of graph theory *per se*. The analysis pipeline can be viewed as a multistep process, which can be adapted according to the imaging modality (**Figure 5-2**).

As with any neuroimaging methods, some level of pre-processing is required. The aim of pre-processing is to obtain artefact free data segments; this might include removal of physiological and environmental noise. Pre-processing pipelines are now relatively well established in both fMRI (see best practices: Poldrack et al., 2016) and in MEG (see best practices: Gross et al., 2013). For pre-processing choices in connectivity studies of this thesis project, see **chapters 6** and **7**.

5.3.1 Defining nodes of the network

Network analysis starts by defining nodes/brain regions in the network. This is achieved by dividing the anatomical scan of the brain into small anatomical regions, also known as patches or parcels. These can be based on various anatomical atlases such as Desikan-Killiany (Desikan et al., 2006), Destrieux (Destrieux et al., 2010), AAL (Tzourio-Mazoyer et al., 2002) or based on histologically defined regions (Eickhoff et al., 2005) or diffusion-weighted imaging (DWI) data. The motivation behind anatomical parcellation is that performing a whole-brain connectivity analysis using the entire brain volume is computationally expensive and potentially non-informative. Therefore, the aim is to identify a parcellation scheme that best approximates the underlying activation. For instance, if one selects an anatomical atlas with a finer resolution, then the resulting network will be dense and difficult to visualise if one uses too coarse a resolution and the network might not provide an adequate representation of the underlying network. In this thesis, AAL atlas has primarily been used as it has been shown to have a spatial resolution that can be achieved using electrophysiological methods (Hillebrand & Barnes, 2002). M/EEG users can also make use of the standard electrode arrays as nodes (e.g., for EEG – 10-20 system or for MEG – sensor positions). However, sensor level analysis is not recommended (Schoffelen & Gross, 2009).

5.3.2 Identifying relationships between the nodes

For each parcel defined in the previous step, time courses of activity are estimated, which allow some continuous measurements of relationships between the nodes. For example, this could be the estimation of functional connectivity in M/EEG sensor space or source space (both in time or frequency domain) or estimation of anatomical connectivity using probabilistic mapping of diffusion data. For M/EEG, estimating source-level connectivity is the recommended approach (Schoffelen & Gross, 2009).

In this thesis, amplitude envelope correlations are used on source localised MEG data (LCMV beamformer) to estimate functional connectivity between AAL regions. However, any other measure of functional connectivity (e.g., imaginary coherence) or causal connectivity (e.g., Granger causality) can also be used. For the fMRI data used in **chapter 6** functional connectivity between AAL regions is estimated using Pearson's correlation.

5.3.3 Representing a graph

The pairwise relationships between all the nodes of the network are summarised in an adjacency matrix. For a given unweighted graph with *N* nodes, the adjacency matrix *A* is a square matrix (N x N), such that A_{ij} is 1 when there is a presence of a link (connection) between node *i* and *j*, and 0 when there is the absence of a link. The diagonal elements of this matrix are usually set to 0 as they reflect connections of brain regions with themselves. Such binary adjacency matrices are typical of structural imaging data. However, in the context of functional imaging data weighted adjacency matrices are used, where the elements indicate the strength of connections between two nodes (see colour coded adjacency matrix in **Figure 5-2**). The weighted adjacency matrices can also be binarized by only selecting connections

that are above a certain threshold. However, this approach can be an issue as it can alter connections that are potentially biologically relevant.

5.3.4 Quantifying the network behaviour

After modelling the brain as a network, various network parameters can be used to quantify its behaviour, such as degree or path length (**Figure 5-1**). These parameters can subsequently be compared against a known null model to identify significant effects or as a between-group comparison (e.g., healthy controls vs patients with neurological pathology).

Each of the steps described above is an experimental choice and can potentially influence the final results. Therefore, these analysis steps deserve careful consideration that is in line with the experimental hypothesis. In **step 5.3.3** described above, the choice of the threshold used to create a graph representation deserves special attention as different thresholds tend to generate graphs of variable sparsity or connection density. A commonly used solution to circumvent this problem is by assessing network properties over a wide range of thresholds. The network properties can be assessed using a large number of parameters (discussed in the next **section 5.4**). These parameters are subsequently compared against a null distribution with the same number of nodes and links. Statistical testing of the network parameters is usually performed using non-parametric testing.

5.4 Graph metrics

The topological properties of a brain network can be quantified by employing a wide variety of graph metrics, some exemplars are discussed below. It is unclear which of these metrics are best suited for quantifying brain networks. However, over the years, some metrics more than others have gained considerable popularity among neuroscientists.

5.4.1 Degree

The degree of a given node is the total number of connections/links it has to the rest of the network (**Figure 5-1**). Node degree (*k*) is the most basic graph metric, and the majority of the other graph measures are often derived from degree. An important parameter derived from degree is the degree distribution. In random networks – where the probability of all to all links is equal – degree distribution is Gaussian. On the other hand, complex networks have non-Gaussian node degree distribution, which is skewed towards a high degree. In the-scale free network case, the node degree distribution follows a power law.

5.4.2 Path length

The path length is the number of links travelled to reach one node from another. For a given unweighted graph, the shortest-path length between the nodes *i* and *j* is the path with the least number of links between them. The mean shortest-path length L_G is the mean over all the node pairs.

$$L_G = \frac{\sum_i^n \sum_j^n A_{ij}}{n(n-1)} \qquad \textbf{(5.1)}$$

A short mean path length indicates higher global efficiency, typically seen in random and complex networks. Naturally, networks with a higher mean path length have lower global efficiency.

5.4.3 Clustering coefficient

If the nearest neighbours of a given node in the network are connected with one another, then they are said to have formed a cluster. The clustering coefficient is a quantity that provides an index for the total number of links present in the cluster, divided by the total number of possible links. The clustering coefficient C_G can be calculated as

$$C_G = \frac{2E_i}{k_i(k_i-1)} \quad \textbf{(5.2)}$$

Here, E_i is the total number of links present in the cluster (*i*'s nearest neighbours), and k_i is the total number of neighbours. Generally, random networks tend to have a lower clustering coefficient, whereas complex networks tend to show a higher clustering coefficient.

5.4.4 Small worldness

The small-world property, popularly known as six degrees of separation (Milgram, 1967), states that any two individuals around the world are connected to each other via six introductions (or less). Similar to this property seen in social networks, human brain networks have also been shown to be "small world" (Bassett & Bullmore, 2006; Watts & Strogatz, 1998), and this property is often used as an index of network efficiency. According to (Watts & Strogatz, 1998), a network G is said to be a small world if it fulfils the following criteria measured against a random network –

1) an equal or smaller shortest-path length

2) a significantly higher clustering coefficient (Watts & Strogatz, 1998; Humphries & Gurney, 2008).

$$\gamma_G = \frac{C_G}{C_{rand}} \quad \textbf{(5.3)}$$

$$\lambda_G = \frac{L_G}{L_{rand}} \quad \textbf{(5.4)}$$

$$S_G = \frac{\gamma_G}{\lambda_G} \quad \textbf{(5.5)}$$

Here, L_G and C_G are the path length and clustering coefficient of the network under consideration and L_{rand} and C_{rand} are path length and clustering coefficient of a random network respectively. A given network is said to be a small world if $S_G > 1$.

5.4.5 Betweenness centrality

This metric offers a measure of a node's centrality in a network, i.e., a measure of a node's relative importance in the network. This allows us on average to quantify how well a given node is connected to all other nodes. Higher betweenness centrality is an important property of a "hub" node. For example, in a hypothetical network analysis of the entire population of the U.K., the Queen of U.K. (densely connected node), will receive a higher betweenness centrality score than the author of this thesis (sparsely connected node), making Her Majesty a major "hub" in the network. These hub nodes are commonly seen in computer networks, airline networks, and even in brain networks. It has also been shown that this "hubness" is affected in brain networks due to various neurological disease processes (Crossley et al., 2014).

Given an unweighted network and two nodes *i* and *j*, the number of unique shortest-paths between *i* and *j* can be defined σ_{ij}. Further, $\sigma_i(k)$ as the number of unique shortest-paths between *i* and *j* via node *k*. Betweenness centrality (CB_B) is –

$$CB_G = \sum_{i \neq k \neq j} \frac{\sigma_{ij}(k)}{\sigma_{ij}} \quad \textbf{(5.6)}$$

5.5 Towards an integrative approach

One of the advantages of network theory is the fact that it is modality invariant, i.e., the same network concepts can be applied to a wide range of data obtained from different modalities. However, networks obtained from different imaging modalities or different frequency bands in the same subjects are usually treated in isolation using a single-layer network approach. Yet, the field is increasingly acknowledging and elucidating how different types of networks are interrelated in a non-trivial way (Pereda et al., 2016). For instance, relationships between anatomical and functional networks are now established and often studied using computational models (Hlinka & Coombes, 2012). Moreover, recent studies suggest that functional networks are shaped by both monosynaptic and polysynaptic walks in the underlying structural network (Mehta-Pandejee et al., 2017; Meier et al., 2016a; Robinson, 2012). Likewise, covariance in cortical myeloarchitecture and fMRI connectivity matrices can be explained by a nonlinear combination of MEG functional connectivity matrices (Hunt et al., 2016; Tewarie et al., 2016). Importantly, for MEG and EEG, there is no reason why different frequency-specific networks would operate independently from one another (Tewarie et al., 2016). Despite its potential, the application of network theory to neuroimaging comes with several challenges, including:

1) How do we integrate information from networks across different neuroimaging modalities from the same subject or group?

2) How do we compare networks between groups and experimental conditions in an unbiased way?

5.6 Primer on multilayer networks

A generic framework that enables integration of information from different networks is the multilayer network approach. A multilayer network can be considered as a 'network of networks', which consists of individual network layers that are interconnected (Boccaletti et al., 2014; Van Mieghem, 2016). Thus, a given node in the multilayer network can be involved in different types of interactions. Multilayer networks can show non-trivial properties that are not merely the result of the sum of its layers (Kivelä et al., 2014; Nicosia et al., 2013; Sahneh et al., 2015). This approach has been applied effectively to several networks, such as social networks, transportation networks, and synthetic networks, demonstrating that empirical systems can be better understood when the influence of interacting networks are considered (De Domenico et al., 2013; Granell, Gómez, & Arenas, 2013; Hernández et al., 2014). Multilayer network approaches have recently been introduced to the field of neuroscience (Brookes et al., 2016; Buldú et al., 2017; Crofts, Forrester, & O'Dea, 2016; De Domenico et al., 2016; Tewarie et al., 2016; Yu et al., 2017), where different layers can correspond to different frequency-band specific networks or networks from different modalities. Lately, motif analysis of a multilayer network – where individual layers were made up of DTI and fMRI networks – was reported by (Battiston et al., 2017). Using the multilayer framework, a MEG study extracted meaningful connectivity differences between patients with schizophrenia and healthy controls (Brookes et al., 2016). Another study demonstrated a non-trivial relationship between frequency-band specific MEG networks for intermediate regimes of coupling between layers (Tewarie et al., 2016b). Furthermore, a multilayer network approach has also been applied successfully to the connectome of the *C. elegans*, where gap junctions and neuromodulator layers were grouped into different layers (Bentley et al., 2016; Nicosia and Latora, 2015; De Domenico et al., 2015a). This chapter is organised in the following way. It starts with a theoretical section on the basic mathematical concepts and metrics for multilayer networks,

followed by a short description of generative models for multilayer networks. These generative models allow us to evaluate correction schemes for given ground truth.

5.7 Quantifying multilayer networks: Multilayer graph metrics

A multilayer network is a generic name for a complex network structure consisting of multiple networks. Nodes exist in a set of layers that correspond to different important features of the system under consideration, and the links encompass connections between all possible combinations of nodes and layers. Specific widely-used special cases include multi-weighted graphs, multilevel or multi-scale networks, multiplex networks, multi-relational networks or hyper-networks (Boccaletti et al., 2014). These different types of networks all fall under the multilayer network framework and can be obtained after applying specific constraints (Boccaletti et al., 2014). Here it is worth noting that the multilayer network approach does not assume that the different layers are necessarily integrated. The multilayer framework leaves space to quantify the balance between distinctness and commonality among layers. There are several review papers for mathematically oriented readers on multilayer networks; please see (Boccaletti et al., 2014; De Domenico et al., 2013; Garas, 2016; Kivelä et al., 2014; Wang et al., 2013). For a recent review of multilayer networks applied to neuroimaging datasets see (De Domenico 2017). Here, the focus is on the aspects of multilayer networks that can be readily translated into neuroimaging (**Figure 6-1**).

A convenient representation of a multilayer network is its corresponding block-adjacency matrix (Gomez et al., 2013; De Domenico et al., 2013; Van Mieghem, 2016). An f-layered multilayer network written in terms of a block-adjacency matrix reads (Sahneh et al., 2015)

$$A = \begin{bmatrix} A_1 & H_{12} & \dots & H_{1f} \\ H_{21} & A_2 & & \vdots \\ \vdots & & \ddots & \\ H_{f1} & \dots & & A_f \end{bmatrix} \quad \textbf{(5.7)}$$

where A_α corresponds to a symmetric, square adjacency matrix of a layer α, $1 \leq \alpha \leq f$, and H_{kl} to the coupling matrix between the layers *k* and *l*, where $1 \leq k, l \leq f$. A_α has the same dimensions for all layers (n x n). This means that every layer has the same number of nodes or brain regions. The between layer coupling matrix H_{kl} can take any form, e.g., fully connected or a diagonal matrix (e.g., $H_{kl} = cI$, where *c* is a constant and *I* the identity matrix). Given the focus of recent theoretical studies, we concentrate on the following case where coupling matrices are special diagonal matrices ($H_{kl} = cI$), i.e., only introducing links between the same node (brain region) over all layers. In other words, the cross-frequency coupling between distant areas was ignored but note that the subsequent metrics can also be applied to the case of fully connected interlayer coupling (see **chapter 7** for a discussion on the choice of c).

The available topological metrics can be divided into –

1) Distance class metrics

   Distance class metrics are metrics where the geodesic distance or hops play a crucial role, where a hop refers to a link along a path.

2) Connection class metrics

   Connection class metrics refer to cohesive subgroups of nodes or the connectedness of a single node in the network.

3) Spectral class metrics

   Spectral class metrics correspond to properties related to the eigenvalues of the network of interest (Van Mieghem, 2011).

4) Between layer dependency metrics (Hernandez & Van Mieghem, 2011).

   Between layer, dependency metrics correspond to metrics that quantify relationships between layers.

5.7.1 Distance class metrics

Similar to single-layer networks, path length, *S*, and global efficiency, *G*, are measures of integration in the network and can be similarly defined as (Boccaletti et al., 2014)

$$S = \frac{1}{t(t-1)} \sum_{i,j,i \neq j} s_{ij} \quad \textbf{(5.8)}$$

$$G = \frac{1}{t(t-1)} \sum_{i,j,i \neq j} \frac{1}{s_{ij}} \quad \textbf{(5.9)}$$

where the distances s_{ij} refer to the number of hops (links) that you must traverse to travel from one node *i* to another node *j* along the shortest path between them, and where $t = nf$ (*f* layers). Distances can be obtained using Dijkstra's algorithm (Dijkstra, 1959). The global efficiency *G* can also be evaluated for a subnetwork consisting of only the neighbours of node *i*. This results in the metric local efficiency for every node, which is usually averaged across nodes in the neuroscience literature, yielding a single value per network (Rubinov & Sporns, 2010).

5.7.2 Connection class metrics

Several metrics exist in this class, such as metrics that quantify the "importance" or "hubness" in a network and other metrics that quantify clustering and community structure. A basic measure for "importance" for a given node *i* in multilayer networks is the multilayer degree d_i. This metric was introduced in its general form by De Domenico et al. (2013), and for the special case of the multiplex network by Battiston, Nicosia, and Latora (2014). A node labelling was assumed such that node *i* belongs to the *l*-th block row in *A* (Van Mieghem, 2016)

$$d_i = \sum_{l=1}^{f}(A_l u)_i + \sum_{b=1,b\neq l}^{f}\sum_{k=1;k\neq l}^{f}(H_{bk}u)_i \ldots$$
$$= \sum_{l=1}^{f} {}_l d_i + \sum_{b=1,b\neq l}^{f}\sum_{k=1;k\neq l}^{f}(H_{bk}u)_i\,, \qquad \textbf{(5.10)}$$

where ${}_l d_i$ is the degree of node *i* in the multilayer network layer *l*, $(H_{bk}u)_i$ are the inter-layer links from node *i* towards nodes at layer *k*, and *u* is the all-one vector (*f* = layers). This multilayer degree metric is the extension of the degree from single-layer networks. Extensions for eigenvector centrality to a multilayer framework also exist (Solá et al., 2013; Solé-Ribalta et al., 2014), as well as other more sophisticated measures, such as versatility of nodes and multilayer PageRank (De Domenico et al., 2013). Multilayer PageRank is a metric based on biased random walks in a multilayer network. A very recent metric related to multilayer PageRank is a functional multilayer PageRank (Iacovacci et al., 2016).

This metric uses the concept of a multilink $\vec{m}_{ij} = \left(a_{ij}{}^1, a_{ij}{}^2, \ldots, a_{ij}{}^f\right)$ and $\vec{m} = (m^1, m^2, \ldots, m^f)$, where $a_{ij}{}^l$ refers to a connection between node *i* and *j* in layer *l*. The functional multilayer PageRank X_i depends on a tensor ***z*** with elements $z^{\vec{m}}$, and captures the probability $\tilde{\alpha}$ with which a random walker in the multilayer network jumps from one node *i* to a neighbour *j* (first term in **Equation 5.11**) or to any other node in the multilayer network (second term in **Equation 5.11**)

$$X_i(\boldsymbol{z}) = \tilde{\alpha}\sum_{j=1}^{n} B_{ij}^{\vec{m}^{ij}}\, z^{\vec{m}^{ij}}\frac{1}{\kappa_j}X_j + \beta v_i. \qquad \textbf{(5.11)}$$

The first term contains the matrix B, which is called the multi-adjacency matrix

$$B_{ij}^{\vec{m}} = \prod_l^f \left[m_l a_{ij}^l + (1-m_l)\left(1-a_{ij}^l\right)\right], \qquad \textbf{(5.12)}$$

and reflects the neighbours of a node that are connected through a multilink. The probability that a random walker hops to a neighbour *i* is normalised by the following expression

$$\kappa_j = \sum_{j=1}^{n} B_{ij}^{\overrightarrow{m}^{ij}} z^{\overrightarrow{m}^{ij}} + \delta_{0,\sum_{j=1}^{N} B_{ij}^{\overrightarrow{m}^{ij}} z^{\overrightarrow{m}^{ij}}}, \quad \textbf{(5.13)}$$

where $\delta_{b,c}$ corresponds to the Kronecker delta function. The product βv_i in **Equation 5.11** describes a random jump to any other connected node in the network

$$\beta = \frac{1}{n}\sum_{j=1}^{n}\left[(1-\tilde{\alpha})\left(1-\delta_{0,\sum_{j=1}^{n} B_{ij}^{\overrightarrow{m}^{ij}} z^{\overrightarrow{m}^{ij}}}\right) + \delta_{0,\sum_{j=1}^{n} B_{ij}^{\overrightarrow{m}^{ij}} z^{\overrightarrow{m}^{ij}}}\right] X_j \quad \textbf{(5.14)}$$

$$v_i = \theta\left(\sum_{j=1}^{n} B_{ij}^{\overrightarrow{m}^{ij}} z^{\overrightarrow{m}^{ij}} + \sum_{j=1}^{n} B_{ji}^{\overrightarrow{m}^{ji}} z^{\overrightarrow{m}^{ij}}\right). \quad \textbf{(5.15)}$$

Here, θ corresponds to the Heaviside function. By tuning z, different versions of $X_i(\boldsymbol{z})$ can be obtained, however, the global ranking of the nodes, i.e., $X_i^* = \max X_i\,(\boldsymbol{z})$ was of interest. This maximum value can easily be found by expressing z in spherical coordinates (Iacovacci et al., 2016). The input to **Equation 5.11** can also be in the form of weighted adjacency matrices (Iacovacci et al., 2016).

The clustering coefficient on single-layer networks has been generalised to multilayer networks as another instance of connection class metrics. This metric captures the amount of segregation in the network in terms of triangles. In the multilayer version of the clustering coefficient C_i, a triangle can be formed by links in different layers (Battiston et al., 2014)

$$C_i = \frac{\sum_l \sum_{k \neq l} \sum_{j \neq i, j \neq i} a_{ij}^l a_{ij}^k a_{ji}^l}{(f-1) \sum_l {}_l d_i \left({}_l d_i - 1 \right)}, \quad \textbf{(5.16)}$$

where a_{ij}^l refers to a connection between node *i* and *j* in layer l. It must be noted that the multilayer clustering coefficient given by **equation 5.16** can be extended to analyse structural–functional network relationships. In particular, their divergence under certain dynamical system conditions, in directed networks of relevance to neural systems (Crofts et al., 2016). Such ideas can be extended to weighted temporal (e.g., frequency band) networks.

As a further instance of connection class metrics, community detection algorithms have been widely applied to single-layer brain networks. In fMRI resting state networks, community structure, has been shown to reveal similar clusters as resting-state networks obtained from the independent component analysis (Crossley et al., 2013; Meunier et al., 2009). Details on multilayer community structure can be found in Bassett et al. (2013) and Mucha et al. (2010). Communities g_i are usually obtained after optimisation of a quality function, e.g., modularity (Newman, 2006), that quantifies within-community connections relative to connections between communities. The multilayer variant of modularity is expressed as (Bassett et al., 2013)

$$Q = \frac{1}{2u_{tot}} \sum_{ijlk} \left[\left(A_{l,ij} - \gamma_l \frac{{}_l d_i \; {}_l d_j}{2 \sum_i {}_l d_i} \delta_{lk} \right) + \delta_{ij} H_{lk,j} \right] \delta_{g_{il}, g_{jk}} \quad \textbf{(5.17)}$$

where u_{tot} corresponds to the total link weight in the network, γ_l to the resolution parameter, g_{il} stands for the community assignment of node *i* in layer l. Another way to extract communities is motif partitioning explained in Evans (2004), which has been applied to directed MEG networks in Meier et al. (2016b); Märtens et al. (2017).

5.7.3 Spectral class metrics

Spectral metrics are either based on the (eigen) spectrum of the block-adjacency matrix *A* or on the Laplacian *Q* of the multilayer network, obeying $Qx = \mu x$, where *x* and μ are eigenvectors and eigenvalues (Van Mieghem, 2011), respectively, of *Q*, which is defined as

$$Q = \begin{bmatrix} \Delta_1 - A_1 & 0 & \cdots & 0 \\ 0 & \Delta_2 - A_2 & & \vdots \\ \vdots & & \ddots & 0 \\ 0 & \cdots & & \Delta_f - A_f \end{bmatrix} + \begin{bmatrix} \sum_l H_{1l} & -H_{12} & \cdots & -H_{1f} \\ -H_{21} & \sum_l H_{2l} & & \vdots \\ \vdots & & \ddots & \\ -H_{f1} & \cdots & & \sum_l H_{fl} \end{bmatrix}$$

with **(5.18)**

$$\Delta_l = \mathrm{diag}\left({}_l d_1,\ {}_l d_2, \ldots,\ {}_l d_n \right), \quad \textbf{(5.19)}$$

where ${}_l d_i$ $(1 \le i \le n)$ is the degree of node *i* in layer *l* (remember that every layer has n nodes). Let $\mu_1 \ge \mu_2 \ge \cdots \ge \mu_t$ be the ordered set of eigenvalues of Q, where $t = nf$. The second smallest Laplacian eigenvalue μ_{t-1} is called the algebraic connectivity. This metric is related to the time to synchronize phase oscillators in a network and also to the robustness of a network: a higher algebraic connectivity means a higher inter-twined subgraph structure, which makes it harder to fragment the graph (Martín-Hernández et al., 2014). A relatively novel way to capture topological information from the network is to analyse the pseudo-inverse $Q^\dagger$ of the Laplacian (Ellens et al., 2011; Van Mieghem et al., 2017). The effective graph resistance $\tilde{R}_G$ and the zeta vector can be obtained from this pseudo-inverse

$$\tilde{R}_G = t\ \mathrm{trace}(Q^\dagger) \quad \textbf{(5.20)}$$

$$\zeta = \left(Q_{11}^\dagger, Q_{22}^\dagger, \ldots, Q_{tt}^\dagger\right) \quad \textbf{(5.21)}$$

The effective graph resistance captures the overall transport ability: the lower $\tilde{R}_G$, the lower the resistance for flow in the network (Van Mieghem et al., 2017). The zeta vector captures the information of nodal spreading within the network. The effective graph resistance $\tilde{R}_G$ and the zeta vector are defined in both weighted and unweighted graphs.

5.7.4 Between layer dependency

In addition to well-known metrics for single-layer networks (**introduced in 5.4**), multilayer networks can also be characterised by their between-layer relationships, examples are:

1) Entropy of multilayer degree

   The entropy of multilayer degree follows the definition of Shannon entropy with the probability replaced by ${}_{l}d_i/d_i$.

2) Multilayer participation coefficient

   Multilayer participation coefficient is related to the entropy and quantifies whether links of a given node *i* are uniformly distributed among layers (Battiston et al., 2014)

$$PC_i = \frac{f}{f-1}\left[1 - \sum_{l=1}^{f}\left(\frac{{}_{l}d_i}{d_i}\right)^2\right]. \qquad \textbf{(5.22)}$$

3) Conditional probability of finding a link in layer α given a link in layer α'

4) Degree correlations (Battiston et al., 2014; Garas, 2016).

   Between layer degree correlations (DC) can be quantified by computing a Pearson correlation between the degree sequences of different layers (Battiston et al., 2014; Wang et al., 2014).

Between layer dependency metrics allow one to capture whether individual layers act independently, in coherence with each other or in a regime between these two extremes, as recently demonstrated in (Tewarie et al., 2016).

5.8 Generative models for multilayer networks

The simulated networks (i.e., known ground truth) will subsequently be used to assess the efficacy of various graph metrics and measures developed to correct biases introduced by differences in average connectivity.

5.8.1 Non-linear preferential attachment for multilayer networks

The first model that was used is a nonlinear preferential attachment model (Nicosia et al., 2014). Here, the initial conditions are a small connected multilayer network consisting of n_0 nodes and with f layers. Then, for every time step during the construction of the network, a node i is added to the multilayer network and connected to another node j with probability $\Pr_{i\to j}$ based on the multilayer degrees

$$\Pr_{i\to j} \propto f\left({}_1d_j,\ {}_2d_j, \dots,\ {}_fd_j\right). \quad \textbf{(5.23)}$$

If we consider the case of a two-layered multilayer network (duplex, f=2) we can choose the function f as

$$f\left({}_1d_j,\ {}_2d_j\right) = \left({}_1d_j\right)^{\alpha}\left({}_2d_j\right)^{\beta}. \quad \textbf{(5.24)}$$

By tuning α and β, different network configurations can be obtained, for example, by tuning α or β from negative to positive, to construct layers with different correlations between their degrees (i.e., the correlation between the degree sequence layer one vs. degree sequence layer two). For the results section, a two-layer multilayer network was created consisting of 200 nodes and β was tuned to alter the interlayer dependency.

5.8.2 Synthetic multilayer community networks

The second generative model that was used created multilayer communities with the tuneable between-layer dependency of these communities; details of the algorithm can be found in Bazzi et al. (2016). The algorithm consists of two sequential steps. First, a multilayer partition is constructed. Partitions in each layer are initialised independently and updated iteratively according to a user-defined interlayer dependency tensor. Then, a random multilayer network is generated using the previously defined multilayer partitioning. This is done using a generalisation of stochastic block models to multilayer networks (Karrer & Newman, 2011). A link is added in the multilayer network based on a probability that is proportional to the product of the partition, the expected number of links between communities (user-defined), and the expected number of links within communities. In addition, the multilayer networks can be constructed with a fraction of random links. In the simulations presented in the results section the similarity of communities in the different layers is tuned by altering the interlayer dependency tensor.

CHAPTER 6

6 Comparing multilayer brain networks between groups

Précis

There is an increasing awareness of the advantages of multi-modal neuroimaging. Networks obtained from different modalities are usually treated in isolation, which is however contradictory to accumulating evidence that these networks show non-trivial interdependencies. Following on from the theory introduced in the previous chapter, this chapter discusses how a multilayer network framework allows for the integration of multiple networks into a single network description, and how graph metrics can be applied to quantify multilayer network organisation for group comparison. The chapter discusses how well-known biases for single-layer networks, such as the effects of group differences in link density and/or average connectivity, influence multilayer networks. Furthermore, four schemes were compared that aim to correct such biases: the minimum spanning tree (MST), effective graph resistance cost minimisation, efficiency cost optimisation (ECO) and a normalisation scheme based on singular value decomposition (SVD). It is demonstrated how these schemes can be applied to the layers independently or to the multilayer network as a whole. The chapter discusses how biases in group comparisons may differ between brain imaging centres and studies and could consequently lead to irreproducible results in a similar manner as it is possible for single-layer networks. Finally, some recommendations are made on using correction schemes prior to multilayer network analysis for group comparisons. These recommended schemes are then used in a group comparison study in the following **chapter 7**.

6.1 Introduction

Despite the obvious promise of multilayer approaches, a key issue in the application of network theory is comparison between groups or conditions. Group comparison at the level of single-layer networks can be challenging and biased by, for example, link density (van den Heuvel et al., 2017; van Wijk, Stam, & Daffertshofer, 2010). In other words, network measures depend on non-organisational properties of the network such as link density and average connectivity. As a result, it proves to be challenging to differentiate between alterations in the underlying ground truth that are due to an experimental manipulation or a disease process from those that are due to experimental choices. This can potentially inflate false positives or false negatives when comparing networks between groups, which are referred to here as the biases in group comparisons. Similar to biases in single-layer networks, there are no reasons why multilayer networks would be exempted from these. Given the recent studies on multilayer networks in different diseases (Brookes et al., 2016; De Domenico et al., 2016; Guillon et al., 2017; Yu et al., 2017), it is now crucial to elucidate how to compare multilayer networks between groups. For single-layer networks, several sampling methods or schemes have been proposed to correct for the biases in estimates of topology that are due to link density or average functional connectivity for unweighted and weighted networks respectively (van Wijk et al., 2010). Examples of schemes that result in an unweighted subnetwork are multi-threshold permutation correction (Drakesmith et al., 2015), the minimally connected component (MCC) (Jalili, 2016), the balance between network efficiency and costs (ECO) (Fallani et al., 2017), a clustering optimization approach (Smith et al., 2015), the minimum spanning tree (MST) (Stam et al., 2014; Tewarie et al., 2015) and the union of shortest-path trees (USPT) (Meier, Tewarie, & Van Mieghem, 2015). The MCC is based on a thresholding scheme, where a threshold is chosen just above the level where the network gets disconnected into components. For ECO, a threshold is chosen that maximises the ratio between network efficiency and link density,

whereas the MST corresponds to the tree (a loop-less subnetwork) with the minimal sum of all weights that spans the original network. The USPT corresponds to the union of shortest-path trees rooted at each node in the graph. While these approaches to extract unweighted networks have demonstrated their value for single-layer networks, it remains unclear whether these approaches generalise to multilayer networks. Approaches for weighted networks (Wang et al., 2010), such as normalising by the mean or range of connectivity values have so far been less promising (van Wijk et al., 2010).

The current chapter is organised as follows –

1) It is demonstrated that multilayer network metrics are biased in a similar fashion as single-layer metrics

2) Existing and two new approaches as solutions to correct for biases in link density and average connectivity are evaluated

3) The sensitivity of the solutions in revealing true changes in network topology is assessed

4) Synthetic networks based on generative models (e.g., nonlinear preferential attachment model and a generative model for multilayer community networks) are used as ground truth. These approaches are also applied to empirical MEG and fMRI data since correction schemes are only useful if changes in the underlying topology can still be detected after the correction.

5) Lastly, the sensitivity of multilayer network metrics in detecting group differences is assessed

6.2 Methods

6.2.1 Empirical MEG and fMRI networks

To derive empirical networks, a previously published MEG/fMRI dataset is used here (Tewarie et al., 2016a). A total of 15 participants (mean age 27.7 ± 6.5, 60% female) were used for analysis in this study. The study was approved by the University of Nottingham Medical School Ethics Committee, and all subjects gave written informed consent prior to participation.

MEG data were acquired using a 275 channel CTF MEG system (MISL, Coquitlam, Canada), at a sampling rate of 600 Hz and using a 150 Hz low pass anti-aliasing filter. Data were recorded during a task-free, eyes-open condition for 10 min with the subject in a supine position. Subjects were asked to fixate on a red cross throughout. The surface of the head was digitised using a 3D digitiser (Polhemus Inc., Vermont). Co-registration was achieved using surface matching of the digitised head shape to an equivalent head shape extracted from an anatomical magnetic resonance (MR) image. MEG data were inspected for artefacts and trials deemed to contain excessive interference were removed. Lead fields were based on equivalent current dipole models (grid spacing of 4mm) and a multiple local sphere head model (Huang et al., 1999). Lead fields, the parcellated individual's cortex (automated anatomical atlas (AAL); (Gong et al., 2009; Tzourio-Mazoyer et al., 2002), and sensor level MEG data were fed into a scalar beamforming approach (Hillebrand et al., 2012). Data covariance was computed within a 1-150 Hz frequency window, and regularisation was applied to the data covariance matrix using the Tikhonov method with a regularisation parameter of 5%. Dipole orientation was determined using a non-linear search for optimal signal-to-noise-ratio. Beamformer time courses were sign-flipped where necessary to account for the arbitrary polarity introduced by the beamformer source orientation estimation. Beamformer time courses within a parcellated region were averaged using a Gaussian weighting function to obtain a representative time course for every region. This complete process resulted in 78

electrophysiological time courses, each representative of a separate cortical AAL region. Time courses were frequency filtered into five frequency bands: delta (1–4 Hz), theta (4–8 Hz), alpha (8–13 Hz), beta (13–30 Hz), gamma (30–48 Hz). This was followed by a multivariate orthogonalisation to correct for signal leakage (Colclough et al., 2015). Finally, a functional connectivity matrix was reconstructed by computing amplitude envelope correlations between leakage-corrected frequency-filtered time courses (Brookes et al., 2011).

MRI data were collected using a 7 T-MRI system (Philips Achieva) with a volume transmit and 32 channel receive head coil. The anatomical MR image (used for MEG source reconstruction as well as fMRI processing) was acquired using an MPRAGE sequence (1 mm isotropic resolution, TE = 3 ms, TR = 7 ms, flip angle = 8°). Bias fields were corrected using SPM8 and brain extraction for the MPRAGE was achieved using the Brain Extraction Tool (BET v2.1, FSL (FMRIB's Software Library, http://www.fmrib.ox.ac.uk/fsl) (Smith et al., 2004). Resting-state fMRI data were acquired using a gradient-echo echo-planar imaging sequence (TR = 2 s, TE = 25 ms, flip angle = 75°, voxel dimensions = 2 × 2 × 2 mm^3, 150 volume acquisitions). Participants were asked to keep their eyes open during the scan and to fixate on a cross presented on a back-projection screen and viewed via a mirror. Data were motion-corrected using SPM8 (Ashburner, Andersson, & Friston, 1999). Subject-specific masks of grey matter, white matter, and cerebrospinal fluid (CSF) were obtained via automatic segmentation of the MPRAGE data (FAST v4.1 FSL (Smith, 2002)). The AAL atlas was used to parcellate the cortex into the same 78 regions of interest (ROIs) as used for the MEG data. The fMRI data were registered to the corresponding MPRAGE image, which was in turn registered to the MNI-152 template brain (FLIRT v5.5, FSL). Inverse transformations were calculated and used to register a grey matter mask and the AAL ROIs to the functional space for each subject. To maintain the consistency between the fMRI and MEG pipeline, a weighted average fMRI signal was computed to obtain a single signal for every ROI. Average cerebrospinal fluid signal, average white matter signal, motion and 2nd order

polynomials (i.e., low-frequency trends) were regressed out from each regional BOLD time course using a general linear model to remove non-neuronal signals. For each subject, pairwise Pearson correlation coefficients (absolute values) were computed between all possible 78 fMRI AAL signal pairs to obtain a connectivity matrix.

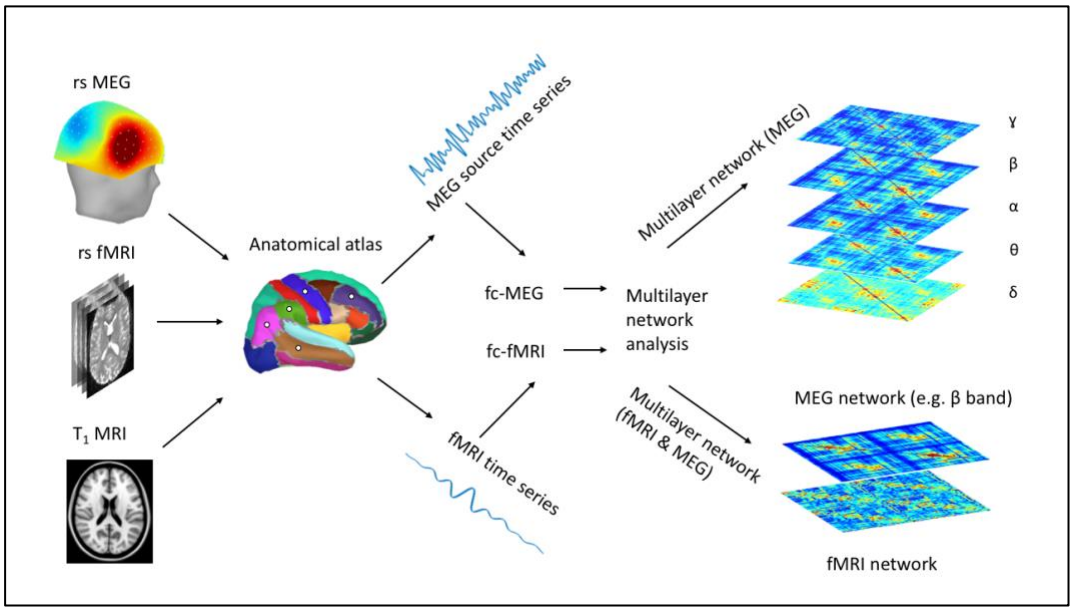


Figure 6-1 *A schematic of the analysis pipeline including the construction of MEG specific multilayer network and a multimodal (fMRI-MEG) multilayer network. Note that a special case of multilayer networks is used here: multilayer networks with one-to-one between layer coupling. rs: Resting-state, fc: Functional connectivity*

6.3 Schemes for the correction of network biases

A special case of multilayer networks is treated here, for which the interlayer coupling matrix $H_{KM} = cI$ (i.e., no cross-frequency coupling between different nodes, see **equation 5.7**). Here, c is a constant and I the identity matrix. Figure **6-1)** shows two possible ways to construct a multilayer network. This network construction is in line with previously published studies (Guillon et al., 2017; Yu et al., 2017). One can either stack different frequency-band specific MEG networks as layers into a multilayer network or one can stack two networks from two different modalities, e.g., beta band MEG network (most similar to fMRI networks, Brookes et al., 2011; Tewarie et al., 2016a), and the fMRI network, into a multilayer network. There are of course other possible ways to construct multilayer networks (e.g., all MEG networks together with a structural network and fMRI network) that will be addressed in the discussion, but for now, the analysis was restricted to the former two cases.

When treating a multilayer network based on different MEG connectivity matrices obtained with the same connectivity metric (i.e., pan spectral network), the weights contain meaningful information. It is therefore argued that a correction scheme should take the information regarding weight differences between the frequency bands into account. In the context of multilayer networks, this is important with respect to layer dominance (Sahneh & Caterina, 2014; Wang et al., 2014), i.e., one layer could be a stronger driver of multilayer network characteristics than other layers. Therefore, it was proposed that a correction scheme should be applied to the block-adjacency matrix (*A*), rather than a correction scheme that is applied to the adjacency matrices of every layer (A_α) separately (see **equation 5.7**). In this chapter both the cases of normalisation are discussed (i.e., normalisation scheme applied to individual layers and normalisation scheme applied to the network as a whole).

However, when treating a multilayer network based on different modalities, or based on different metrics using the same modality, the range of the link weights can be

very different, and thus the differences in link weights for the different layers are artificial. Therefore, in such cases, it was proposed that a correction scheme should be applied to the individual layers ($A\alpha$) separately.

The choice of SVD normalisation is crucial when layers in the multilayer network are made from different modalities. The normalisation of a block-adjacency matrix can be performed in two ways – a) normalisation of the network as a whole or b) individual layer normalisation. The choice of normalisation is governed by how the multilayer network is constructed, i.e., if a block-adjacency matrix contains exclusively pan spectral (M/EEG) connectivity data (i.e., individual layers of the pan-spectral network correspond to individual M/EEG frequency bands) then the normalisation is applied to the multilayer network as a whole. Whereas, if a block-adjacency matrix contains layer information derived from different modalities (e.g., MEG and fMRI or MEG and DTI) then individual layer normalisation is performed. The choice of normalisation for the former (M/EEG frequency bands) is not as crucial as the latter (multimodal data). Both these approaches are tested below (see 6.4.2 and 6.4.3).

Four network correction schemes are employed here: MST, ECO and two new methods: effective graph resistance cost minimisation and network normalisation based on SVD. The first three approaches usually result in unweighted networks and correct for biases due to an average degree or link density and aim to only include the backbone of the network. The SVD approach corrects for differences in average connectivity between groups and results in a weighted network (the scaled version of the original network).

6.3.1 MST

The minimum spanning tree is a loop-less subnetwork that spans the original network using the minimum possible sum of link weights (Kruskal, 1956). The number of links in a tree is always equal to n-1 (or n*f*-1 for multilayer networks), and therefore no biases due to (differences in) link densities exist. After extracting the MST, link

weights in this subnetwork are set to one. Furthermore, as long as the weight ordering is maintained, the MST is unaffected by manipulations of the original network. Strictly speaking, the MST gives a reduced topology rather than a correction, such as ECO. However, to remain consistent across all approaches, MST is also treated as a correction scheme here.

6.3.2 ECO

Efficiency cost optimisation is based on optimising the function $J = (G + Y)/\rho$, where *G* and *Y* are the global and local efficiency of the network (see **equations 5.8, 5.9**) and ρ the link density (fraction of links). It has been demonstrated analytically that the maximum for this function for different types of network topologies obeys $\rho \approx 3/(n-1)$, where n is the number of nodes (De Vico Fallani et al., 2017). In the case of multilayer networks, this becomes $\rho \approx 3/(nf-1)$. Therefore, for all the subsequent analyses, results for this analytically obtained link density are shown.

6.3.3 Effective graph resistance cost minimisation

Since there is evidence that large-scale communication in the brain is not merely shaped by efficiency, as inferred by a function of the shortest-paths (Goñi et al., 2014; Meier et al., 2016), and because of the risk of disconnected networks, a different version of ECO was proposed. Instead of efficiency cost optimisation, effective graph resistance cost minimisation $F = \tilde{R}_G/\rho$ was proposed. Since there is no analytical expression to determine the optimum value for *F*, a numerical approach is followed to find the minimum (this entails computing *F* for a range of link densities to determine the threshold that minimises *F*). This scheme is based on **Equation 5.20** and thus the correction scheme is applied to the block-adjacency matrix rather than to the individual layers separately.

6.3.4 SVD normalisation

For any matrix (block-adjacency matrix A or adjacency matrix A_α) a singular value decomposition $A = U\Lambda V^T$ is applied, where U and V contain the left and right singular vectors and Λ the singular values of A. To correct for average connectivity/average link weight Λ can be rescaled by the largest singular value λ_1. The rescaled matrix would thus become $\tilde{A} = U\left(\frac{10}{\lambda_1}\Lambda\right)V^T$. The multiplication by 10 is used to ensure that the range of values in $\tilde{A}$ is not too small and varies between 0 and 1. If A is a symmetric and square matrix, then a singular value decomposition returns the eigenvalues and eigenvectors. However, an eigenvalue decomposition can result in complex eigenvalues if A is non-symmetric and square (directed network), and therefore a singular value decomposition can be used to exclude potentially complex eigenvectors and eigenvalues[2].

The reasons for normalising the symmetric and square block-adjacency matrix (as studied here) by its *largest* eigenvalue are as follows –

1) The largest eigenvalue λ_1 is called the spectral radius of the graph ($\lambda_1, \lambda_2, \lambda_3, \ldots, \lambda_n$ is the eigenspectrum). Recent work has shown that the epidemic threshold (critical threshold) of a network is given by the inverse of the spectral radius of the network's adjacency matrix (Kivelä et al., 2014; Van Mieghem, 2016). Moreover (Van Mieghem, 2016) has demonstrated that it is also the threshold of phase transition of virus spread and synchronisation of coupled oscillators in networks. Therefore, by normalising the adjacency matrix by its spectral radius, the critical threshold is equalised between groups and datasets. The inverse of the spectral radius is a measure of synchronisation threshold, it is related to shortest-path, overall connectedness and degree diversity of a graph (for review see (Stam & van

2 In general, the SVD is the eigenvalue decomposition of the Gram matrix, thus of A^TA (where A is an n x m matrix, and m can be different from n). In fact, for non-square matrices, the SVD was originally used (Golub & Van Loan, 1996)

Straaten, 2012)). This is relevant for group comparisons performed in **Chapter 7.**

2) The largest eigenvalue is an upper bound for the norm of the adjacency matrix (Van Mieghem, 2011). Therefore, normalisation based on the first eigenvalue is also normalisation by the norm of the adjacency matrix. Any combination of a set of values (i.e., sum over all eigenvalues or the sum over more than one of the highest eigenvalues) in the eigenspectrum does not have such a mathematical relationship with the norm of the matrix.
3) Lastly, the first eigenvalue also captures the main mode of variation of functional connectivity. Tewarie et al., (2016) demonstrated this by removing the first eigenvalue and calculating average correlation over all the layers of the multilayer network. This led to a sharp increase in global correlations, potentially indicating that the largest eigenvalue is likely responsible for frequency-specific information (see **Figure 4A** in Tewarie et al., 2016).

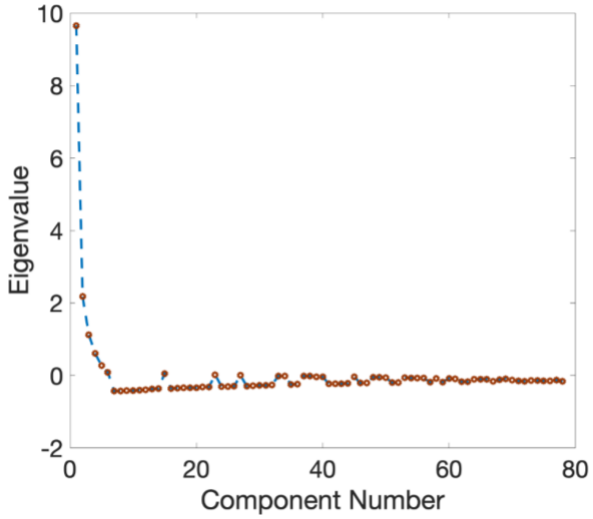


Figure 6-2 *The plot shown here is the eigenspectrum of a MEG multilayer network used in this chapter (see **6.4.1**, layer 1: alpha band, layer 2: beta band). We normalise the adjacency matrix by its largest eigenvalue also known as the spectral radius of the graph.*

6.4 Results

6.4.1 Uncorrected multilayer networks are affected by average link weight or link density

To show the biases that can be introduced when a correction scheme is not applied, it was first demonstrated how multilayer metrics vary as a function of link density (ρ see **section 6.3.2**) or average connectivity strength (<FC>: the sum of weighted degrees) of an empirically based multilayer network. This multilayer network has two layers, corresponding to the group averaged alpha and beta band MEG networks. We applied different proportional thresholds, tuned the average functional connectivity strength, and subsequently computed four multilayer network metrics: degree correlation between layers (DC), mean functional multilayer PageRank (X), mean multilayer participation coefficient (PC) and multilayer modularity (Q).

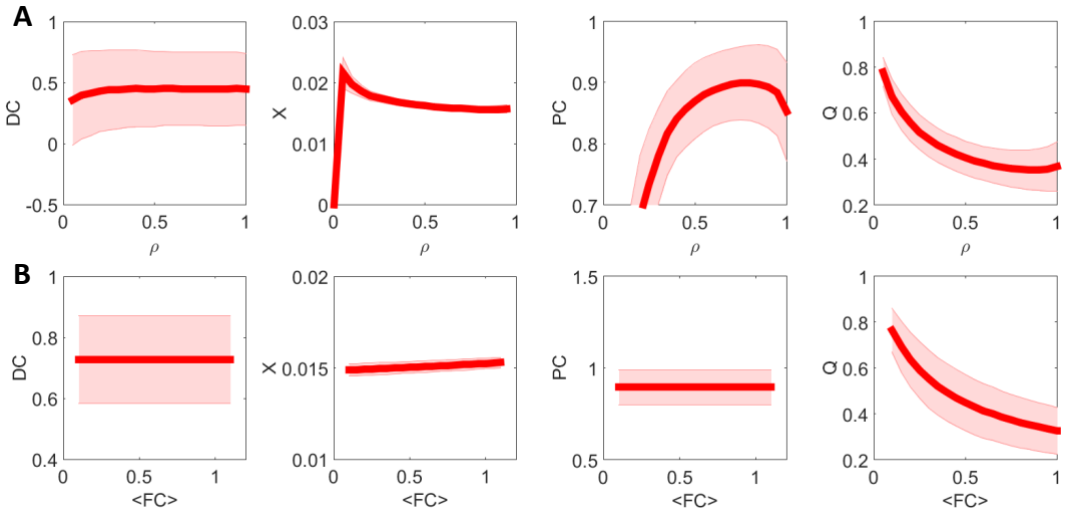


Figure 6-3 *Metrics are affected by changes in link density (A) and average connectivity (B). The plots show that tuning arbitrary link density (i.e., an arbitrary threshold), or the average connectivity, affects most of the metrics. However, this was not the case for DC and PC for changes in average connectivity. ρ = link density, DC: degree correlation, X: functional multilayer page rank, PC: participation coefficient, Q: multilayer modularity, <FC>: average functional connectivity. The solid line and shaded areas show the mean and standard deviation across subjects, respectively.*

Figure **6-3A)** shows the different multilayer network metrics as a function of link density. Different thresholds for link density (**Figure 6-3B**) (lower panel) can non-trivially influence network metrics. Thus, choosing an arbitrary threshold for groups with different densities can artificially induce significant group differences in terms of multilayer network metrics shows the different multilayer network metrics as a function of average connectivity. *Q* is affected since it is optimised in terms of the degrees, which scale with connectivity. Other metrics such as based on computing a correlation (DC) or ratios (PC) are naturally unaffected by differences in scale. However, to safely use all multilayer metrics on a weighted network, one would have to correct for average connectivity.

6.4.2 Applying correction schemes to multilayer networks as a whole

Four correction schemes are applied to the block-adjacency matrix of the multilayer network in the previous section: MST, ECO, effective graph resistance cost minimisation and SVD normalisation. The multilayer network has two layers *viz.*, alpha and beta band. First, MSTs are usually unaffected by a threshold, if a threshold applied to a network does not discard links that would be included in the MST, the MST computed on a thresholded network would be unaffected. However, this stability is not observed in the case for MSTs computed on a multilayer network (**Figure 6-4A**), where the MSTs computed for different link densities are not the same. The lack of uniqueness for the MST comes from the non-unique values of $H_{kl} = cI$. Furthermore, for most link densities, one of the individual layers can become disconnected (denoted by red dots in **Figure 6-4A**). (**Figure 6-4B)**, illustrate this, from layer one in this multilayer network, it can be inferred that not all nodes within a layer form a fully connected set in that layer, i.e., there are two connected components within the layer. Results for ECO are more stable compared to the MST. If the link density is above $\rho \approx 3/(nf-1)$, then the network with exactly this density is extracted. However, even after applying ECO, the resultant multilayer network can be disconnected either on the level of individual layers or the whole

multilayer network (denoted by green dots in **Figure 6-4A**). In **Figure 6-4D**, shows effective graph resistance cost minimisation as a function of link density. Recall that the lower $\tilde{R}_G$ the lower the resistance for flow in the network. There no clear minimum for $\tilde{R}_G$, but $\tilde{R}_G$ reaches a plateau at around $\rho = 0.3$. Results for the SVD normalisation are shown in **Figure 6-4C**. SVD normalisation leads to stable values for Q as a function of average functional connectivity (compare with **Figure 6-3B**, lower right corner panel). The other metrics do not vary as a function of average connectivity either.

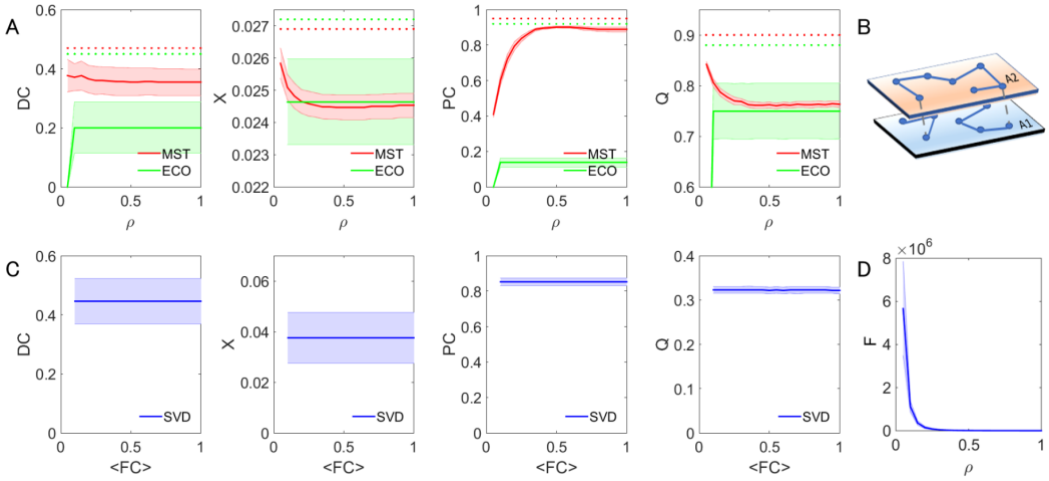


Figure 6-4 *The multilayer network made from participants' alpha and beta band networks. A) MST correction scheme on the whole multilayer network. This may result in a network that is connected but with disconnected individual layers, denoted by the multiple red dots and illustrated in (B). ECO correction scheme on the multilayer network (A). This can also lead to disconnected networks denoted by multiple green dots. C) SVD correction scheme on the whole multilayer network. D) Effective graph resistance cost minimisation. The solid line and shaded areas show the mean and standard deviation across subjects, respectively. ρ = density, <FC>: average functional connectivity, DC: degree correlation, X: functional multilayer PageRank, PC: participation coefficient, Q: multilayer modularity, F: effective graph resistance cost minimisation.*

6.4.3 Applying correction schemes to individual layers in multilayer networks

The case of a two-layered multilayer network was considered, consisting of layers obtained from a subject's beta band MEG network, and their fMRI network, i.e., from different modalities. Again, results are shown based on individual subjects for which the mean and standard deviation was illustrated (**Figure 6-5**). Instead of applying correction schemes to the block-adjacency matrix, the four correction schemes are applied to the individual layers. (**Figure 6-5A)** shows the MST (red) and the ECO based networks (green) for different link densities and the stability of multilayer network metrics after applying the correction schemes MST and ECO. Unlike for the correction to the whole block-adjacency matrix (**Figure 6-4A**), the MST does not depend on the non-unique values of H_{Kl}, and therefore the weights for calculating the MST are unique, which results in stable and unique MSTs. Note though that non-unique link weights within individual layers can lead to non-unique MSTs. The SVD normalisation again results in a correction for biases in average connectivity (**Figure 6-5B**). For effective graph resistance cost minimisation, a plateau is reached for layer 1 (beta band MEG) for $\rho = 0.6$ and $\rho = 0.25$ for layer 2 (fMRI network). Again, no local minimum was observed in this domain for ρ. Lastly, the choice of correction scheme might affect the ability to detect group differences (i.e., larger variability might hide genuine group differences). The sensitivity to detect changes in network topology is therefore assessed in the next paragraphs.

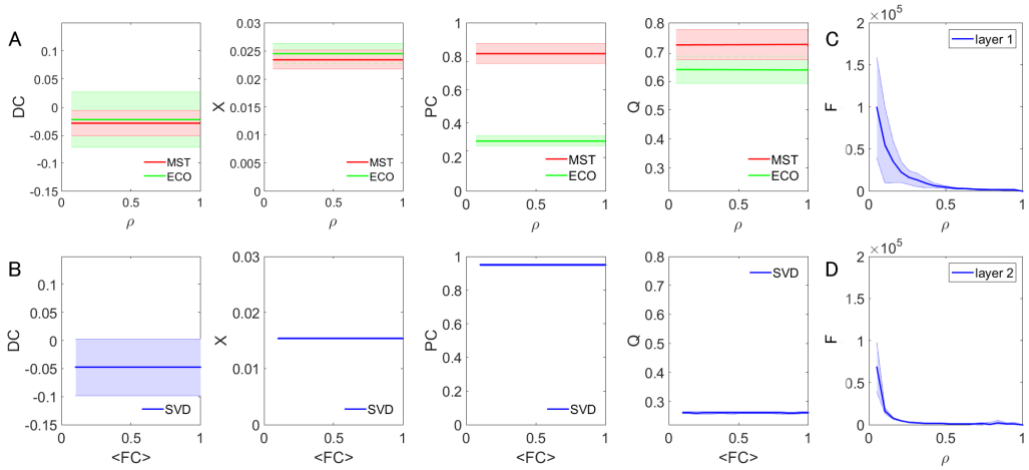


Figure 6-5 *The multilayer network made from participants' beta band MEG and fMRI networks. A) MST and ECO correction schemes applied to the individual layers. B) SVD correction scheme applied to individual layers. CD) Effective graph resistance cost minimisation in the two layers. The solid line and shaded areas show the mean and standard deviation across subjects, respectively. ρ = density, <FC>: functional connectivity, DC: degree correlation, X: functional multilayer page rank, PC: participation coefficient, Q: community structure, F: effective graph resistance cost minimisation.*

6.4.4 Nodal community assignment in multilayer networks after applying correction schemes

The SVD correction scheme applied to the whole multilayer network, and the SVD, MST and ECO applied to individual layers can adequately correct for differences in average connectivity or link density. However, the magnitude of Q, for instance, gets altered after applying correction schemes. It is therefore important to assess to what extent the underlying communities change after applying a correction scheme. In **Figure 6-6** the community assignment for every node was plotted on a brain plot for the original multilayer network (empirical alpha and beta band network) and the community assignment for a node after applying the correction schemes. A sensorimotor network (green) and a visual network (red) can be identified, which are dominant patterns in the beta and alpha band respectively. It can be observed that only SVD can correctly identify the original networks. Lastly, one should be cautious

with community assignment in a tree (MST) with conventional methods, i.e., there will never be more links within a module than between modules. An alternative is the hierarchical clustering method evaluated in (Yu et al., 2015). The latter was not applied in the current work to keep consistency for all correction schemes.

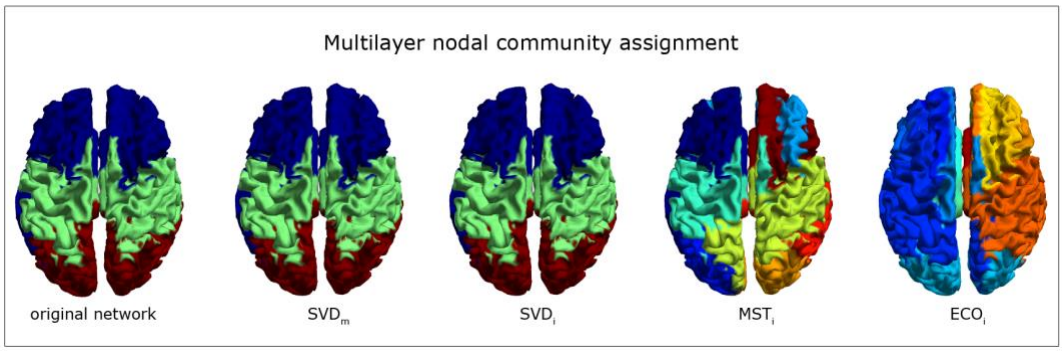


Figure 6-6 *Community assignment of multilayer networks (alpha and beta band) after applying correction schemes. Nodes that have the same colour belong to the same community (shown for the first layer here). On the outmost left, the original community assignment for every node is shown and further to the right the assignment after applying correction schemes is visualized. Only SVD applied to the whole multilayer (SVD_m) and on the individual layers (SVD_i) can correctly identify the communities. ECO and MST applied to the individual layers distort community assignments of nodes.*

6.4.5 Sensitivity to genuine alterations in multilayer network organisation – correction applied to multilayer networks as a whole

Given the ability of some of the schemes to correct for non-topological biases, the sensitivity of network metrics to changes in network topology after applying a correction to the block-adjacency matrix was tested. Sensitivity in this context is referred to as the ability of multilayer graph metrics to detect changes in the ground truth. The analysis is only performed for the SVD normalisation, since results from the previous paragraph showed that MSTs computed on the entire multilayer network resulted in non-unique MSTs, the ECO approach resulted in disconnected networks, and effective graph resistance cost minimisation did not yield a unique

global minimum that could serve as a plausible link density. First, the multilayer community model and the nonlinear preferential attachment model were used to construct two-layered synthetic multilayer networks with known ground truth (see section **5.8**). In each model, the between-layer dependencies were tuned, which influences the similarity in communities or degree sequences across the two layers, respectively. This was done by altering the interlayer dependency tensor for the multilayer community model or by tuning β for the nonlinear preferential attachment model. (**Figure 6-7A)** shows the behaviour of the modularity Q as a function of between layer dependency in the original multilayer network and in the SVD corrected version. By applying SVD normalisation, there is a reduction in sensitivity to the similarity in communities between layers and an overestimation of Q (Q from the corrected network is higher than from the ground truth). Although, the Q values based on SVD normalisation still correlate strongly with the underlying ground truth (**Figure 6-7C**). (**Figure 6-7C)** shows the degree correlation as a function of between layer dependencies. The SVD normalisation clearly follows the degree correlation of the underlying multilayer network. This can also be observed from the strong correlation between ground truth and degree correlation after SVD normalisation (**Figure 6-7D**).

In addition to applying the correction scheme to synthetic data, empirical MEG data were used to analyse the sensitivity of SVD normalisation to underlying changes in network organisation. The multilayer networks are again two-layered networks with a subject's alpha and beta band networks as layers. A subject's given network organisation in these empirical multilayer networks was altered by adopting a rewiring scheme. For a given probability P, matrix elements are randomly swapped within the layers without preserving the degree distribution. (**Figure 6-7E)** shows how multilayer network community structure alters as a function of increasing rewiring probability for original multilayer networks and SVD corrected multilayer networks. The SVD obtained Q values correlate strongly with the Q values obtained from the original multilayer networks (**Figure 6-7G**). The same is also observed for

degree correlation, i.e., SVD corrected DC values correlate strongly with the original DC values (**Figure 6-7F, H**).

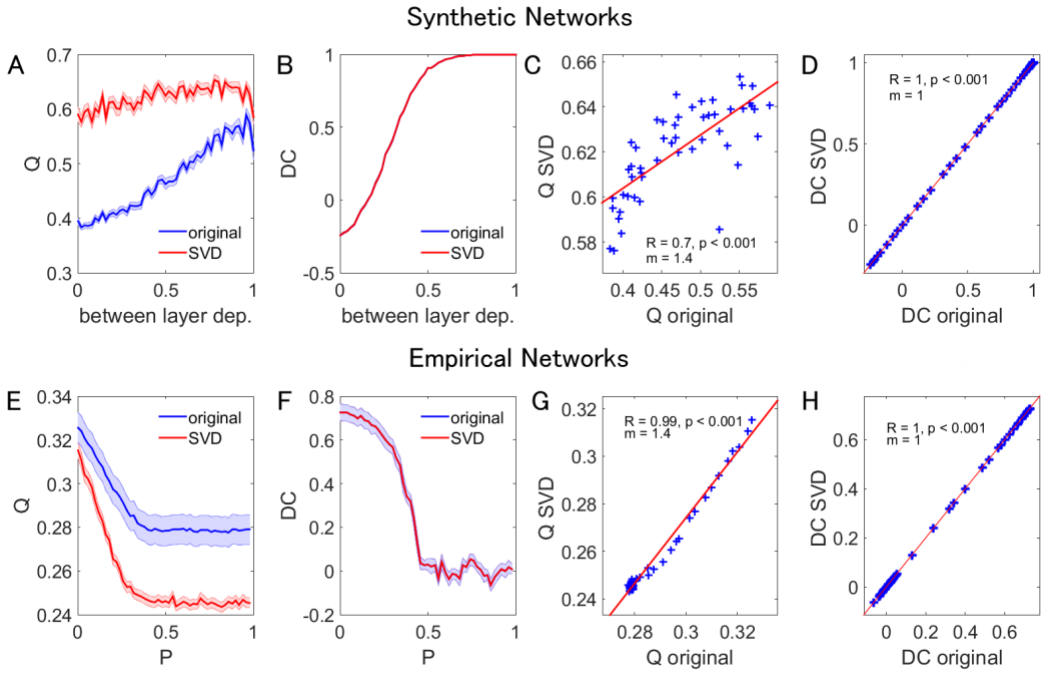


Figure 6-7 *1st row: sensitivity of network metrics to changes in network organisation of the (synthetic) multilayer networks before and after applying SVD. A) Synthetic modular multilayer networks: modularity (Q) as a function of between layer dependency on the ground truth (blue) and SVD corrected networks (red). B) Synthetic scale free multilayer networks: degree correlation (DC) as a function of between layer dependency on the ground truth (blue) and SVD corrected networks (red) (both are completely overlapping). C) Correlation between Q as obtained before and after SVD. D) Correlation between DC as obtained before and after SVD. 2nd row: sensitivity of network metrics to changes in network organisation of the (empirical) multilayer networks. E) Q as a function of rewiring probability (P) for original networks (blue) and SVD corrected networks (red). F) Degree correlation (DC) as a function of rewiring probability for original networks and SVD corrected networks. G) Correlation between Q as obtained before and after SVD. H) Correlation between DC as obtained before and after SVD. The shaded areas in A and B show the mean and standard deviation across realisations (A, B) or subjects (E, F). m in panels CDGH is the slope of the regression line.*

6.4.6 Sensitivity to genuine alterations in multilayer network organisation – correction applied to individual layers in multilayer networks

The sensitivity of network metrics after a correction has been applied to individual layers is now demonstrated. For both generative models, the interlayer dependency was tuned and analysed to show how sensitive the correction schemes are (MST, ECO, SVD normalisation). Effective graph resistance cost minimisation was not used any further since previous analysis **(Figure 6-5C-D**) did not yield in plausible link density. Figure **6-8A)** shows *Q* for the synthetic modular multilayer networks for both the ground truth and correction schemes. All correction schemes overestimate Q, and this overestimation is especially the case for MST and ECO. **Figure 6-8C** shows the correlation between Q obtained from the ground truth and the correction schemes, and the slopes for MST and ECO are smaller than for SVD, indicating that the latter correction scheme is more sensitive to changes in community structure of the underlying ground truth. **Figure 6-8B & D** show the degree correlation between layers as a function of between-layer dependency and the correlation between ground truth DC and DC obtained after application of the correction schemes. DC values for all schemes are almost exactly preserved after applying the correction schemes and correlate strongly to the underlying ground truth.

In addition to synthetic networks, empirical data were used to analyse the sensitivity of network metrics changes in network organisation after correction using SVD normalisation, MST, and ECO. Again, corrections were applied to individual layers. The multilayer networks consist of subjects' beta band MEG network and their fMRI network. A rewiring scheme equivalent to that described in the previous section was used. **Figure 6-8E, G** show *Q* as a function of rewiring probability for the original multilayer network and *Q* values obtained after application of the correction schemes. A good linear fit is obtained between the modularity values for the original network and the values obtained after application of the different correction schemes (**Figure 6-8G**), although the range of values for *Q* obtained after correction

is very different compared to those obtained for the original empirical multilayer network. Since MST and ECO include less weak connections, less influence of noisy connections is potentially driving up Q. Again, for DC, it can be seen that correction schemes follow the original DC values (**Figure 6-8F, H**).

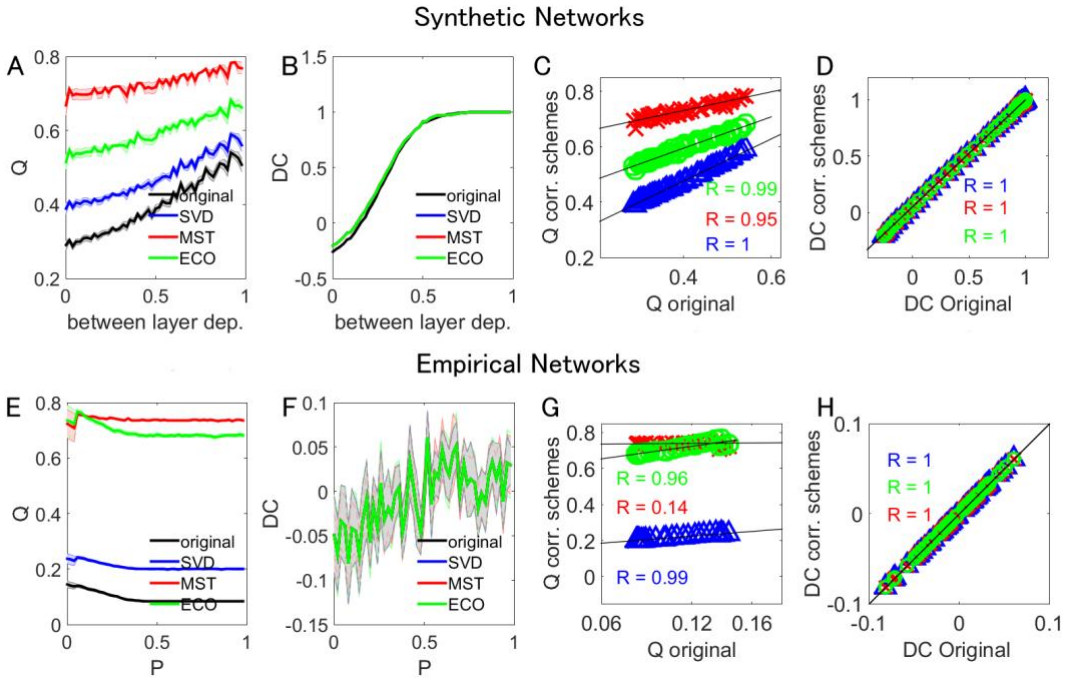


Figure 6-8 *Sensitivity of metrics to changes in network organisation of the (synthetic) multilayer networks. Synthetic modular multilayer networks: Community (Q) as a function of between layer dependency on the ground truth and on corrected networks (A). Synthetic scale free multilayer networks: degree correlation (DC) as a function of between layer dependency on the ground truth and corrected networks (B). Correlation between modularity as obtained before and after correction schemes (C). Correlation DC as obtained before and after correction schemes (D). Sensitivity of the solutions to changes in network organisation of the (empirical) multilayer networks. Empirical multilayer networks: Community (Q) as a function of rewiring probability (P) for original networks (black) and corrected networks (E). Empirical multilayer networks: degree correlation (DC) as a function of rewiring probability (P) for original networks (black) and corrected networks (F). Correlation between modularity as obtained before and after correction schemes (G). Correlation of DC as obtained before and after correction schemes (H). The shaded areas show the mean and standard deviation across realisations (A-B) or subjects (E-F).*

6.4.7 Sensitivity for identification of group differences

Figure 6-7ACEG and **Figure 6-8ACEG** indicate how sensitive multilayer network metrics are to changes in network topology after applying correction schemes. However, such curves are usually not obtainable in empirical studies where the interest lies in the detection of group differences. Two different distributions of Qs were simulated, based on the generative model for multilayer community networks, and we analysed if these differences in distributions can be detected after applying correction schemes. Analysis for DC is omitted since (**Figure 6-7BDFH)**, and (**Figure 6-8BDFH)** show that DC values are almost exactly preserved after applying correction schemes. The wwo simulated conditions were: I) two sets of multilayer networks with a between layer dependency of 0.6 and 10% and 14% random links, respectively; II) two sets with 10% random links, but with a between-layer dependency of 0.4 and 0.7, respectively. Each set consists of 200 multilayer network realisations. **Figure 6-9** shows two sets of Qs for the original networks and for the networks obtained after applying the correction schemes: Q after correction on the whole multilayer SVD_m, Q after correction on individual layers SVD_i, and Q after MST and ECO applied to individual layers. All metrics computed after correction schemes can detect group differences for the conditions I and II (**Figure 6-9A-B**). However, note that most of the correction schemes change the shape of the original distributions (black). Furthermore, note that the two distributions for the SVD_m groups overlap more than the groups for the other correction schemes, which is in line with the smaller slope in (**Figure 6-7)** (the red line) compared to the slopes in (**Figure 6-8)**.

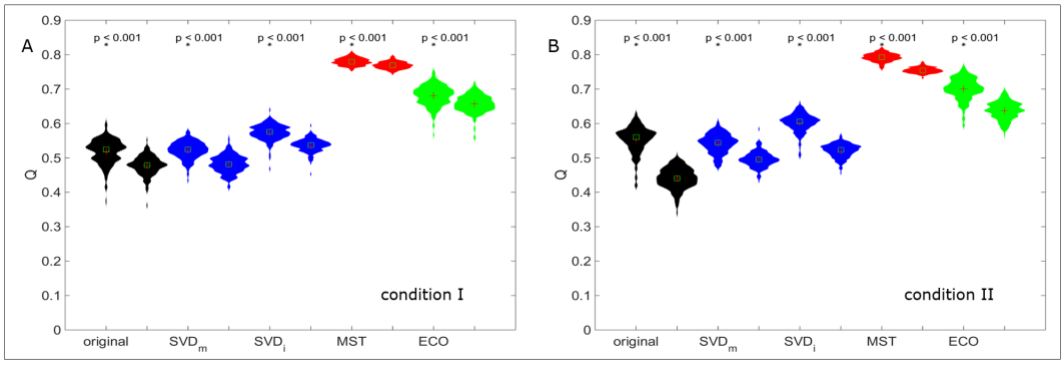


Figure 6-9 *Distributions of Q for two groups. Group differences of multilayer network community structure for the ground truth (black), SVD approach (blue), MST (red), and ECO (green). Both whole multilayer network correction, as well as individual layer correction, are applied for SVD; the former is denoted as SVD_m and the latter as SVDi. A and B refer to two different conditions: I) a different number of random links for the two sets; II) different between layer dependency for the two sets.*

6.5 Discussion

Multilayer network framework allows for the integration of information from different modalities in a unified network, where each layer of the network corresponds to network obtained from different neuroimaging modalities or in the context of M/EEG data, to each frequency band (Brookes et al., 2016; Tewarie et al., 2016). Firstly, four different correction schemes to correct for biases in multilayer network metrics that are due to differences in link density and average connectivity were evaluated.

The following two cases were examined:

1) multilayer networks based on frequency band-specific MEG networks;

2) multilayer networks based on networks from different modalities (fMRI and beta band MEG).

For case 1: only the SVD normalisation sufficiently corrected for biases due to average connectivity, while other schemes could not correct for biases sufficiently.

For case 2: the results showed that the correction schemes MST, ECO and SVD normalisation all corrected successfully for biases due to link density or average connectivity, while effective graph resistance cost minimisation did not result in plausible link densities.

The sensitivity of these approaches to detect changes in the network organisation of the underlying ground truth after these correction schemes were applied was evaluated. Results for case one showed that metrics computed after SVD normalisation were indeed sensitive in identifying alterations in underlying network organisation, while for case two, metrics computed after MST, ECO and SVD were all shown to be sensitive.

For corrections applied to the entire multilayer networks, only the SVD approach resulted in appropriate correction for non-topological biases since this approach corrected for differences in average connectivity of the different layers. This

approach can be applied to complete weighted multilayer networks where different link weight distributions in different layers contain relevant information. For example, in several cognitive experiments, gamma-band connections can be more dominant and relevant in relation to the cognitive demand than other frequency bands (Doesburg et al., 2008; Fries, 2009; Senkowski & Gallinat, 2015). Thus, preserving the dominance of the gamma-band in such conditions would be in line with the relevant task modulations. However, this is not strictly limited to modulations in gamma-band. For example, a working memory task may lead to changes in the theta band (Jensen & Tesche, 2002). Therefore, it is important that the representation of the dominant frequency band (or layer) is preserved even at the network analysis stage. It is worth noting that in conditions where there is a dominant frequency band, individual layer normalisation would likely lead to equally important frequency bands in a multilayer network, this would in turn smear the underlying effects of interest.

The three other correction schemes, applied to the multilayer networks as a whole, did not result in sufficient correction. The ECO correction scheme sometimes led to disconnected multilayer networks, which limits its applicability. The effective graph resistance cost approach led to a plateau of values rather than a local minimum, indicating that not a single link density can be selected as a threshold that maximises flow in the network. The MST applied to the entire multilayer network did not yield unique MSTs. Reconstruction of the MST entirely depends on the ordering of the link weights and non-unique matrix elements can lead to arbitrary ordering. We encountered non-unique values as the interlayer coupling matrix was based on the identity matrix. The higher the threshold, the higher the probability of non-unique values, which leads to the scaling of MST metrics with link density in (**Figure 6-4A)**. In addition, the number of matrix elements in the block-matrix is equal to $(nf)^2$, thus the more layers, the larger the probability to encounter matrix elements with the same values. This problem can be solved by estimation of, for example, one-to-one cross-frequency coupling. Another option is to place random numbers on the diagonal of the interlayer coupling matrices; however, this does not solve the

problem, since different initialisations will result in different non-unique MSTs. Lastly, whilst the MST of the whole multilayer network is by definition connected, its application can lead to individual layers with unconnected components. Empirically, this means that the brain within a frequency band of interest, e.g., alpha band, does not form a connected network. Given the vast literature on electrophysiological networks (Bastos et al., 2015; Larson-Prior et al., 2013), this seems biologically implausible.

Unlike for the whole multilayer network, most correction schemes applied to individual layers were successful in correcting for differences in average connectivity or link density. This approach is sensible when the natural range of link weights in different layers is distinct, due to, for example, the usage of different connectivity metrics or the extraction of networks from different modalities. Only the effective graph resistance cost approach applied to individual layers was not successful, as this led, again, to a plateau of values rather than a local minimum, i.e., no single link density could be selected as a threshold to maximise flow in the network. In addition, the link density at which the plateau was reached was a lot higher than the density of connectomes obtained after ECO (see De Vico Fallani et al., 2017). This indicates the arbitrary nature of this type of corrections.

Metrics computed on the whole multilayer network after SVD correction correlated strongly to the network topology of the underlying ground truth. This was more evident for empirical multilayer networks than synthetic multilayer networks (compare **Figure 6-7A-E**): although metrics computed on SVD corrected synthetic networks followed the direction of change of the underlying topology, there was a decrease in sensitivity to changes in topology, i.e., the red curve (SVD) has a less steep increase than the blue curve (original network) in (**Figure 6-7A)**. The reason for this decrease in sensitivity in synthetic networks is that the SVD approach applied to a sparse network (as was the case for the synthetic networks) can lead to an artificially small noise floor for links that were initially zero in the original network. This is, however, not the case for the fully connected networks found empirically, and as can also be seen from (**Figure 6-7**), where metrics computed on SVD corrected

empirical networks correlated strongly to metrics computed on the original networks. Metrics computed on multilayer networks after individual layer correction all correlated strongly to the network topology of the underlying ground truth. This maintenance of sensitivity also resulted in the sensitivity to detect group differences.

6.5.1 Further discussion on methodological choices and findings

1) The drawback of the SVD correction scheme is that it does not filter potentially noisy connections. It leads to a rescaling that adequately corrects for differences in average connectivity but does not lead to sparse networks like the MST or ECO. There are methods in image processing to perform noise reductions for matrices based on SVD (De Moor, 1993); however, non-smoothness in a weighted adjacency matrix can be genuine and does not necessarily imply noise. If one is interested in obtaining a sparse multilayer network and when correction to the entire multilayer network is required, one potential option to solve the problem of noisy connections could be a sequential correction: first a link weight normalisation based on SVD on the whole multilayer network followed by extracting an MST or applying ECO on individual layers with preservation of the link weights.
2) If a weighted adjacency matrix is symmetric, then an SVD approach is equivalent to an eigenvalue-decomposition approach. This would mean that we are normalising the eigenvalues of the weighted adjacency matrix by the largest eigenvalue (see **section 6.3.4** for justification). The advantage of SVD, however, becomes apparent when directed networks are treated since these networks correspond to non-symmetric matrices for which an eigenvalue-decomposition approach could lead to complex eigenvalues.
3) Multilayer networks were treated based on either different MEG frequency-band specific networks obtained using the same connectivity metric or a two-layered network consisting of MEG and fMRI networks. However, the flexibility of the multilayer network also allows the construction of networks

of various kinds. Correction of such networks can be performed by combining the currently explored methods. Examples of different flavours of multilayer networks can be a number of frequency-band specific MEG networks obtained with a connectivity metric, stacked with a number of MEG networks obtained with a different connectivity metric or a multilayer network consisting of different frequency-band specific MEG networks together with a fMRI and structural network. In these cases, one could apply correction schemes to specific subsets before joining the sets together. For example, apply an SVD to all layers obtained with a single metric as a whole, apply SVD on the individual fMRI network layer, and apply SVD on an individual structural network layer.

4) In the current setting and for simplicity, the one-to-one coupling between layers was evaluated, but there is no methodological hurdle to apply the explored approaches to multilayer networks with richer and more realistic between-layer coupling matrices.
5) (**Figure 6-8F)** shows the correlation between the degrees of MEG beta band networks and fMRI network from individual subjects. These values are very low but can be explained by the fact that similarity between fMRI and MEG networks are much more apparent when averaging over subjects (Brookes et al., 2011; Tewarie et al., 2016).
6) Note that all multilayer network results from empirical data will be influenced by methodological choices prior to calculation of multilayer network metrics such as the connectivity metric of choice (Colclough et al., 2016), source localization method, and forward model for MEG (Hincapié et al., 2017), and the parcellation scheme (Proix et al., 2016; Lord et al., 2016).
7) It is important to realise that any correction scheme or sampling method comes with the risk of leaving out genuine connections. Filtering can, therefore, influence group differences after applying correction schemes. In addition, applying correction schemes can leave the relative response to a perturbation intact, but the magnitude of the network metrics may change.

8) Lastly, although a fair number of network metrics were enumerated and evaluated, the choice of metrics could have influenced the stability of the results. It is important to stress that the proposed correction schemes have been evaluated within the limits of the current datasets, pipelines, and network metrics. The evaluation of other network metrics and approaches in the context of other generative models and connectivity metrics also deserves further attention in future work.

A specific set of four correction schemes were used in the current study, despite the presence of more proposals in the literature. The reason to restrict to this specific set of approaches is for clarity and the ease with which these approaches can be applied to neuroscientific data. Other approaches not explored in the current study include a recently introduced statistical method to test the null hypothesis that a sample of networks are generated by the same random process (Fujita, Vidal, & Takahashi, 2017), a multi-threshold permutation correction method (Drakesmith et al., 2015), a clustering optimisation approach (Smith et al., 2015), the union of shortest-paths (Meier et al., 2015), and the minimally connected component (Jalili, 2016). The disadvantage of the latter is, however, that connectedness of the network is not guaranteed. In the current study, some of the explored approaches (ECO and MST) guarantee a fixed link density, which avoids biases due to differences in link density between groups. The union of shortest-paths does, however, the exact opposite: A specific topological network is fixed, which allows one to detect for which density this topology emerges.

To conclude, similar to single-layer networks, multilayer networks are also affected by non-topological biases of the network such as differences in link density and average connectivity. Whenever these biases are left uncorrected, this could lead to a risk of unreproducible results between centres and studies in a similar manner as for single-layer networks. Based on the findings presented in this chapter, the use of correction schemes prior to multilayer network analysis for group comparisons is

recommended. These approaches include – whenever a multilayer network consisting of networks obtained from different modalities is in question, one can apply either MST, ECO or SVD correction schemes to its individual layers. However, when treating a multilayer network where the layers correspond to complete networks obtained from the same modality and connectivity metric (based on the present analysis), SVD is a recommended approach. Future studies should explore the applicability of other existing approaches in the context of multilayer networks.

CHAPTER 7

7 Musical training-related differences in brain's resting state

Précis

Using a novel method for between-group comparisons of functional brain networks (developed in this thesis, **chapter 6**), the current chapter studies MEG differences between individuals with vs. without musical training. The ability to proficiently play a musical instrument requires a fine-grained synchronisation between a number of sensorimotor and cognitive brain regions, acquired through training and reflecting cortical dynamics over years. Previous studies demonstrated that the brain undergoes structural changes with intensive training and that behavioural specialisation is reflected in brain activation patterns during music-related tasks. The question whether such specialisation extends beyond music-related tasks was studied here as a test case for the novel method, based on MEG data from task-free, resting-state conditions. Consequently, multilayer network analysis (**chapters 5 and 6**) was applied to resting-state MEG data from participants with musical training (n=31) and those without (n=31). To obtain a sufficiently large sample of participants, the study used publicly available data from the Open MEG Archive.

The analysis revealed that musicians show a modular organisation that spans visuomotor and frontotemporal areas, which are involved in the execution of a musical performance. This twofold modular structure was found to be significantly different from non-musicians. The differences between the two groups are primarily seen in the theta (6.5-8 Hz), alpha1 (8.5-10 Hz) and beta1 (12.5-16 Hz) frequency bands. The novel method demonstrated that musicians have a highly integrated resting state network organisation compared to non-musicians. In conclusion, network analysis based on resting-state data revealed training-related changes in functional network organisation, even at rest and outside of the trained behaviour.

7.1 Introduction

Musical training is a commonly used model to study training-related brain plasticity (Herholz & Zatorre, 2012; Jäncke, 2009; Zatorre & McGill, 2005). This research is largely motivated by the fact that achieving high levels of proficiency in any given musical instrument requires years of focused training. Numerous studies have reported structural brain changes due to musical training. For example, increased size of the anterior half of the corpus callosum (Schlaug et al., 1995), and differences in the cortical representation of the hand motor area (Amunts et al., 1997; Elbert et al., 1995). More specifically, the brain also undergoes changes that pertain to the demands posed by the particular type of musical training, i.e., pianists showed a left hemisphere dominance, whereas violinist showed right hemisphere advantage (Bangert & Schlaug, 2006). Robust changes in grey matter specific to auditory, motor, and visuospatial regions have also been reported (Gaser & Schlaug, 2003). This anatomical specialisation is potentially the result of years of musical training that requires fine-grained communication between several cortical areas. For example, musicians showed an increased coupling between auditory and pre-motor areas (Grahn & Rowe, 2009), which is one of many processes that occur in musicians during a performance.

It is worth noting that the training-related plastic changes are not unique to musicians but can be seen in groups of subjects with some degree of behavioural specialisation. For instance, training-related white matter changes have been observed in healthy adults (Scholz et al., 2010), professional golfers (Jäncke et al., 2009), and London taxi drivers (Maguire et al., 2000).

The majority of the evidence of functional specialisation in musicians comes from structural data (white or grey matter changes) or task-based functional data. Little attention has been paid to the analysis of functional data recorded during resting state, capturing spontaneous, non-task-related brain activity. As a result, it is not clear if signatures of long-term musical training can be detected in ongoing brain activity.

To better characterise the relationships between anatomical regions from the task-free data, functional connectivity approaches have proved useful. It must be noted that either a seed-based or whole-brain functional connectivity analysis can only inform us about the strength of these connections. Going a step further, studying the pattern of these connections can give us more information about the functional network as a whole. Using a seed-based connectivity approach to resting state fMRI in musicians, (Luo et al., 2012) demonstrated an increased functional connectivity in auditory, visual, and motor areas. Similarly Tanaka and Kirino (2017), also demonstrated an increased functional connectivity in the thalamo-cortical network in musicians. Using a whole-brain analysis of fMRI Alluri et al. (2017) reported that musicians recruit action-based brain networks, while non-musicians recruit perception based networks in a naturalistic listening paradigm.

Analysis of resting state networks is not limited only to fMRI but has also been a significant part of the human electrophysiological research based on MEG (Brookes et al., 2011; Hillebrand et al., 2012) and EEG (Smit et al., 2008; Stam et al., 2005). However, to the best of our knowledge, only one recent study (Klein et al., 2016) has explored resting state EEG differences between musicians and non-musicians. The authors analysed high density EEG resting state data obtained from musicians with graph theoretical approaches. They reported that musicians showed an increased intra- and inter-hemispheric functional connectivity between auditory, sensorimotor, and prefrontal cortex in theta (6.5-8 Hz), alpha1 (8.5-10 Hz), and alpha2 (10.5-12 Hz) frequency ranges. A limitation of this study is that separate frequency-specific networks were studied in isolation (also referred to as analysis of single-layers), which ignores the pan-spectral picture of ongoing brain connectivity.

To overcome this limitation, the present study used a multilayer network framework, combining data obtained from multiple frequency bands in one single network description (Brookes et al., 2016; Tewarie et al., 2016b; Mandke et al., 2018). Generally, a multilayer network is a network of networks, which is made up of individual networks as layers that are interconnected via some relationship (a more formal introduction to multilayer networks follows in the methods section).

Multilayer network approaches have recently been introduced in the field of neuroscience where different layers of the network correspond to different M/EEG frequency bands (frequency-specific networks) or networks obtained from different neuroimaging modalities (Bassett et al., 2010; Brookes et al., 2016; De Domenico, 2017; Mandke et al., 2018; Tewarie et al., 2016b; Yu et al., 2017).

Most complex networks – including multilayer networks – exhibit a certain level of modularity, i.e., densely connected groups of nodes (brain regions) form clusters (modules). Numerous neuroimaging studies have reliably shown that human brain architecture is highly modular (Power et al., 2011; Yeo et al., 2011). Modules have been suggested to sub-serve information processing (Sporns & Betzel, 2016). The modular organisation of the brain begins early in life and matures during the adolescent years (Baum et al., 2017). This development of modular organisation allows for cortical specialisation Bassett et al. (2011) have shown that reorganisation also occurs with learning. Accordingly, brain networks in musicians as a result of training may reorganise to facilitate communication between sensory, motor and cognitive areas of the brain.

In the present study, resting-state MEG recordings from musicians and non-musicians obtained from the Open MEG Archive (Niso et al., 2016) were investigated. An established single-layer analysis method (Network-Based Statistics toolbox, Zalesky, Fornito, & Bullmore, 2010), and a novel multilayer network approach, with layers representing MEG frequency bands, were used to evaluate the data. In the absence of a statistically significant between group-difference in single-layer analysis, a presence of a difference in multilayer analysis would highlight the added value of the latter approach. This study of resting-state MEG data had the primary aim to identify neuronal signatures of behavioural specialisation or changes due to training-related plasticity (musical training). The focus was on identifying the modularity of resting-state networks within and between individual MEG frequency bands ("pan-spectral" modularity). It was hypothesised that the years of musical training would have changed the modular structure of the musicians' brains in comparison with non-musicians.

7.2 Methods

7.2.1 Participants and MEG data pre-processing

All MEG data analysed in this study were obtained from a public access data repository, Open MEG Archive, OMEGA (Niso et al., 2016). At the time when the analysis was performed, the OMEGA repository contained MEG data from 150 healthy controls. The repository also includes self-report questionnaire data. Out of the questionnaire data, the self-reported musical experience was used to classify healthy participants into two groups. 5-min resting-state MEG recordings acquired on a 275 channel CTF-MEG system were used (MISL, Coquitlam, Canada) as detailed in Niso et al. (2016).

The first group included data from participants that had no history of neuro-psychological problems and 5+ years of experience playing some musical instrument. Out of this group, individuals whose structural MRI data were not suitable for the procedure of co-registration with MEG were excluded. Further participants were excluded based on unusual sensor level power spectra (Gross et al., 2013). The 31 subjects that passed the quality checks formed the experimental group (musicians). Out of the 31 musicians, 23 were professional musicians and 8 can be considered as amateur musicians. This group was a heterogeneous sample, as it included a wide range of musical expertise playing instruments (e.g. string instruments, percussions etc.).

The second (control) group included data from neurologically healthy OMEGA participants who did not play any musical instrument. Using the same exclusion criteria as for the musicians' group, a further 31 participants were identified (age and gender-matched) for the control group. Further data of the altogether 62 participants (31 in each group, all right-handed by self-report) are given in (**Table *7-1***).

Table 7-1 Summary of statistics for both groups

	Musicians	**Non-musicians**
Gender	M: 20; F: 11	M: 20; F: 11
Age	Mean: 28.25 years; SD: 7.25	Mean: 27.48 years; SD: 5.95
Years of experience	Mean: 13.25 years; SD: 5.04	no experience

M: male, F: female

The raw data included task-free, 5-mins eyes open resting-state MEG scans, sampled at 2400 Hz (Niso et al., 2016). As part of the pre-processing, the data were down-sampled at 600 Hz. A third-order synthetic gradiometer configuration of the CTF-MEG system was applied; a 150 Hz low pass anti-aliasing filter was used. The OMEGA repository also provides the participant's digitised head shape (Polhemus). Using the Polhemus files, a surface matching of the digitised head shape to an equivalent head shape extracted from individual anatomical scans were performed. This was to allow for co-registration of MEG sensor geometry and brain anatomy.

7.2.2 Source localisation using an atlas based beamformer

An atlas-based beamforming approach (Hillebrand et al., 2012) – previously also used in (Brookes et al., 2016; Tewarie et al., 2016a; Tewarie et al., 2016b) – was applied for source localisation. The cortex was parcellated using the AAL (Tzourio-Mazoyer et al., 2002). Out of the 116 AAL regions, 78 cortical regions that provide a full cortical coverage were selected and the remaining 38 subcortical and cerebellar regions were ignored. A beamformer approach (Robinson & Vrba, 1998) was employed to generate a single time course of electrophysiological activity within each of these regions. To achieve this, the centre of mass was first derived for each region. Given the spatial resolution of MEG (Barnes et al., 2004), voxels were defined on a regular 4 mm grid covering the entire region, and the beamformer-estimated time-course of

electrical activity was derived for each voxel. To generate a single time course representing the whole region, individual voxel signals were weighted according to their distance from the centre of mass using a Gaussian weighting function. This procedure ensures that the regional time course is biased towards the centre of the region, with a full-width half maximum of approximately 17mm. To calculate individual voxel time courses, a scalar beamformer was used (Robinson & Vrba, 1998). Covariance was computed within a 0.5-150 Hz frequency window and a time window spanning the entire experiment (300s) (Brookes et al., 2008). Regularisation was applied to the data covariance matrix using the Tikhonov method with a regularisation parameter equal to 5% of the maximum eigenvalue of the unregularised covariance matrix. The forward model was based upon a dipole approximation (Sarvas, 1987) and a multiple local sphere head model (Huang et al., 1999). Dipole orientation was determined using a non-linear search for optimum signal to noise ratio (SNR). Beamformer time courses were sign flipped where necessary to account for the arbitrary polarity introduced by the beamformer source orientation estimation. This process resulted in 78 electrophysiological time courses, each representative of a separate AAL region. This approach was applied to each subject individually.

7.2.3 Functional connectivity calculation

The time courses were frequency filtered in theta (6.5-8 Hz), alpha1 (8.5-10 Hz), alpha2 (10.5-12 Hz), beta1 (12.5-16 Hz), beta2 (16.5-20 Hz), this frequency selection was motivated by the recent work on training-related plasticity (Klein, et al., 2016; Langer et al., 2013). After frequency filtering, to correct for signal leakage, frequency filtered time courses were subjected to a multivariate orthogonalisation (Colclough et al., 2015). Using the Hilbert transform, an amplitude envelope was computed by calculating the absolute value of the analytical signal. The envelopes of all the frequency bands were down-sampled to 4 Hz (Brookes et al., 2011; Luckhoo et al., 2012). Finally, a functional connectivity matrix was reconstructed for individual

frequency bands by computing Pearson's correlation coefficient between down-sampled envelope pairs, with each correlation coefficient forming a single element in the weighted adjacency matrix (Hipp et al., 2012; O'Neill et al., 2015; Tewarie et al., 2016b). This produced a square (78 nodes x 78 nodes) off-diagonal weighted adjacency matrix for each frequency band under consideration.

Furthermore, to explore seed-based connectivity, the following regions were used – left and right supplementary motor area (SMA, nodes 12 and 51 in AAL atlas) and left and right precentral gyrus (nodes 14 and 53 in AAL atlas) (review: Jäncke, 2009). A linearly constrained minimum variance beamformer was used to project data to these regions. Following this, amplitude envelope correlations were used to estimate functional connectivity between these regions across participants.

The primary aim of this study was to identify global changes following musical training in MEG resting-state networks. The secondary aim was to investigate changes in functional connectivity in motor regions that have previously shown structural and functional changes (in task-based data) following musical training.

7.2.4 Single-layer analysis using Network-Based Statistics

To test if the effects of musical training can be detected in raw adjacency matrices, a single-layer analysis using the Network-Based Statistics (NBS toolbox, Zalesky et al., 2010) was performed. For technical details on NBS, the reader is redirected to the original article (Zalesky et al., 2010). A summary of NBS is as follows: In a typical cross-sectional design, NBS identifies significant between-group differences in pairwise associations, where such associations are links or connections between two nodes. A given symmetric $N \times N$ connectivity matrix has a maximum $N(N-1)/2$ individual connections. Using M independent permutations, a t-statistic is estimated for all individual connections. Then links that exceed a certain threshold with their respective t statistic are retained, which forms the supra-threshold network. The size of the biggest connected component found in this resulting network is used as a test

statistic. The *p*-value of an observed component is calculated by finding the number of permutations for which the maximal component size exceeds the original test statistic, normalised by *M*. The component size is determined by its total number of connections, this is called the *component extent*. Extent is better suited to detect weaker experimental effects that span over many connections. In addition to this, NBS also offers another measure of component size, which is called *component intensity* and is calculated by summing the test statistic values across all the connections of the component. Intensity is the appropriate choice for detecting effects that are strong but focal, spanning relatively fewer connections. It can also detect strong effects with distributed topology. To identify group differences using NBS, M=5000 permutations were used with independent samples *t*-test (p<0.05). The group differences were tested using both component extent and component intensity.

7.2.5 Multilayer network construction

Multilayer network construction has been explained in the previous sections (**section 5.6**). However, for continuity, this is explained briefly and specifically how it has been adapted for this data.

A multilayer network is a complex network structure, which is a network of networks, where each layer is formed by an individual network. The links in such a network describe relationships between combinations of all possible nodes and layers. In this study, multilayer networks were constructed by integrating information from theta (6.5-8 Hz), alpha1 (8.5-10 Hz), alpha2 (10.5-12 Hz), beta1 (12.5-16 Hz), beta2 (16.5-20 Hz) frequency bands, where each network or layer shared the same number of nodes (78 cortical regions). The links in each layer were the amplitude envelope correlation (AEC) weights within that frequency band. (**Figure 7-1**) shows a schematic of multilayer network construction.

Mathematical representation of a multilayer network is its block-adjacency matrix (De Domenico et al., 2013; Van Mieghem, 2016). An *f*-layered multilayer network can be written in the form of a block-adjacency matrix (Sahneh et al., 2015) as follows:

$$A = \begin{bmatrix} A_1 & H_{12} & \dots & H_{1f} \\ H_{21} & A_2 & & \vdots \\ \vdots & & \ddots & \\ H_{f1} & \dots & & A_f \end{bmatrix}, \qquad \textbf{(7.1)}$$

where A_α corresponds to a symmetric, square adjacency matrix of a layer α, $1 \leq \alpha \leq f$. In our case A_α corresponds to individual frequency-specific networks. The matrix H_{kl} corresponds to the coupling matrix between the layers k and l, where $1 \leq k, l \leq f, f = 5$. The frequency-specific networks, A_α, have the same dimensions for all layers (N x N, N=78), implying that every layer of the network has the same number of nodes or brain regions.

In line with previous studies (Guillon et al., 2017; Yu et al., 2017), one-to-one between layer relationship was chosen, with links only between the same nodes (brain regions) over all the layers, i.e. $H_{kl} = cI$ was chosen, where c is a constant (here the mean connectivity calculated over all the individual layers) and *I* the identity matrix. The choice of *c* follows from the results presented in the previous chapter as the SVD normalisation method mainly corrects for differences in average connectivity (see **Figure 6-4C**). For a discussion on the parameter *c,* see **section 7.4.1.** As between-layer links are limited to the same nodes across all layers, the cross-frequency coupling between non-identical areas in different layers is ignored.

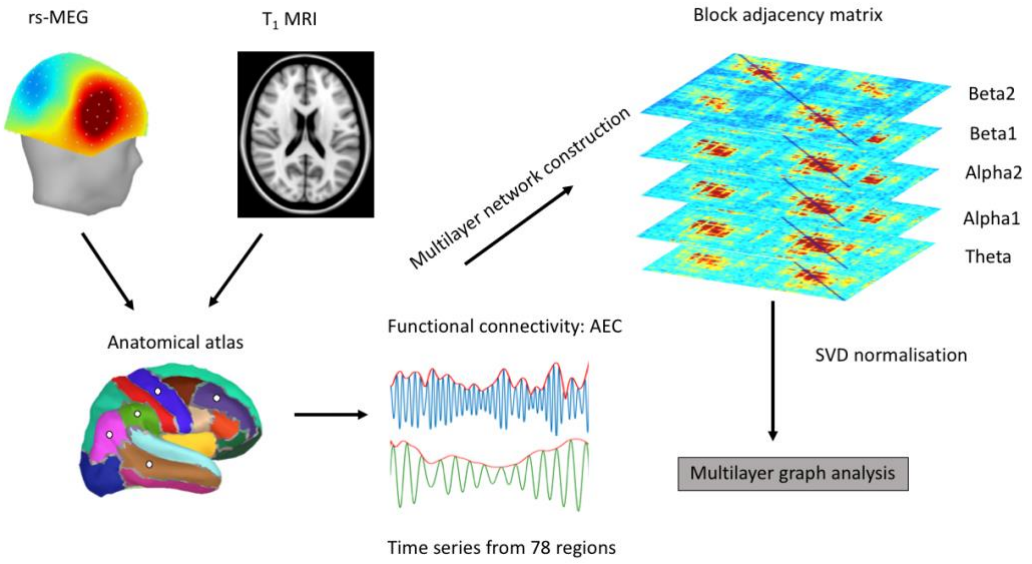


Figure 7-1 *A schematic of the analysis pipeline used in the construction of multilayer networks. Here, a special case of the multilayer networks is used: multilayer networks with one-to-one between layer coupling. rs: Resting-state, AEC: Amplitude envelope correlations. Theta: 6.5-8 Hz, Alpha1: 8.5-10 Hz, Alpha2: 10.5-12 Hz, Beta1: 12.5-16 Hz, Beta2: 16.5-20 Hz*

7.2.6 Graph analysis of multilayer networks

A multilayer network was constructed for every participant in the two groups. However, comparing raw block-adjacency matrices between groups can be biased due to differences in link weights, i.e., such a comparison can inflate false positives or negatives (Mandke et al., 2018). These biases in the context of multilayer networks arise due to differences in average connectivity (van den Heuvel et al., 2017). To correct for such biases a recently introduced SVD based normalisation approach was used (Mandke et al., 2018). Prior to subjecting the block-adjacency matrix to graph analysis, all singular values were normalised by the largest singular value of the weighted adjacency matrix to correct for the difference in mean connectivity between groups. For a given block-adjacency matrix, A, a singular value decomposition $A = U\Lambda V^T$ was applied, where U and V contain the left and right singular vectors and Λ the singular values of A. To correct for differences in average

connectivity, Λ was rescaled by the largest singular value λ_1. The rescaled matrix would thus become $\tilde{A} = U\left(\frac{10}{\lambda_1}\Lambda\right)V^T$. The multiplication by 10 is used to ensure that the range of values in $\tilde{A}$ is not too small and varies between 0 and 1. The choice of using the largest eigenvalue is justified in **section 6.3.4.** As the connectivity data used in constructing the multilayer network was computed using AEC, the SVD normalisation was applied to the whole adjacency matrix. This follows from the results shown in **section 6.4.2** and findings published in Mandke et al. (2018).

To identify community structure specific to musicians, a community detection algorithm was used, details of which are given in the next paragraph. Multilayer network formulation allows to study various between layer relationships. Degree correlations (DC) is one of such measures that enables the study of the correspondence between hubs in different layers. DC can be derived by calculating a Pearson correlation coefficient between degree sequences of different layers (Battiston et al., 2014; Mandke et al., 2018), where degree provides a measure for "importance" of a given node. In the case of weighted networks, node strength (i.e., the sum of the link weights surrounding a node) is used instead of degree. Here, the focus was on DC as a measure of the relative importance of a given node and modularity to go beyond individual nodes and study their higher-order organisation.

Community detection algorithms (e.g., Blondel et al., 2008) have widely been used to study resting-state fMRI networks and structural data (Crossley et al., 2013; Garcia, Ashourvan, Muldoon, Vettel, & Bassett, 2018; Sporns & Betzel, 2016). Generally, communities in a network are obtained by optimising a quality function, e.g., modularity (Newman, 2006), which provides an index for within-community and between-community connections. The multilayer modularity (Q) as expressed in (Bassett et al., 2013) is as follows:

$$Q = \frac{1}{2u_{tot}} \sum_{ijlk} \left[\left(\tilde{A}_{l,ij} - \gamma_l \frac{{}_l d_i \; {}_l d_j}{2 \sum_i {}_l d_i} \delta_{lk} \right) + \delta_{ij} H_{lk,j} \right] \delta_{g_{il}, g_{jk}} \qquad \textbf{(7.2)}$$

where u_{tot} is the total link weight in the network, γ_l is the resolution parameter, g_{il} is the community assignment of node *i* in layer *l*, and δ_{ij} is the Kronecker delta function (meaning that δ_{ij}*=1 if i=j* and δ_{ij}*=0* if *i≠j*). Using this community detection algorithm, individual nodal module assignments expressed as indices were calculated. Nodes with the same index can be said to be part of the same community. Each subject's block-adjacency matrix was subjected to community detection algorithm. Using the resulting index assignments, an agreement (consensus) matrix (*N x N*) was estimated for every layer per group, where each element in the matrix corresponds to the proportion of the number of times two given nodes were part of the same community over all individual subjects (Baum et al., 2017). Furthermore, a collapsed agreement matrix was obtained by averaging over all individual layer agreement matrices. This step was performed to achieve a group-level representation of the entire multilayer network.

To compare the multilayer community structure between groups (musicians vs. non-musicians), each of collapsed agreement matrices were subjected to the same community detection algorithm (**Equation 7.2**), resulting in a partition of the 78 nodes into a number of communities (Baum et al., 2017). To identify whether the community assignments between the groups are similar or dissimilar the adjusted Rand index was used (Traud et al., 2008), which also takes into account chance correlations. For any two given partitions A and B, the adjusted Rand index achieves a maximum score of 1 if they are perfectly similar, and 0 if they have no overlap.

7.3 Results

7.3.1 Functional connectivity and Network Based Statistics

Seed-based connectivity analysis for the 4 nodes under consideration (bilateral SMA and pre-central gyri) did not reveal any statistically significant ($p<0.05$) differences between the two groups.

After performing SVD normalisation, for a visual representation of the data, functional connectivity estimates between all nodes for all frequency bands (theta, alpha1, alpha2, beta1, beta2) obtained using AEC were averaged across participants (**Figure 7-2:** musicians, **Figure 7-3:** non-musicians). In the figures, only the top 40% of the connections were subsequently plotted in brain space to visualise the underlying networks.

After computing individual connectivity matrices, a single-layer analysis using NBS was performed. The effects using NBS were assessed using both extent and intensity options provided as part of the toolbox. However, this failed to show any significant effect with stringent statistical thresholding ($p<0.05$, FWER-corrected) across frequency bands. A null result using NBS is possible because of a number of reasons:

1) The single-layer analysis ignores the pan-spectral picture in the data, which warrants a more integrative approach.

2) High differences in link weights can smear underlying experimental effects and this demands some corrections as highlighted in (Mandke et al., 2018; van Wijk et al., 2010).

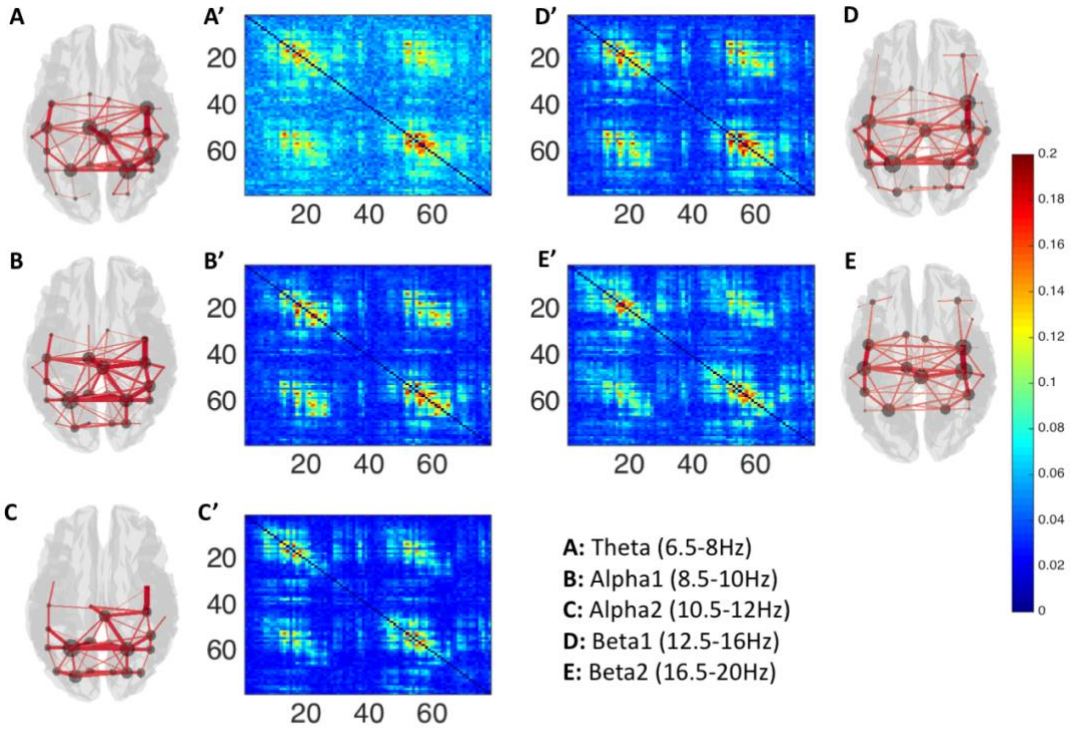


Figure 7-2 *Averaged AEC in adjacency matrix (78 brain area labels on each axis: 1-39 left hemisphere, 40-78 right hemisphere) across musicians (A' to E') and its corresponding source space (top 40% of the connections) representation (3D plots, A to E) in the 5 frequency bands under consideration. All adjacency matrices show typical patterns of high-AEC within left hemisphere (upper left quadrant), within right hemisphere (lower right quadrant) and between hemispheres (upper right quadrant). In the 3D plots, lines indicate presence of connections, with thicker lines corresponding to stronger connections. The circles in the 3D plots indicate summed magnitude of link weights (node strength, weighted degree) between the node and rest of the brain.*

Non-musicians

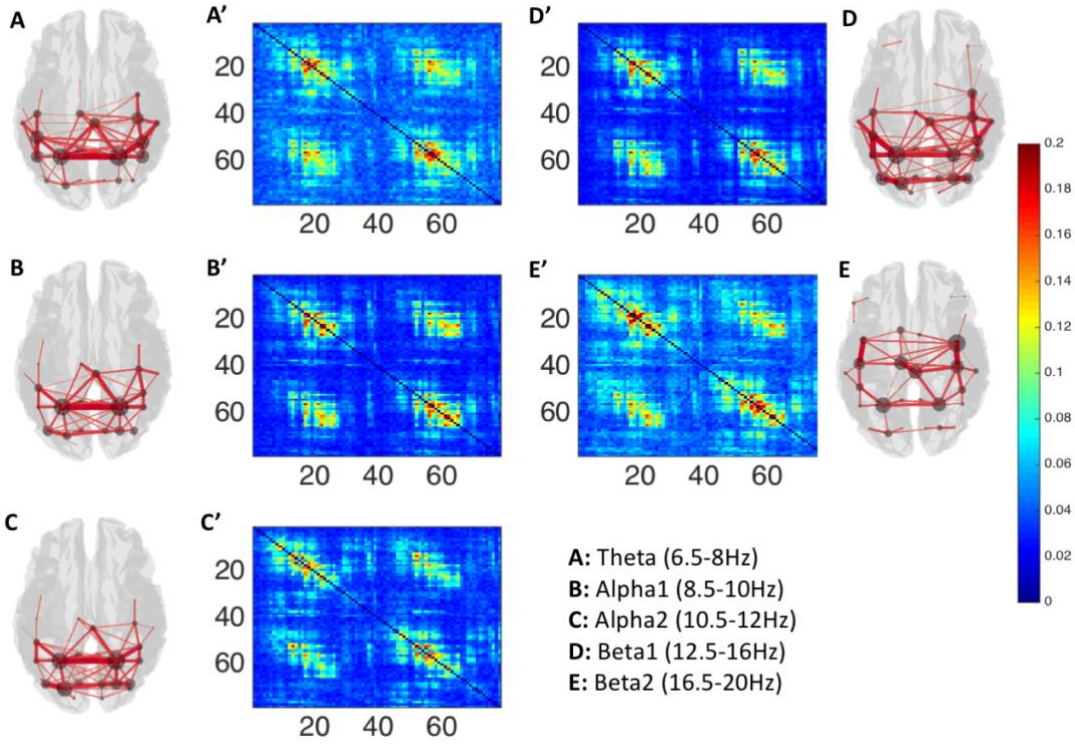


Figure 7-3 *Averaged AEC plotted as adjacency matrices across non-musicians (A' to E') and their corresponding source space (top 40% of the strongest connections) representation (3D plots, A to E) in 5 frequency bands under consideration. All adjacency matrices show typical patterns of high-AEC within left hemisphere (upper left quadrant), within right hemisphere (lower right quadrant) and between hemispheres (upper right quadrant). In the 3D plots, lines indicate presence of connections, with thicker lines corresponding to stronger connections. The circles in the 3D plots indicate summed magnitude of link weights (node strength, weighted degree) between the node and rest of the brain.*

7.3.2 Graph analysis of the multilayer networks

7.3.2.1 Community structure

The block-adjacency matrices of the two groups were subjected to community detection algorithm after SVD normalisation. Multilayer modularity (Q) was

calculated for individual subjects' SVD normalised multilayer networks (**Figure 7-4**) and was significantly different between groups (p=0.033, Wilcoxon rank-sum test). To further understand the link between musical training and neural connectivity findings, a correlation between the years of musical training with modularity was obtained, but this correlation was not found to be significant (p=0.8).

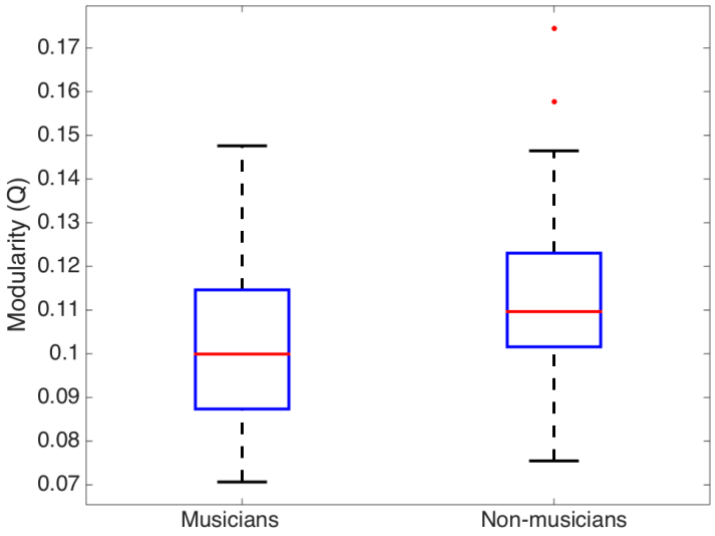


Figure 7-4 *Boxplots of modularity (Q) for the two groups. This difference was found to be statistically significant (p=0.033 Wilcoxon rank-sum test). The top and bottom of each box represent 25th and 75th percentile respectively (also defining the interquartile range), and the red line in the middle shows the median of that sample. Whiskers extend from the ends of the interquartile range to the furthest non-outlier observation. Outliers (red dots) are defined as values above or below 1.5 times the interquartile range, measured from top or bottom of the box.*

The group of musicians demonstrated different modular organisation than the non-musicians (adjusted Rand index: 0.568). The group representation of this modular organisation for both groups is shown in (**Figure 7-5**). The multilayer network community structure observed in musicians had two large communities, while non-musicians had three communities. Musicians showed a modular structure that encompasses both visual and motor networks, shown in red (**Figure 7-5**, left panel),

and frontal and temporal regions, shown in blue. In non-musicians, the modularity analysis revealed three modules, the frontal (colour: blue), midline-temporal (colour: green) and posterior (colour: red) network components. The non-musicians showed distinctly different community structure from the group of musicians. In non-musicians, the visual and motor networks are segregated from one another (as shown in red and green respectively), whereas musicians display integrated visuomotor networks. In addition, the musicians also exhibit markedly different patterns of connectivity spanning the frontotemporal regions, in particular in the right hemisphere, with the integration of inferior frontal and superior temporal regions into a single community only in musicians (**Figure 7-5**, left panel).

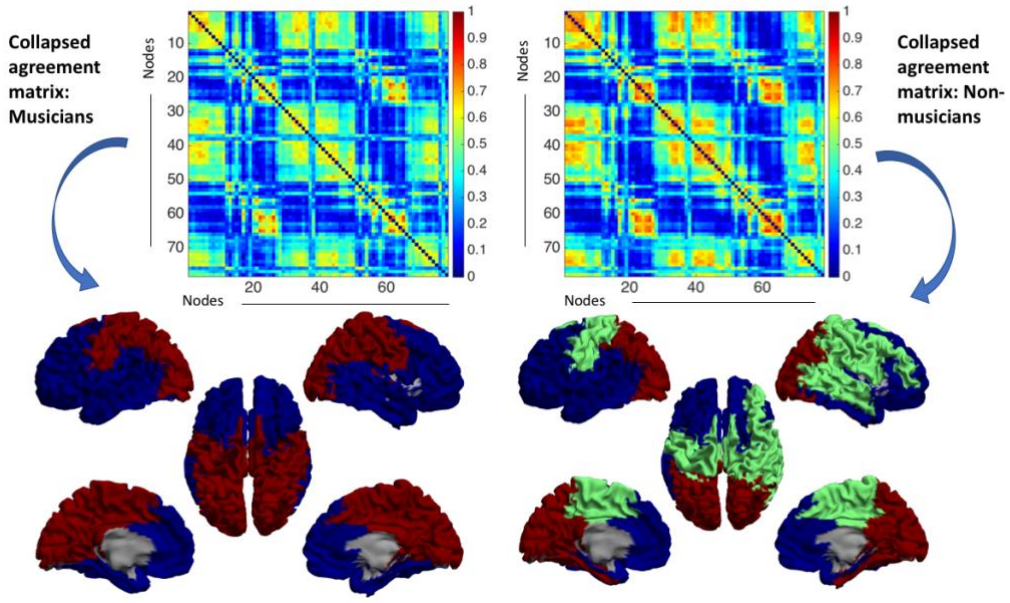


Figure 7-5 *Schematic representation of collapsed agreement matrix computed for both groups. The collapsed agreement matrices were subjected to community detection algorithm. The community assignment was subsequently plotted in brain space to reveal group-level representation. Identical colours belong to the same community.*

7.3.2.2 Degree correlations

One aspect of between layer relationships is the correspondence between hubs in different layers, which can be quantified using DC. Degree correlations between all combinations of layers were calculated. Out of all the layer combinations only statistically significant ($p<0.05$, Wilcoxon rank-sum test) pairs are shown in (**Figure 7-6**). The left panel in (**Figure 7-6**) shows the DC difference between layer 1 (theta) and layer 4 (beta1) and the right panel displays the DC difference between layer 2 (alpha1) and layer 4 (beta1) between groups.

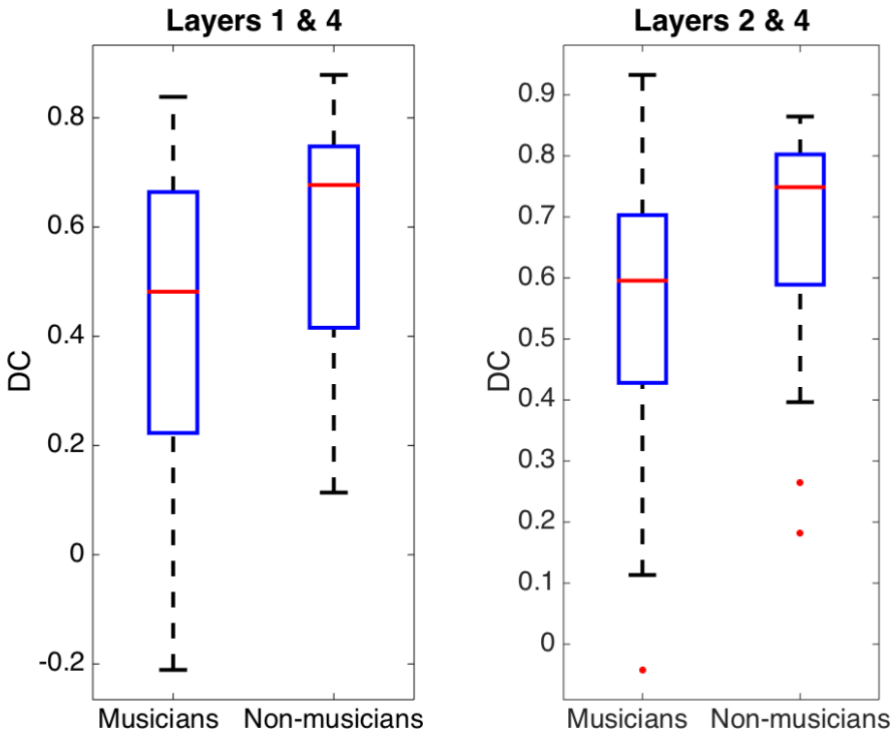


Figure 7-6 *Boxplots of degree correlations. Only the layer pairs that showed significant differences are plotted. The left panel shows significantly different DC between theta layer (layer 1) and beta1 layer (layer 4) (p=0.045, Wilcoxon rank-sum test). Right panel shows significantly different DC between layer 2 (alpha1) and layer 4 (beta1), (p=0.031, Wilcoxon rank-sum test). Box- and whisker plots as in (**Figure 7-4**).*

7.4 Discussion

The study aimed to detect the impact of musical training in musicians' brain function, measured during the resting-state. The majority of the previous studies that have reported group differences in motor cortices of musicians in both structural and task-based functional data (see for example: Palomar-García, et al., 2017; Schlaug, 2015; Schlaug et al., 1995; Stewart, 2008), have recruited participants that play the same instrument professionally and have very similar levels of expertise. A critical limitation of the present study is the heterogeneity among participants in terms of years of experience (13.25 years ± 5.04) and a wide range of musical expertise (string instruments, percussions etc). This heterogeneity coupled with resting-state MEG recordings that were only 5-mins long probably make identification of seed-based differences difficult. Hence, this study focused on identifying global changes in the network configuration. However, it is plausible in a future study to introduce a task that engages both auditory and motor systems, which would likely make the differences more apparent.

To this end, a novel multilayer network framework to construct multi-frequency networks in a group of musicians and non-musicians was used. Furthermore, the properties of these networks using graph theoretical approaches were studied. As per the hypothesis, a modular organisation in musicians spanning the visuomotor regions and also the frontal and auditory parts of the brain was found. This modular organisation points to stronger inter-modular connectivity potentially underlying the integrated organisation observed in musicians. It must be noted here that single-layer analysis using NBS did not reveal this information. Furthermore, NBS has one critical limitation. It relies on choosing an arbitrary test statistic threshold. While it is the only parameter that needs to be manually set by the user, the results depend on the appropriate selection of the test statistic. In other words, different "statistically significant" networks can – (a) appear or – (b) disappear or – (c) change in topology with changes in the threshold. Plus, NBS also assumes that the users know *a priori* if the experimental effects are focal or distributed (i.e., the NBS parameters –

component extent and component intensity). The arbitrariness of this method and the fact that it only considers single-layer networks highlights the added value of the multilayer analysis.

The present study adds to the body of knowledge about brain reorganisation in highly-trained musicians, which was so far limited to structural MRI studies (for example (Schlaug et al., 1995; Amunts et al., 1997; Bangert & Schlaug, 2006), and task-based fMRI studies (e.g., Alluri et al., 2017; Grahn & Rowe, 2009). The question whether years of musical training would also be reflected in functional networks outside of task conditions – during resting-state – has only recently been addressed, in a single study so far (Klein et al. 2016). They reported an increased intra- and inter-hemispheric functional connectivity in resting-state EEG data of musicians in theta (6.5-8 Hz) and alpha1 (8.5-10 Hz) frequency bands. However, their investigation was limited to studying frequency-specific networks in isolation. This single-layer approach does not detect pan-spectral functional networks.

In addition to studying its modularity, the multilayer network framework also allows us to analyse between layer dependencies. When the brain is modelled as a multilayer network, the individual layers can act independently, in coherence of one another or at a transition point between these two extremes (Tewarie et al., 2016b). One important aspect of this between layer dependency is the correspondence between hubs in different layers. To probe this further, the DC between all combinations of the layers was estimated and compared between the two groups. The analysis revealed that musicians show a significantly different degree correlation compared to non-musicians, particularly in the theta-beta1 and alpha1-beta1 coupling.

The findings from DC underscore two important aspects of network organisation in musicians:

1) At a nodal level, musicians have less segregated clusters (lower modularity), thereby allowing for an integrated network organisation.

2) Between layers, a lower DC value for musicians was found, which points towards different layers functioning independently within the multilayer network, i.e., the hubs formed in the two layers are distinctly different from one another.

Taken together, musicians possess a highly integrated organization over the whole multi-frequency network, but the different layers retain, at the same time, their unique network structure. For example, classical musicians often need to read sheet music, encode the visual information (alpha band network) and translate it into signals to be executed by the motor cortex (beta band network). The between network coordination is not limited only to visuomotor areas, but has also been shown to span auditory, motor and other cognitive areas, which likely facilitates higher overall network integration (Jäncke, 2012; Proverbio et al., 2014). For instance, the coordination between auditory and motor areas is said to be mediated via the arcuate fasciculus (Catani et al., 2005; Catani & Mesulam, 2008). It is also plausible that this anatomical architecture underlies the auditory-motor coupling reported in musicians (Grahn & Rowe, 2009; Jäncke, 2012).

The critical difference observed in the results concerning between layer organization lies primarily in the theta-beta1 and alpha1-beta layers. The increased intra- and inter-hemispheric resting-state functional connectivity reported by (Klein et al., 2016), is also found in theta and alpha1 frequency bands. It is possible that the present results observed in lower frequency bands reflect long-range communication (Ward, 2003). Both theta and alpha band activity is involved in a wide range of cognitive functions (review: Başar et al., 2001; Ward, 2003) – such as memory and attention, which are highly active processes while playing an instrument (Schlaug, 2015).

The relationship between behavioural specialisation and changes in the underlying neuronal activity is not very straightforward (Zatorre et al., 2012). This problem is more pronounced when investigating spontaneous neuronal oscillations (using M/EEG), as both increases and decreases in activity can reflect a different brain state

(review: Baillet, 2017). There are several studies (e.g., Schneider et al., 2002; Shahin et al., 2003; Strait & Kraus, 2011, 2014) that have used evoked potentials to investigate musical specialisation. However, such evidence does not exist for resting-state data. A possible solution to circumvent this issue would be to conduct a longitudinal electrophysiological study to establish a clearer link between behaviour and increase or decrease in the underlying neuronal activity (using a similar approach as in the longitudinal structural imaging study by Draganski et al., 2004).

Brain dynamics occur across multiple spatial and temporal scales. Various neuroimaging techniques measure different aspects of the same underlying physiological processes, but these data sets are often analysed in isolation. However, the multilayer network framework has the potential to bridge this gap by taking a more integrative approach (De Domenico, 2017; Mandke et al., 2018). For example, the framework can be used to integrate data from MEG in different frequency ranges (as in the current study), from DTI and MEG or from fMRI and MEG in the same group of participants. Therefore, the multilayer network approach allows us to study in an individual how brain processes at different scales, from functional to structural, undergo plasticity-related changes. This study is one of the first demonstrations that an integrative approach is useful to study training-related brain plasticity.

The present study is not without limitations. Firstly, the data used here were part of the Open MEG Archive (Niso et al., 2016), which included a number of participants (8 out of 31 participants), who played an instrument for 5+ years but did not identify themselves as professional musicians. In addition, the participants who were professional musicians did not play the same instrument nor did they have similar years of experience (Mean: 13.25 years; SD: 5.04) playing an instrument. A future study could be designed to replicate these findings, with a more careful selection of participants to identify a clear relationship between resting-state network organisation and years of experience. Secondly, the MEG recordings in the present study were only 5 min in duration. The recording duration, an important aspect in capturing brain states in individual subjects (Liuzzi et al., 2017), should be carefully considered when designing future resting-state EEG or MEG studies.

Recently, in the context of speech, Assaneo & Poeppel (2018) provided evidence for the presence of an intrinsic rhythm – which mediates auditory-motor communication. It is conceivable that such a fine-tuned mechanism might also exist in musicians, mediating the communication between different areas and potentially leading to the formation of sub-networks or communities. This analysis needs to be probed further by studying the relationship between task-based data and task-free data in the same group of musicians.

7.4.1 Methodological considerations for multilayer networks (interlayer coupling)

In this work a frequency-based multilayer network was used, where, individual layers of the network were derived from individual MEG frequency bands that were identified a-priori. The intra-layer (within layer/band) communication was quantified using AEC and the inter-layer or cross-frequency (between layer/band) communication was set to one-to-one (or parameter *c*). Presently, there is no consensus in the network science community on the appropriate way of estimating interlayer coupling parameters and it suffers from some level of arbitrariness. This problem is further compounded by the fact that interlayer coupling between frequency-specific networks can be determined by many different metrics. For instance, the commonly described cross-frequency interactions as per (Jensen & Colgin, 2007) are – (a) power to power, (b) phase to phase, (c) phase to frequency, and (d) phase to power. There is mounting experimental evidence for the presence of phase to power or phase-amplitude coupling both in human and animal electrophysiology. Furthermore, Jensen & Colgin (2007), argue that gamma oscillations (>80 Hz) tend to couple strongly with the phase of the theta cycle (4-8 Hz), which has primarily been shown in intracranial data. A similar relationship has recently also been shown in resting-state MEG data (Florin & Baillet, 2015), however, the highest frequency band under consideration in the present work was 16.5-20 Hz and the lowest was 6.5-8 Hz, where such a cross-frequency relationship has not been

demonstrated before, making estimation of interlayer coupling a non-trivial problem. In a multilayer description, it is possible to include interlayer link weights derived from a separate measure of connectivity, such as, phase-amplitude coupling, but this will likely lead to inconsistent results and requires a careful methodological investigation, which is beyond the scope of present work. Moreover, the non-trivial problem of interlayer coupling is accentuated when considering multilayer network where individual layers are derived from different imaging modalities (for example, layer 1: fMRI network, layer 2: MEG network as in **Chapter 6**).

As problematic as the interlayer coupling is, De Domenico et al., (2016) argue that presence of such interlayer links allows us to take full advantage of tensorial algebra, allowing us to extend single-layer network metrics to multilayer networks. They also suggest that the choice of "*c*" should therefore depend on the choice of analysis. Moreover, as long as the value of "*c*" is kept constant between the groups under consideration, then the measure of degree (see **equation 5.10**) will scale linearly with c. Similarly, as modularity Q, depends linearly on H (H = *c*I, see **equation 5.17**), it follows that Q should also scale linearly with *c*. Lastly, as measures of between layer interactions (i.e., participation coefficient) are based on the quotient of two degrees (degrees scale linearly), these should be unaffected by values of *c*.

In the end, building on the work of De Domenico et al., (2016) and to maintain consistency between findings reported by (Guillon et al., 2017; Yu et al., 2017) the inter-layer coupling parameter was set to $\mathrm{H_{kl}} = \mathrm{cI}$. This can be thought of as a scaling parameter, which does not affect the results as long as it is kept constant for a given analysis.

7.4.2 Conclusion

An open-access dataset (OMEGA, Niso et al., 2016) was used to investigate the effects of training-related plasticity in resting-state MEG data. The frequency-specific networks were studied using NBS and by applying a novel multilayer network framework to construct multi-frequency networks in musicians and non-musicians.

The single-layer analysis did not reveal a statistically significant difference between the two groups. However, effects of musical training were detected in the modularity of the network, which spanned visuomotor and frontotemporal areas that have been shown to be involved in execution of a musical performance. The results also indicate that musicians show an integrated network organisation in comparison to non-musicians. DC results showed a significantly different layer-to-layer correspondence, potentially indicating that the formation of hubs in different layers is significantly different between the two groups. Presently, the study of training-related plasticity lacks an integrative approach and therefore neglects interactions between processes manifest in different MEG frequency bands and/or different modalities within individuals. To overcome this limitation, the use of the multilayer network framework is recommended.

CHAPTER 8

8 Concluding remarks and future directions

8.1 General discussion and future directions

8.1.1 MEG for cortical dynamics at multiple time scales

This thesis studied the dynamics of brain function at the millisecond's scale, during detection of oddballs, and at a scale of years, reflecting the development of skills through training. In the first experimental part of the project, cortical dynamics occurring over the millisecond time scale were investigated using MEG, a method with good spatial and temporal resolution as explained in **chapter 2**. To this end, auditory event-related responses were studied, specifically, the auditory P300 response to oddball tones which participants had to count (as rare targets within a series of standard tones of different sound frequency). To identify the neural sources of time-locked averages and to localise the sources of non-phase-locked responses (or ERS), LCMV and SAM beamformer were used, respectively. The two source localisation methods which were explained in detail in **chapter 3**. The neural sources of auditory N100m to standard tones were localised in the bilateral primary auditory cortices both as time-locked averages and ERS. Whereas, the neural sources of late, cognitive evoked responses to oddballs were localif sed in supra-modal areas. This is possible because the cognitive task demands additional sources, recruited from other areas. Naturally, the next question is, *are these processes and their neural substrates specific to audition or supra-modal?* One way to answer this question is to compare auditory with far less widely studied somatosensory P300. Among the few attempts to localise the sources of somatosensory P300, a MEG study of responses

to deviant (vs. standard) median nerve stimuli (applied to the wrist) is noteworthy (Huang et al., 2005). In their study, neural sources of target responses were found in inferior and parietal lobule/supra-marginal gyrus, anterior cingulate cortex and dorsolateral prefrontal cortex. These brain areas are partly shared with responses to auditory targets as observed in this thesis. However, their study used phase-locked averaging, which attenuates response components that vary from trial to trial, which has been demonstrated for auditory modality in this thesis (**chapter 4**). Therefore, it would be desirable to study time-locked averages and ERS to somatosensory oddballs, with the prediction (from the auditory P300 study) that oddballs activate parietal somatosensory cortex and also supra-modal areas.

The aim to study cortical dynamics over years required methods development as preparation for investigating the effect of sensorimotor training on resting-state network organisation. **Chapter 5** of the thesis introduced graph theory and multilayer network framework. A multilayer network, simply put, is a network of networks, where brain regions represent nodes in the network and layers of the network are individual networks derived from MEG frequency bands (or imaging modalities) that are interconnected. It allows us to capture both within- and between-network interactions. Such a complex interacting representation allows us to obtain a more realistic picture of the brain. In the case of integrating M/EEG frequency networks, the information about their interaction is embedded within the between-layer interactions. It has also been shown that multilayer networks show non-trivial properties that are not merely the result of the sum of its layers (De Domenico et al., 2013; Kivelä et al., 2014).

As for methods development, the main result of this thesis is that group comparisons using the multilayer network framework can be biased due to differences in average connectivity between groups. Therefore, accurate statistical inferencing requires some normalisation, which corrects for these biases. It must be noted that for weighted networks, the information is contained within the weights of the network and they do not simply indicate the presence or absence of connections. As a result, it proves to be challenging to differentiate between alterations in the underlying

ground truth that are due to an experimental manipulation or a disease process from those that are due to experimental choices. Such differentiation is of obvious importance to future applications of multilayer network analysis in studies of disease processes such as neurodegenerative disorders. To ameliorate this problem, the SVD based normalisation method was developed (**chapter 6**) which reduces biases in group comparisons, thereby controlling false positives and negatives. The efficacy of this method was assessed using synthetic data (known ground truth), and it was revealed that the SVD method proves to be superior to some existing approaches. Furthermore, several graph metrics were introduced, which can be utilised to quantify the topological organisation of the multilayer networks.

Finally, to investigate cortical dynamics over years, the newly developed methods were applied to the resting-state MEG data obtained from musicians and non-musicians (**chapter 7**), which was achieved by using the data released as part of the Open MEG Archive (Niso et al., 2016). Here, the musicians showed an integrated network configuration when compared with controls. While this study is the first one to investigate the multilayer network organisation in musicians and non-musicians, it had several limitations. First, as data were obtained from an open access repository, this did not allow for more stringent experimental control, i.e., selection of a more homogenous sample based on expertise and years of experience. Second, each participant's data recording was only 5-min long. It has been shown that longer recordings are required to capture brain states accurately in individual participants. Despite these obvious limitations, the study has made some unique contributions, i.e., the single-layer analysis of the same data (network-based statistics) failed to reveal any meaningful differences between groups. This is potentially because the interacting layers reveal additional information that individual layers cannot. This unique advantage of multilayer networks is particularly relevant for clinical studies, where often limited data are available (like in the present study with its limitation to 5-min recordings). By modelling the data as a multilayer network, we can potentially get to the heart of inherent complexities, embedded within the data.

In **chapter 7**, the effects of training-related plasticity were studied in MEG data only, with frequencies of MEG oscillations defining the layers of the network. Importantly, the multilayer network approach not only allows the integration of MEG layers but also data integration across imaging modalities. For example, layers representing the participant's functional data from other modalities (fMRI) and also structural data (DTI, structural covariance) into a common network representation. Such multimodal approaches are promising for future studies of training-related plasticity which will benefit from the unified network description. Furthermore, the thesis also provides a solution (i.e., agreement matrix) to evaluate multilayer community structure across layers (**see section 7.3.2.1**).

Thus, the thesis studied cortical dynamics at different scales – over milliseconds and over years. Among the outcomes, the new method for between-group comparisons of multilayer networks has significant potential for future use, as demonstrated in the study of network signatures of sensorimotor training. Beyond studying training-related plasticity, the most obvious application of the multilayer network framework is in the clinical domain, specifically to investigate neurodegenerative disorders. The following section proposes how this can be achieved.

8.1.2 Network neuroscience-based biomarkers

In the last three decades, various non-invasive neuroimaging methods have allowed us to improve our mechanistic understanding of the human brain functioning. However, these are rarely used as diagnostic or prognostic indicators. Even today, clinical diagnosis and management of various neurological and mental disorders depend on the subjective evaluation of symptomatology. For example, Alzheimer's Disease (AD) is characterised by irreversible neurodegeneration that can sometimes pre-date cognitive decline by more than a decade (Beason-Held et al., 2013). This underscores the need for early identification and intervention, which can have significant benefits for improving quality of life. Biomarkers from positron emission tomography (PET) have successfully been used in in the differential diagnosis of AD

(e.g., Marcus, Mena, & Subramaniam, 2014), however, they expose the individual to radiation. On the other hand, non-invasive imaging methods are completely radiation free. Early identification can be improved by the use of various non-invasive neuroimaging methods, however, so far these methods have had little clinical utility. Presently, the two major hurdles in the use of clinical neuroimaging are as follows:

1) Group averages

Due to the high scanning costs, the majority of the neuroimaging studies are limited in sample size and as a consequence, the results are often reported as group averages, which prevents scientists from identifying population-level trends (e.g., changes in brain connectivity across the life span). There are, however, good reasons behind performing a group comparison. The signal of interest measured using neuroimaging techniques is often very small and therefore, by studying group data one can achieve a considerable increase in signal to noise.

Statistically, the majority of the studies use general linear modelling (referred to as mass univariate analysis), as this allows scientists to identify statistically significant differences between groups. However, this approach is hardly useful in the context of individual patient reporting. Moreover, the studies that report disease-specific group difference show a large overlap with a healthy population, making its use in diagnostics impossible. This highlights a bigger problem, which is the lack of clear norms about what normal, healthy brain function looks like across the lifespan. Individualised data reporting is of paramount importance if neuroimaging methods are to become clinically relevant.

2) Lack of an integrative approach

Various brain imaging approaches, such as diffusion-weighted imaging (DWI), fMRI and MEG, offer complementary insights into brain structure and function. However, they are often studied in isolation, despite the accumulating evidence that they are interlinked in a non-trivial way (Hunt et al., 2016; Tewari et al., 2016). By using an integrative approach such as the multilayer network framework can allow us to

identify both linear and non-linear relationships between brain networks extracted from different imaging modalities.

Both these issues can be ameliorated by the use of network neuroscience-based approaches. The biggest advantage of graph theoretical approaches is that they are modality invariant, i.e., they can easily be used across a wide range of neuroimaging modalities. Plus, as it has been demonstrated in **chapters 5 and 6,** the multilayer network framework can be used to integrate data from different imaging modalities in a unified network description. Therefore, an ideal imaging or network neuroscience-based biomarker is the one that is highly sensitive to individual variability and highly specific to disease progression or pathophysiology. It also needs to be robust to the variability often introduced by imaging hardware and software.

By building on the recent advances in network neuroscience with various open-access databases (e.g., CamCAN, OMEGA etc), a normative database of brain connectivity can be established that paves the way for individual data reporting. A "normative" multimodal connectome database will allow for continuous measurement of brain connectivity (trajectories) across the lifespan. A normative database can have wide-ranging clinical applications (in various neurological or psychiatric conditions), we could measure whether deviations (distance from the norm in quartiles) from the norm predict cognitive-behavioural outcomes?

To this end, network neuroscience-based approaches are particularly well suited as one can derive individual scores of global and local network functioning, which can be compared against the norm (**Figure 8-1**). To study statistically low powered cohorts, such an approach with MEG source data has been suggested recently (Baillet, 2017), however, a norm-referenced testing (NRT) would be completely novel and facilitate individual data reporting.

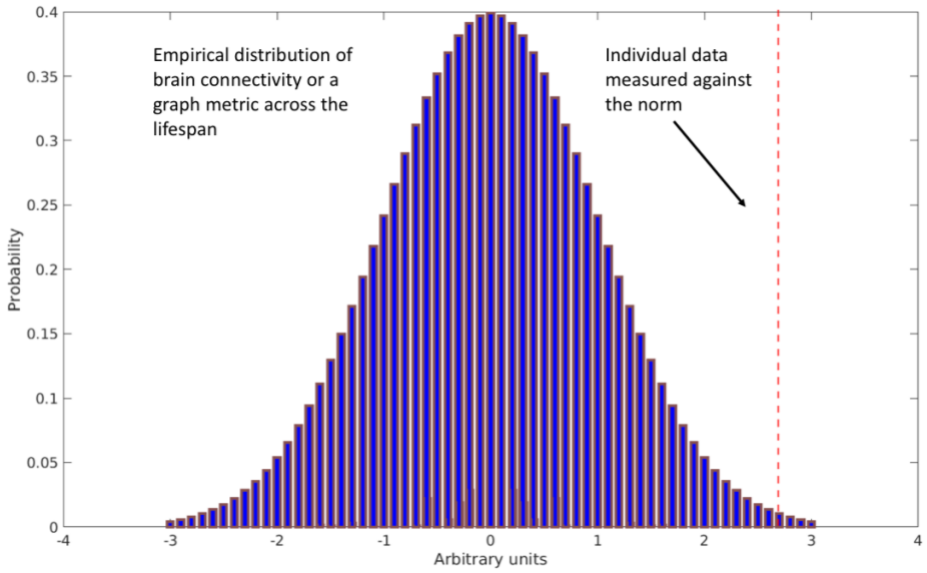


Figure 8-1 *Large open-access databases such as (OMEGA, Niso et al., 2016), (CamCAN, Taylor et al., 2017), (HCP, Van Essen et al., 2013)[3] can be used to establish a normative database of brain connectivity. Such an empirical database or distribution of a quantitative metric can be used to assess an individual or groups of subjects and whether they deviate from the norm. Figure adapted from Baillet (2017).*

NRT based assessment is a type of evaluation which provides an estimate of an individual's trait being measured in a pre-defined empirical distribution. NRT based assessment is regularly used for the Graduate Record Examination (GRE) or for various IQ tests.

For example, in typical IQ tests, a median IQ is defined from a population and new individuals are ranked above or below that value. In the context of neuroimaging, the trait being measured could be for example, average connectivity, degree correlation, clustering coefficient etc. This type of assessment only provides a measure of whether the given individual's data are above or below relative to the population norm. Identifying how an individual patient fares against the norm can potentially prove to be a useful diagnostic or prognostic indicator.

3 *OMEGA: Open MEG Archive, CamCAN: Cambridge Centre for Ageing Neuroscience, HCP: Human Connectome Project*

In conclusion, by exploiting the superior temporal resolution of MEG, this work has investigated cortical dynamics occurring at the two ends of the temporal scale. The tools used in investigating cortical dynamics over years in particular, i.e., the use of a network framework in systems neuroscience is still in its infancy. The chief contributions of this thesis are the application of graph metrics to quantify multilayer networks, the development of a method for group comparisons, and finally demonstrating that multilayer networks provide additional information that single-layer approaches (i.e., network-based statistics) cannot. Throughout this thesis, multilayer networks with one-to-one coupling were used, therefore, the next obvious challenge is to identify the best methods of estimating between layer weights. However, then the open question remains, *at what point does any additional information in a fully connected block-adjacency matrix becomes redundant?*

Finally, the multilayer networks offer a static snapshot of the brain function. It is worth noting that the recent work on dynamic connectivity has shown that brain networks rapidly form and dissolve over much smaller timescales (O'Neill et al., 2018; Vidaurre et al., 2017, 2016). Therefore, further work is needed to investigate how multilayer network topology evolves over time, which can potentially be achieved by studying longitudinal data obtained from a small group of subjects (dense sampling, e.g., midnight scanning club, Gordon et al., 2017).

By studying the human brain as a network, we have begun to uncover its astonishing complexity. In the years to come, I am confident that our understanding of healthy brain functioning and its breakdown in disease will only continue to grow.

9 Appendix

Table 9-1 *Complete list of nodes in the AAL atlas.*

1	Rectus_L	40	Rectus_R
2	Olfactory_L	41	Olfactory_R
3	Frontal_Sup_Orb_L	42	Frontal_Sup_Orb_R
4	Frontal_Med_Orb_L	43	Frontal_Med_Orb_R
5	Frontal_Mid_Orb_L	44	Frontal_Mid_Orb_R
6	Frontal_Inf_Orb_L	45	Frontal_Inf_Orb_R
7	Frontal_Sup_L	46	Frontal_Sup_R
8	Frontal_Mid_L	47	Frontal_Mid_R
9	Frontal_Inf_Oper_L	48	Frontal_Inf_Oper_R
10	Frontal_Inf_Tri_L	49	Frontal_Inf_Tri_R
11	Frontal_Sup_Medial_L	50	Frontal_Sup_Medial_R
12	Supp_Motor_Area_L	51	Supp_Motor_Area_R
13	Paracentral_Lobule_L	52	Paracentral_Lobule_R
14	Precentral_L	53	Precentral_R
15	Rolandic_Oper_L	54	Rolandic_Oper_R
16	Postcentral_L	55	Postcentral_R
17	Parietal_Sup_L	56	Parietal_Sup_R
18	Parietal_Inf_L	57	Parietal_Inf_R
19	SupraMarginal_L	58	SupraMarginal_R
20	Angular_L	59	Angular_R
21	Precuneus_L	60	Precuneus_R
22	Occipital_Sup_L	61	Occipital_Sup_R
23	Occipital_Mid_L	62	Occipital_Mid_R
24	Occipital_Inf_L	63	Occipital_Inf_R
25	Calcarine_L	64	Calcarine_R
26	Cuneus_L	65	Cuneus_R
27	Lingual_L	66	Lingual_R
28	Fusiform_L	67	Fusiform_R
29	Heschl_L	68	Heschl_R
30	Temporal_Sup_L	69	Temporal_Sup_R
31	Temporal_Mid_L	70	Temporal_Mid_R
32	Temporal_Inf_L	71	Temporal_Inf_R

33	Temporal_Pole_Sup_L	72	Temporal_Pole_Sup_R
34	Temporal_Pole_Mid_L	73	Temporal_Pole_Mid_R
35	ParaHippocampal_L	74	ParaHippocampal_R
36	Cingulum_Ant_L	75	Cingulum_Ant_R
37	Cingulum_Mid_L	76	Cingulum_Mid_R
38	Cingulum_Post_L	77	Cingulum_Post_R
39	Insula_L	78	Insula_R

9.1 Appendix to chapter 7 – Degree correlations

In **chapter 7**, to investigate the correspondence between the hubs of different layers of the multilayer network, we computed degree correlations. DC can be derived by calculating a Pearson correlation coefficient between degree sequences of different layers. We calculated DC between all combinations of layers. **Section 7.3.2.2** shows DC results that were statistically significant between musicians and non-musicians. This section provides remaining results of DC. For all the box and whisker plots below, the top and bottom of each box represents 25th and 75th percentile respectively (also defining the interquartile range), and the red line in the middle shows the median of that sample. Whiskers extend from the ends of the interquartile range to the furthest non-outlier observation. Outliers (red dots) are defined as values above or below 1.5 times the interquartile range, measured from top or bottom of the box. Layers 1 to 5 of the multilayer network are as follows –

Layer 1: theta (6.5-8 Hz), Layer 2: alpha1 (8.5-10 Hz), Layer 3: alpha2 (10.5-12 Hz), Layer 4: beta1 (12.5-16 Hz), Layer 5: beta2 (16.5-20 Hz)

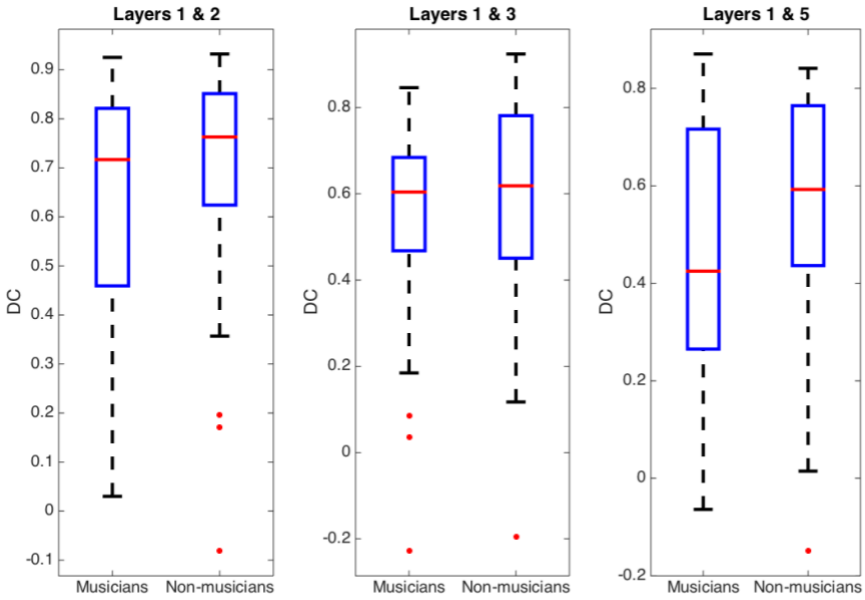


Figure 9-1 *Boxplots of degree correlations.* ***Left panel*** *shows DC between theta layer (layer 1) and alpha1 layer (layer 2) (p=0.31, Wilcoxon rank-sum test).* ***Middle panel*** *shows DC between theta layer (layer 1) and alpha2 layer (layer 3) (p=0.27, Wilcoxon rank-sum test).* ***Right panel*** *DC between theta layer (layer 1) and beta2 layer (layer 5) (p=0.17).*

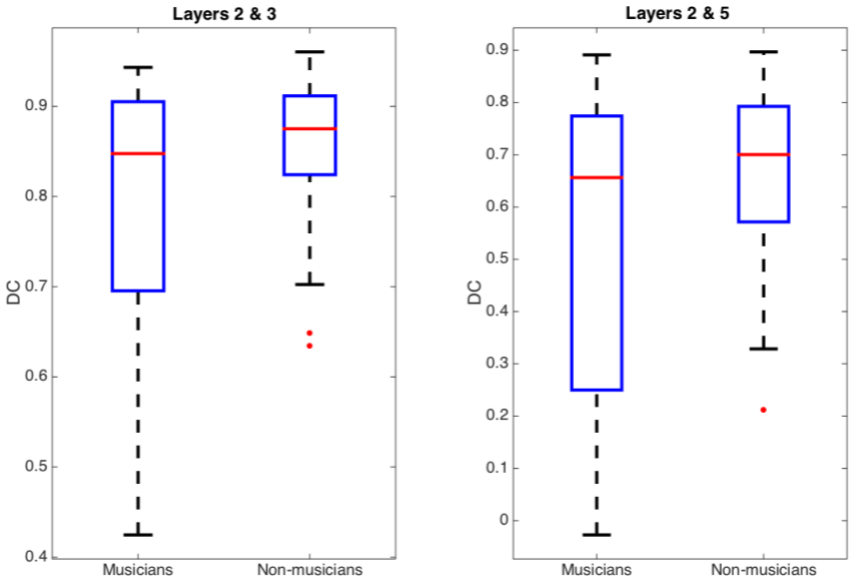


Figure 9-2 *Boxplots of degree correlations.* ***Left panel*** *shows DC between alpha1 layer (layer 2) and alpha2 (layer 3) (p=0.23, Wilcoxon rank-sum test).* ***Right panel*** *shows DC between alpha1 layer (layer 2) and beta2 layer (layer 5) (p=0.15, Wilcoxon rank-sum test).*

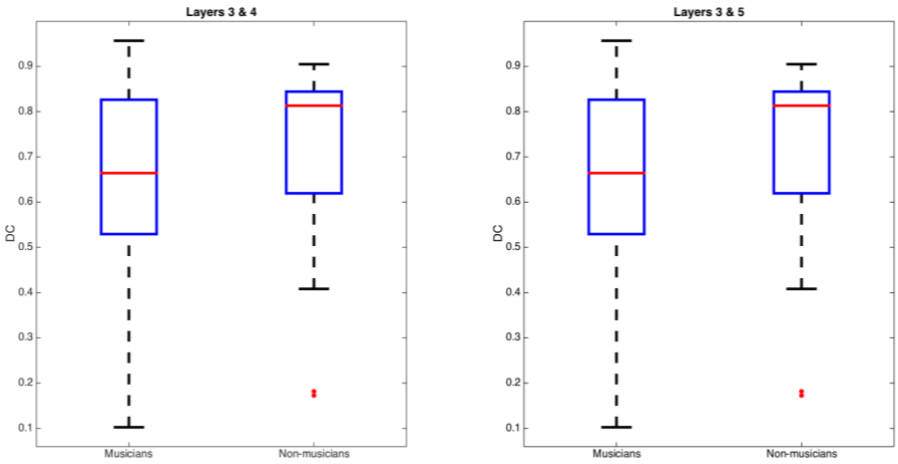


Figure 9-3 *Boxplots of degree correlations.* ***Left panel*** *shows DC between alpha2 layer (layer 3) and beta1 layer (layer 4) (p=0.14, Wilcoxon rank-sum test).* ***Right panel*** *shows DC between alpha2 layer (layer 3) and beta2 layer (layer 5) (p=0.14, Wilcoxon rank-sum test).*

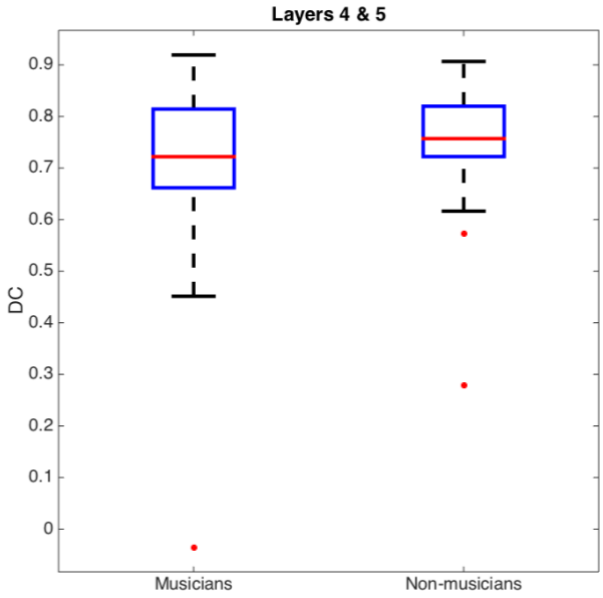


Figure 9-4 *Boxplot of degree correlations between beta1 layer (layer 4) and beta2 layer (layer 5) (p=0.24, Wilcoxon rank-sum test).*

LIST OF FIGURES

Figure 1-1 Exponential growth in the number of scientific publications in neurosciences over the decades. 2

Figure 1-2 Spatiotemporal scales of various neuroscientific methods. The X-axis shows the spatial scale and Y-axis shows the temporal scale. In this thesis, brain dynamics at two ends of the temporal spectrum were investigated using MEG. These are the two points where the horizontal dotted line intersects with the two vertical dotted lines. As an example of cortical dynamics over milliseconds, auditory evoked responses were studied. The study of cortical dynamics over years was achieved by studying group differences in MEG resting-state data. The inset shows the availability of neuroscientific methods in the year 1988. Figure adapted from Sejnowski et al. (2014). 4

Figure 2-1 A schematic of a pyramidal neuron. The image is taken from Hämäläinen et al. (1993). . 10

Figure 2-2 Schematic representation of a typical neuron. Image extracted and adapted from https://en.wikipedia.org/wiki/Myelin#/media/File:Neuron_Hand-tuned.svg (creative commons). 11

Figure 2-3 Laminar organisation of the cortex from layer I to layer VI. Various staining methods reveal different cell types. Figure from Kandel, Schwartz, and Jessell (2000) 12

Figure 2-4 A schematic representation of postsynaptic current flowing along a dendrite. The primary current is the direct result of an influx of ions. The secondary currents or volume currents are a result of electric fields generated as ions are released. 17

Figure 2-5 The example shows a simple dipole in the temporal region producing magnetic fields as measured using MEG and electric fields as measured using EEG. It can be noted that the magnetic field patterns are orthogonal to the electric fields and can be explained using the right-hand rule. The image is taken from Hari and Puce (2017). 18

Figure 2-6 The very first traces of alpha rhythm recorded using a superconducting magnetometer from the occiput of a healthy subject. The modulation of alpha activity on the opening and closing of the eyes can be seen in both electrical and magnetic traces. Image from Cohen (1972). 20

Figure 2-7 An example of event-related responses to auditory stimulation recorded using MEG, showing positive (P50) and negative peaks (N100). Auditory stimuli were pure tones (frequency: 1000Hz, duration: 100ms), which were presented at a regular interval of 1.5sec. For the purpose of illustration, the traces were averaged in MEG sensor space across 10 subjects. The three traces represent different sensors. X-axis: Time in seconds, Y-axis: Amplitude in fT.... 22

Figure 2-8 (A) Schematic of a typical MEG scanner (Figure from Vrba & Robinson, 2001) **(B)** Various sources of magnetic interference and their corresponding field strengths. It is worth noting that both biological and environmental sources of interference are several magnitudes higher than the activity of the brain (the alpha rhythm for reference). This figure demonstrates the need for effective shielding strategies. The figure is taken from Hämäläinen et al. (1993). 24

Figure 2-9 The voltage (V), in the SQUID sensor is a sinusoidal function of magnetic flux (ϕ). The sensor is kept in its optimum working area by a feedback loop. Figure adapted from Hari and Puce (2017). 26

Figure 2-10 Three commonly used configurations of MEG pick up coils. CTF-MEG system used in this thesis uses the axial gradiometer configuration. 26

Figure 2-11 An illustration showing the effect of first-order gradiometers. Due to the baseline distance, the interfering noise is attenuated. Baseline distance = r_2-r_1, X-axis: Distance, Y-axis: Magnetic field (B) 28

Figure 3-1 Relationship between the forward and the inverse problem. The **left panel** shows orientation and the field patterns of the dipoles (i.e., recorded data) and the **right panel** shows the location of the two dipoles in source space (i.e., estimated current distribution). 31

Figure 3-2 Illustration of beamforming. To estimate the virtual electrode (VE) output, the signal at a region of interest is reconstructed as a weighted sum of the MEG sensors (shown for a 151-channel system; the CTF system used in the thesis has 275 channels). The weights are assigned such that signal from the region of interest is maximised, while attenuating sources of noise from other regions. This step is sequentially run for every region in the brain (resulting in a VE output for each of the pre-defined grid points. VE is the same as $\boldsymbol{q}\theta(t)$ in equation 3.2). Figure from Hillebrand and Barnes, (2005). 34

Figure 4-1 The schematic shows the estimation of an averaged virtual electrode output using an event-related beamformer for a given location in the brain. Figure adapted from Cheyne et al. (2006). 46

Figure 4-2 Plot D and E show sensor space grand averages (N=10 participants) of standard and deviant tones (100 trials each). Plots A-C show field topography for standard tones and plots F-H show field topography for deviant tones. The shaded box in panels D and E shows the P300 time window. The colour bar ranges between -150 fT (blue) to +150 fT (red). L: Left, R: Right 48

Figure 4-3 Plots A-F show group results (N=10 participants) of cluster permutations testing (sensor x time) plotted on sensor layouts at corresponding time stamps. The plots show statistically significant activity between standard and deviant condition, with red colour corresponding to positive t-values (deviant > standard). L: Left, R: Right 49

Figure 4-4 Group results (N=10 participants) of SAM analysis showing statistically significant ($p<0.05$, FDR-corrected), regions of ERS to standard tones (plot **C**). Plot **A** and **B** show reconstructed

virtual electrode (VE) output from the peak voxel in the superior temporal region in the left and right hemisphere respectively (shaded area showing SD). The results were obtained by contrasting post-stimulus window (0-200ms) against a pre-stimulus window (-200-0ms) of the standard tones. Plot **D** and **E** showcase averaged spectrograms obtained after transforming the individual VE output in time-frequency domain using Hilbert transform. 50

Figure 4-5 *Group results of the event-related beamformer analysis showing statistically significant regions (p<0.05, FDR-corrected) to standard tones (plot **C**). Plot **A** and **B** show reconstructed virtual electrode (VE) output from the peak voxel in the superior temporal region in the left and right hemisphere respectively (shaded area showing SD). The results were obtained by contrasting averaged post-stimulus window (0-200ms) against a pre-stimulus window (-200-0ms) of the standard tones. Plot **D** and **E** showcase averaged spectrograms obtained after transforming the individual VE output in time-frequency domain using Hilbert transform.* 52

Figure 4-6 Results of SAM analysis showing statistically significant (p<0.05, FWE-corrected), regions of ERS in theta band (4-8Hz) for deviant tones, in frontal and prefrontal regions (plot C). Plot **A** and **B** show reconstructed virtual electrode (VE) output from the peak voxel in the bilateral inferior frontal gyri (shaded area showing SD). The results were obtained by contrasting post-stimulus window (300-700ms) of deviant tones against the post-stimulus window (300-700ms) of standard tones. The group activity maps (N=10 participants) have been overlaid on the template brain. Plot **D** and **E** showcase averaged spectrograms obtained after transforming the individual VE output in the time-frequency domain using Hilbert transform. 53

Figure 4-7 Group results of the event-related beamformer analysis showing statistically significant (p<0.05, FDR-corrected) to deviant tones (plot **C**). Plot **A** and **B** show reconstructed virtual electrode (VE) output from the peak voxel in the prefrontal cortex in the left and right hemisphere respectively. The results were obtained by contrasting averaged post-stimulus window of deviant tones (300-700ms) against a post-stimulus window of standard tones (300-700ms). Plot **D** and **E** showcase spectrograms obtained after transforming the VE output in the time-frequency domain using Hilbert transform..... 55

Figure 5-1 Building blocks of graphs. A: node or vertex, B: a simple graph showing the presence of an edge or link between the two nodes, C: degree: number of connections incident on a given node (node j has a degree of 2), path length: distance from node i to node k (2); D: undirected, unweighted graph; E: undirected, weighted graph (weights correspond to the thickness of lines); F: directed, weighted graph. 68

Figure 5-2 Schematic representation of a typical analysis pipeline used in graph-theoretical analysis of brain imaging data. Based on anatomical scans. the brain is parcellated into regions (here 78 regions based on AAL atlas). For each of the 78 regions, activity time courses are obtained (in the case of MEG: amplitude envelopes for 2 out of 78-time courses shown). 78 x 78

connectivity values are computed, displayed here (a) in adjacency matrix where each of 78 x 78 node is coloured according to connection strength (red: strongest connections) and (b) as network representation where 78 regions are ordered in a circular plot and connections are shown as connecting lines. The network is then evaluated using various graph metrics. 70

Figure 6-1 A schematic of the analysis pipeline including the construction of MEG specific multilayer network and a multimodal (fMRI-MEG) multilayer network. Note that a special case of multilayer networks is used here: multilayer networks with one-to-one between layer coupling. rs: Resting-state, fc: Functional connectivity 95

Figure 6-2 The plot shown here is the eigen spectrum of a MEG multilayer network used in this chapter (see **6.4.1**, layer 1: alpha band, layer 2: beta band). We normalise the adjacency matrix by its largest eigenvalue also known as the spectral radius of the graph. 100

Figure 6-3 Metrics are affected by changes in link density (A) and average connectivity (B). The plots show that tuning arbitrary link density (i.e., an arbitrary threshold), or the average connectivity, affects most of the metrics. However, this was not the case for DC and PC for changes in average connectivity. ρ = link density, DC: degree correlation, X: functional multilayer page rank, PC: participation coefficient, Q: multilayer modularity, <FC>: average functional connectivity. The solid line and shaded areas show the mean and standard deviation across subjects, respectively..... 101

Figure 6-4 The multilayer network made from participants' alpha and beta band networks. A) MST correction scheme on the multilayer network. This may result in a network that is connected but with disconnected individual layers, denoted by the multiple red dots and illustrated in (B). ECO correction scheme on the multilayer network (A). This can also lead to disconnected networks denoted by multiple green dots. C) SVD correction scheme on the whole multilayer network. D) Effective graph resistance cost minimisation. The solid line and shaded areas show the mean and standard deviation across subjects, respectively. ρ = density, <FC>: average functional connectivity, DC: degree correlation, X: functional multilayer page rank, PC: participation coefficient, Q: multilayer modularity, F: effective graph resistance cost minimisation. 103

Figure 6-5 The multilayer network made from participants' beta band MEG and fMRI networks. A) MST and ECO correction schemes applied to the individual layers. B) SVD correction scheme applied to individual layers. CD) Effective graph resistance cost minimisation in the two layers. The solid line and shaded areas show the mean and standard deviation across subjects, respectively. ρ = density, <FC>: functional connectivity, DC: degree correlation, X: functional multilayer page rank, PC: participation coefficient, Q: community structure, F: effective graph resistance cost minimisation. 105

Figure 6-6 Community assignment of multilayer networks (alpha and beta band) after applying correction schemes. Nodes that have the same colour belong to the same community (shown for the first layer here). On the outmost left, the original community assignment for every node is shown and further to the right the assignment after applying correction schemes is visualized. Only SVD applied to the whole multilayer (SVD_m) and on the individual layers (SVD_i) can correctly identify the communities. ECO and MST applied to the individual layers distort community assignments of nodes. 106

Figure 6-7 1st row: sensitivity of network metrics to changes in network organisation of the (synthetic) multilayer networks before and after applying SVD. A) Synthetic modular multilayer networks: modularity (Q) as a function of between layer dependency on the ground truth (blue) and SVD corrected networks (red). B) Synthetic scale free multilayer networks: degree correlation (DC) as a function of between layer dependency on the ground truth (blue) and SVD corrected networks (red) (both are completely overlapping). C) Correlation between Q as obtained before and after SVD. D) Correlation between DC as obtained before and after SVD. 2nd row: sensitivity of network metrics to changes in network organisation of the (empirical) multilayer networks. E) Q as a function of rewiring probability (P) for original networks (blue) and SVD corrected networks (red). F) Degree correlation (DC) as a function of rewiring probability for original networks and SVD corrected networks. G) Correlation between Q as obtained before and after SVD. H) Correlation between DC as obtained before and after SVD. The shaded areas in A and B show the mean and standard deviation across realisations (A, B) or subjects (E, F). m in panels CDGH is the slope of the regression line. 108

Figure 6-8 Sensitivity of metrics to changes in network organisation of the (synthetic) multilayer networks. Synthetic modular multilayer networks: Community (Q) as a function of between layer dependency on the ground truth and on corrected networks (A). Synthetic scale free multilayer networks: degree correlation (DC) as a function of between layer dependency on the ground truth and corrected networks (B). Correlation between modularity as obtained before and after correction schemes (C). Correlation DC as obtained before and after correction schemes (D). Sensitivity of the solutions to changes in network organisation of the (empirical) multilayer networks. Empirical multilayer networks: Community (Q) as a function of rewiring probability (P) for original networks (black) and corrected networks (E). Empirical multilayer networks: degree correlation (DC) as a function of rewiring probability (P) for original networks (black) and corrected networks (F). Correlation between modularity as obtained before and after correction schemes (G). Correlation of DC as obtained before and after correction schemes (H). The shaded areas show the mean and standard deviation across realisations (A-B) or subjects (E-F). 110

Figure 6-9 Distributions of Q for two groups. Group differences of multilayer network community structure for the ground truth (black), SVD approach (blue), MST (red), and ECO (green). Both whole multilayer network correction, as well as individual layer correction, are applied for SVD; the former is denoted as SVD_m and the latter as SVDi. A and B refer to two different conditions: I) a different number of random links for the two sets; II) different between layer dependency for the two sets. 112

Figure 7-1 A schematic of the analysis pipeline used in the construction of multilayer networks. Here, a special case of the multilayer networks is used: multilayer networks with one-to-one between layer coupling. rs: Resting-state, AEC: Amplitude envelope correlations. Theta: 6.5-8Hz, Alpha1: 8.5-10Hz, Alpha2: 10.5-12Hz, Beta1: 12.5-16Hz, Beta2: 16.5-20Hz..... 130

Figure 7-2 Averaged AEC in adjacency matrix (78 brain area labels on each axis: 1-39 left hemisphere, 40-78 right hemisphere) across musicians (A' to E') and its corresponding source space (top 40% of the connections) representation (3D plots, A to E) in the 5 frequency bands under consideration. All adjacency matrices show typical patterns of high-AEC within left hemisphere (upper left quadrant), within right hemisphere (lower right quadrant) and between hemispheres (upper right quadrant). In the 3D plots, lines indicate presence of connections, with thicker lines corresponding to stronger connections. The circles in the 3D plots indicate summed magnitude of link weights (node strength, weighted degree) between the node and rest of the brain. 134

Figure 7-3 Averaged AEC plotted as adjacency matrices across non-musicians (A' to E') and their corresponding source space (top 40% of the strongest connections) representation (3D plots, A to E) in 5 frequency bands under consideration. In the 3D plots, lines indicate the presence of connections, with thicker lines corresponding to stronger connections. The circles in the 3D plots indicate the summed magnitude of link weights (node strength, weighted degree) between the node and rest of the brain..... 135

Figure 7-4 Boxplots of modularity (Q) for the two groups. This difference was found to be statistically significant (p=0.033 Wilcoxon rank-sum test). The top and bottom of each box represent 25th and 75th percentile respectively (also defining the interquartile range), and the red line in the middle shows the median of that sample. Whiskers extend from the ends of the interquartile range to the furthest non-outlier observation. Outliers (red dots) are defined as values above or below 1.5 times the interquartile range, measured from top or bottom of the box. 136

Figure 7-5 Schematic representation of collapsed agreement matrix computed for both groups. The collapsed agreement matrices were subjected to community detection algorithm. The community assignment was subsequently plotted in brain space to reveal group-level representation. Identical colours belong to the same community. 137

Figure 7-6 Boxplots of degree correlations. Only the layer pairs that showed significant differences are plotted. The Left panel shows significantly different DC between theta layer (layer 1) and beta1 layer (layer 4) (p=0.045, Wilcoxon rank-sum test). Right panel shows significantly different DC between layer 2 (alpha1) and layer 4 (beta1), (p=0.031, Wilcoxon rank-sum test). Box- and whisker plots as in (**Figure 7-4**)..... 138

Figure 8-1 Large open-access databases such as (OMEGA, Niso et al., 2016), (CamCAN, Taylor et al., 2017), (HCP, Van Essen et al., 2013) can be used to establish a normative database of brain connectivity. Such an empirical database or distribution of a quantitative metric can be used to assess an individual or groups of subjects and whether they deviate from the norm. Figure adapted from Baillet (2017)..... 152

Figure 9-1 Boxplots of degree correlations. **Left panel** shows DC between theta layer (layer 1) and alpha1 layer (layer 2) (p=0.31, Wilcoxon rank-sum test). **Middle panel** shows DC between theta layer (layer 1) and alpha2 layer (layer 3) (p=0.27, Wilcoxon rank-sum test). **Right panel** DC between theta layer (layer 1) and beta2 layer (layer 5) (p=0.17)..... 157

Figure 9-2 Boxplots of degree correlations. **Left panel** shows DC between alpha1 layer (layer 2) and alpha2 (layer 3) (p=0.23, Wilcoxon rank-sum test). **Right panel** shows DC between alpha1 layer (layer 2) and beta2 layer (layer 5) (p=0.15, Wilcoxon rank-sum test)..... 158

Figure 9-3 Boxplots of degree correlations. **Left panel** shows DC between alpha2 layer (layer 3) and beta1 layer (layer 4) (p=0.14, Wilcoxon rank-sum test). **Right panel** shows DC between alpha2 layer (layer 3) and beta2 layer (layer 5) (p=0.14, Wilcoxon rank-sum test)..... 158

Figure 9-4 Boxplot of degree correlations between beta1 layer (layer 4) and beta2 layer (layer 5) (p=0.24, Wilcoxon rank-sum test)..... 159

LIST OF TABLES

Table 2-1 Summary of human electrophysiological frequency bands..... 21

Table 4-1 Anatomical locations of peak clusters (p<0.05, FDR-corrected) found using SAM-SnPM analysis (N100 time window: 0-200ms)..... 51

Table 4-2 Anatomical locations of peak clusters (p<0.05, FDR-corrected) found using event-related beamformer (N100m). 52

Table 4-3 Anatomical locations of peak clusters (p<0.05, FDR-corrected) found using SAM-SnPM analysis (P300). 54

Table 4-4 Anatomical locations of peak clusters (p<0.05, FDR-corrected) found using event-related beamforming (P300). 56

Table 7-1 Summary of statistics for both groups 125

Table 9-1 Complete list of nodes in the AAL atlas. 154

REFERENCES

Adjamian, P., Hadjipapas, A., Barnes, G. R., Hillebrand, A., & Holliday, I. E. (2008). Induced gamma activity in primary visual cortex is related to luminance and not color contrast: An MEG study. *Journal of Vision*, *8*(2008), 1–7. https://doi.org/10.1167/8.7.4

Adjamian, P., Holliday, I. E., Barnes, G. R., Hillebrand, A., Hadjipapas, A., & Singh, K. D. (2004). Induced visual illusions and gamma oscillations in human primary visual cortex. *European Journal of Neuroscience*, *20*(2), 587–592. https://doi.org/10.1111/j.1460-9568.2004.03495.x

Alluri, V., Toiviainen, P., Burunat, I., Kliuchko, M., Vuust, P., & Brattico, E. (2017). Connectivity patterns during music listening: Evidence for action-based processing in musicians. *Human Brain Mapping*, *38*(6), 2955–2970. https://doi.org/10.1002/hbm.23565

Amunts, K., Schlaug, G., Jäncke, L., Steinmetz, H., Schleicher, A., Dabringhaus, A., & Zilles, K. (1997). Motor cortex and hand motor skills: Structural compliance in the human brain. *Human Brain Mapping*, *5*(3), 206–215. https://doi.org/10.1002/(SICI)1097-0193(1997)5:3<206::AID-HBM5>3.0.CO;2-7

Ashburner, J., Andersson, J. L. R., & Friston, K. J. (1999). High-dimensional image registration using symmetric priors. *NeuroImage*, *9*(6), 619–628. https://doi.org/10.1006/nimg.1999.0437

Ashburner, J., & Friston, K. J. (2005). Unified segmentation. *NeuroImage*, *26*(3), 839–851. https://doi.org/10.1016/j.neuroimage.2005.02.018

Assaneo, M. F., & Poeppel, D. (2018). The coupling between auditory and motor cortices is rate-restricted : Evidence for an intrinsic speech-motor rhythm. *Science Advances*, 1–10. https://doi.org/10.1126/sciadv.aao3842

Baillet, S. (2017). Magnetoencephalography for brain electrophysiology and imaging. *Nature Neuroscience*, *20*(3), 327–339. https://doi.org/10.1038/nn.4504

Baillet, S., Mosher, J. C., & Leahy, R. M. (2001). Electromagnetic brain mapping. *IEEE Signal Processing Magazine*, *18*(6), 14–30. https://doi.org/10.1109/79.962275

Baker, S. N. (2007). Oscillatory interactions between sensorimotor cortex and the periphery. *Current Opinion in Neurobiology*, *17*(6), 649–655. https://doi.org/10.1016/j.conb.2008.01.007

Bangert, M., & Schlaug, G. (2006). Specialization of the specialized in features of external

human brain morphology. *European Journal of Neuroscience*, *24*(6), 1832–1834. https://doi.org/10.1111/j.1460-9568.2006.05031.x

Barnes, G. R., Furlong, P. L., Singh, K. D., & Hillebrand, A. (2006). A verifiable solution to the MEG inverse problem. *NeuroImage*, *31*(2), 623–626. https://doi.org/10.1016/j.neuroimage.2005.12.036

Barnes, G. R., Hillebrand, A., Fawcett, I. P., & Singh, K. D. (2004). Realistic spatial sampling for MEG beamformer images. *Human Brain Mapping*, *23*(2), 120–127. https://doi.org/10.1002/hbm.20047

Başar-Eroglu, C., Başar, E., Demiralp, T., & Schürmann, M. (1992). P300-response: possible psychophysiological correlates in delta and theta frequency channels. A review. *International Journal of Psychophysiology*, *13*(2), 161–179. https://doi.org/10.1016/0167-8760(92)90055-g

Başar, E., Başar-Eroglu, C., Karakaş, S., & Schürmann, M. (2001). Gamma, alpha, delta, and theta oscillations govern cognitive processes. *International Journal of Psychophysiology*, *39*(2–3), 241–248. https://doi.org/10.1016/s0167-8760(00)00145-8

Başar, E., Schürmann, M., Başar-Eroglu, C., & Karakaş, S. (1997). Alpha oscillations in brain functioning: An integrative theory. *International Journal of Psychophysiology*, *26*(1–3), 5–29. https://doi.org/10.1016/s0167-8760(97)00753-8

Bassett, D. S., & Bullmore, E. T. (2006). Small-world brain networks. *Neuroscientist*, *12*(6), 512–523. https://doi.org/10.1177/1073858406293182

Bassett, D. S., Bullmore, E. T., Verchinski, B. A., Mattay, V. S., Weinberger, D. R., & Meyer-Lindenberg, A. (2008). Hierarchical Organization of Human Cortical Networks in Health and Schizophrenia. *Journal of Neuroscience*, *28*(37), 9239–9248. https://doi.org/10.1523/JNEUROSCI.1929-08.2008

Bassett, D. S., Porter, M. A., Wymbs, N. F., Grafton, S. T., Carlson, J. M., & Mucha, P. J. (2013). Robust detection of dynamic community structure in networks. *Chaos*, *23*(1), 013142–16. https://doi.org/10.1063/1.4790830

Bassett, D. S., & Sporns, O. (2017). Network neuroscience. *Nature Neuroscience*, *20*(3), 353–364. https://doi.org/10.1038/nn.4502

Bassett, D. S., Wymbs, N. F., Porter, M. A., Mucha, P. J., Carlson, J. M., & Grafton, S. T. (2010). Dynamic reconfiguration of human brain networks during learning. *Proceedings of the National Academy of Sciences*, *108*(18), 7641–7646. https://doi.org/10.1073/pnas.1018985108

Bastos, A. M., & Schoffelen, J.-M. (2016). A tutorial review of functional connectivity analysis methods and their interpretational pitfalls. *Frontiers in Systems Neuroscience*, *9*, 1–23. https://doi.org/10.3389/fnsys.2015.00175

Battiston, F., Nicosia, V., Chavez, M., & Latora, V. (2017). Multilayer motif analysis of brain networks. *Chaos*, *27*(4), 047404–047408. https://doi.org/10.1063/1.4979282

Battiston, F., Nicosia, V., & Latora, V. (2014). Structural measures for multiplex networks. *Physical Review E - Statistical, Nonlinear, and Soft Matter Physics*, *89*(3), 1–14. https://doi.org/10.1103/PhysRevE.89.032804

Bauer, M., Kennett, S., & Driver, J. (2012). Attentional selection of location and modality in vision and touch modulates low-frequency activity in associated sensory cortices. *Journal of Neurophysiology*, *107*(9), 2342–2351. https://doi.org/10.1152/jn.00973.2011

Baum, G. L., Ciric, R., Roalf, D. R., Betzel, R. F., Moore, T. M., Shinohara, R. T., … Satterthwaite, T. D. (2017). Modular segregation of structural brain networks supports the development of executive function in youth. *Current Biology*, *27*(11), 1561–1572. https://doi.org/10.1016/j.cub.2017.04.051

Bazzi, M., Jeub, L. G. S., Arenas, A., Howison, S. D., & Porter, M. A. (2016). Generative Benchmark Models for Mesoscale Structure in Multilayer Networks, 1–22. https://doi.org/http://arxiv.org/abs/1608.06196

Beason-Held, L. L., Goh, J. O., An, Y., Kraut, M. A., O'Brien, R. J., Ferrucci, L., & Resnick, S. M. (2013). Changes in Brain Function Occur Years before the Onset of Cognitive Impairment. *Journal of Neuroscience*, *33*(46), 18008–18014. https://doi.org/10.1523/JNEUROSCI.1402-13.2013

Bentley, B., Branicky, R., Barnes, C. L., Chew, Y. L., Yemini, E., Bullmore, E. T., … Schafer, W. R. (2016). The multilayer connectome of caenorhabditis elegans. *PLoS Computational Biology*, *12*(12), 1–31. https://doi.org/10.1371/journal.pcbi.1005283

Berger, H. (1929). Über das Elektro- Enkephalogramm des Menschen. *Arch. Psychiatr. Nervenkr.*, *87*, 527–570. https://doi.org/10.1007/BF01797193

Betzel, R. F., & Bassett, D. S. (2017). Multi-scale brain networks. *NeuroImage*, *160*, 73–83. https://doi.org/10.1016/j.neuroimage.2016.11.006

Blondel, V. D., Guillaume, J.-L., Lambiotte, R., & Lefebvre, E. (2008). Fast unfolding of communities in large networks. *Journal of Statistical Mechanics: Theory and Experiment*, *2008*(10), 10008–10012. https://doi.org/10.1088/1742-

5468/2008/10/P10008

Boccaletti, S., Bianconi, G., Criado, R., del Genio, C. I., Gómez-Gardenes, J., Romance, M., … Zanin, M. (2014). The structure and dynamics of multilayer networks. *Physics Reports*, *544*(1), 1–122. https://doi.org/10.1016/j.physrep.2014.07.001

Braun, U., Schäfer, A., Walter, H., Erk, S., Romanczuk-Seiferth, N., Haddad, L., … Bassett, D. S. (2015). Dynamic reconfiguration of frontal brain networks during executive cognition in humans. *Proceedings of the National Academy of Sciences*, *112*(37), 11678–11683. https://doi.org/10.1073/pnas.1422487112

Brookes, M. J., Hale, J. R., Zumer, J. M., Stevenson, C. M., Francis, S. T., Barnes, G. R., … Nagarajan, S. S. (2011). Measuring functional connectivity using MEG: methodology and comparison with fcMRI. *NeuroImage*, *56*(3), 1082–1104. https://doi.org/10.1016/j.neuroimage.2011.02.054

Brookes, M. J., Stevenson, C. M., Barnes, G. R., Hillebrand, A., Simpson, M. I. G., Francis, S. T., & Morris, P. G. (2007). Beamformer reconstruction of correlated sources using a modified source model. *NeuroImage*, *34*(4), 1454–1465. https://doi.org/10.1016/j.neuroimage.2006.11.012

Brookes, M. J., Tewarie, P. K., Hunt, B. A. E., Robson, S. E., Gascoyne, L. E., Liddle, E. B., … Morris, P. G. (2016). A multi-layer network approach to MEG connectivity analysis. *NeuroImage*, *132*, 425–438. https://doi.org/10.1016/j.neuroimage.2016.02.045

Brookes, M. J., Vrba, J., Robinson, S. E., Stevenson, C. M., Peters, A. M., Barnes, G. R., … Morris, P. G. (2008). Optimising experimental design for MEG beamformer imaging. *NeuroImage*, *39*(4), 1788–1802. https://doi.org/10.1016/j.neuroimage.2007.09.050

Brookes, M. J., Woolrich, M. W., Luckhoo, H., Price, D., Hale, J. R., Stephenson, M. C., … Morris, P. G. (2011). Investigating the electrophysiological basis of resting state networks using magnetoencephalography. *Proceedings of the National Academy of Sciences*, *108*(40), 16783–16788. https://doi.org/10.1073/pnas.1112685108

Buffalo, E. A., Fries, P., Landman, R., Buschman, T. J., & Desimone, R. (2011). Laminar differences in gamma and alpha coherence in the ventral stream. *Proceedings of the National Academy of Sciences*, *108*(27), 11262–11267. https://doi.org/10.1073/pnas.1011284108

Buldú, J. M., & Porter, M. A. (2017). Frequency-based brain networks: From a multiplex framework to a full multilayer description. *Network Neuroscience*, *2*(4), 418–441. https://doi.org/10.1162/NETN_a_00033

Buzsáki, G., Horváth, Z., Urioste, R., Hetke, J., & Wise, K. (1992). High-frequency network oscillation in the hippocampus. *Science*, *256*(5059), 1025–1027. https://doi.org/10.1126/science.1589772

Capotosto, P., Babiloni, C., Romani, G. L., & Corbetta, M. (2009). Frontoparietal Cortex Controls Spatial Attention through Modulation of Anticipatory Alpha Rhythms. *Journal of Neuroscience*, *29*(18), 5863–5872. https://doi.org/10.1523/JNEUROSCI.0539-09.2009

Catani, M., Jones, D. K., & Ffytche, D. H. (2005). Perisylvian language networks of the human brain. *Annals of Neurology*, *57*(1), 8–16. https://doi.org/10.1002/ana.20319

Catani, M., & Mesulam, M. (2008). The arcuate fasciculus and the disconnection theme in language and aphasia: History and current state. *Cortex*, *44*(8), 953–961. https://doi.org/10.1016/j.cortex.2008.04.002

Cheng, C. H., Baillet, S., Hsiao, F. J., & Lin, Y. Y. (2013). Effects of aging on neuromagnetic mismatch responses to pitch changes. *Neuroscience Letters*, *544*, 20–24. https://doi.org/10.1016/j.neulet.2013.02.063

Cheyne, D., Bakhtazad, L., & Gaetz, W. (2006). Spatiotemporal mapping of cortical activity accompanying voluntary movements using an event-related beamforming approach. *Human Brain Mapping*, *27*(3), 213–229. https://doi.org/10.1002/hbm.20178

Cheyne, D., Bostan, A. C., Gaetz, W., & Pang, E. W. (2007). Event-related beamforming: A robust method for presurgical functional mapping using MEG. *Clinical Neurophysiology*, *118*(8), 1691–1704. https://doi.org/10.1016/j.clinph.2007.05.064

Cheyne, D. O. (2013). MEG studies of sensorimotor rhythms: A review. *Experimental Neurology*, *245*, 27–39. https://doi.org/10.1016/j.expneurol.2012.08.030

Cohen, D. (1968). Magnetoencephalography: Evidence of magnetic fields produced by alpha-rhythm currents. *Science*, *161*(3843), 784–786. https://doi.org/10.1126/science.161.3843.784

Cohen, D. (1972). Magnetoencephalography: Detection of the Brain's Electrical Activity with a Superconducting Magnetometer. *Science*, *175*(4022), 664–666. https://doi.org/10.1126/science.175.4022.664

Colclough, G. L., Brookes, M. J., Smith, S. M., & Woolrich, M. W. (2015). A symmetric multivariate leakage correction for MEG connectomes. *NeuroImage*, *117*, 439–448. https://doi.org/10.1016/j.neuroimage.2015.03.071

Colclough, G. L., Woolrich, M. W., Tewarie, P. K., Brookes, M. J., Quinn, A. J., & Smith, S. M.

(2016). How reliable are MEG resting-state connectivity metrics? *NeuroImage*, *138*, 284–293. https://doi.org/10.1016/j.neuroimage.2016.05.070

Crofts, J. J., Forrester, M., & O'Dea, R. D. (2016). Structure-function clustering in multiplex brain networks. *EPL*, *116*(1), 18003–18007. https://doi.org/10.1209/0295-5075/116/18003

Crossley, N. A., Mechelli, A., Scott, J., Carletti, F., Fox, P. T., Mcguire, P., & Bullmore, E. T. (2014). The hubs of the human connectome are generally implicated in the anatomy of brain disorders. *Brain*, *137*(8), 2382–2395. https://doi.org/10.1093/brain/awu132

Crossley, N. A., Mechelli, A., Vértes, P. E., Winton-Brown, T. T., Patel, A. X., Ginestet, C. E., … Bullmore, E. T. (2013). Cognitive relevance of the community structure of the human brain functional coactivation network. *Proceedings of the National Academy of Sciences*, *110*(38), 15502–15502. https://doi.org/10.1073/pnas.1314559110

Dale, A. M., Liu, A. K., Fischl, B., & Buckner, R. (2000). Dynamic statistical parametric mapping: combining fMRI and MEG for high-resolution imaging of cortical activity. *Neuron*, *26*, 55–67. https://doi.org/10.1016/S0896-6273(00)81138-1

De Domenico, M. (2017). Multilayer modeling and analysis of human brain networks. *GigaScience*, *6*, 1–8. https://doi.org/10.1093/gigascience/gix004

De Domenico, M., Nicosia, V., Arenas, A., & Latora, V. (2015). Structural reducibility of multilayer networks. *Nature Communications*, *6*, 1–9. https://doi.org/10.1038/ncomms7864

De Domenico, M., Sasai, S., & Arenas, A. (2016). Mapping multiplex hubs in human functional brain networks. *Frontiers in Neuroscience*, *10*, 1–14. https://doi.org/10.3389/fnins.2016.00326

De Domenico, M., Solé-Ribalta, A., Cozzo, E., Kivelä, M., Moreno, Y., Porter, M. A., … Arenas, A. (2013). Mathematical formulation of multi-layer networks. *Physical Review X*, *3*(4), 1–15. https://doi.org/10.1103/PhysRevX.3.041022

De Domenico, M., Solé-Ribalta, A., Omodei, E., Gómez, S., & Arenas, A. (2015). Ranking in interconnected multilayer networks reveals versatile nodes. *Nature Communications*, *6*, 1–6. https://doi.org/10.1038/ncomms7868

De Moor, B. (1993). The Singular Value Decomposition and Long and Short Spaces of Noisy Matrices. *IEEE Transactions on Signal Processing*, *41*(9), 2826–2838. https://doi.org/10.1109/78.236505

De Vico Fallani, F., Latora, V., & Chavez, M. (2017). A Topological Criterion for Filtering

Information in Complex Brain Networks. *PLOS Computational Biology*, *13*(1), 1–18. https://doi.org/10.1371/journal.pcbi.1005305

Demiralp, T., Yordanova, J., Kolev, V., Ademoglu, a, Devrim, M., & Samar, V. J. (1999). Time-frequency analysis of single-sweep event-related potentials by means of fast wavelet transform. *Brain and Language*, *66*(1), 129–145. https://doi.org/10.1006/brln.1998.2028

Desikan, R. S., Ségonne, F., Fischl, B., Quinn, B. T., Dickerson, B. C., Blacker, D., … Killiany, R. J. (2006). An automated labeling system for subdividing the human cerebral cortex on MRI scans into gyral based regions of interest. *NeuroImage*, *31*(3), 968–980. https://doi.org/10.1016/j.neuroimage.2006.01.021

Destrieux, C., Fischl, B., Dale, A., & Halgren, E. (2010). Automatic parcellation of human cortical gyri and sulci using standard anatomical nomenclature. *NeuroImage*, *53*(1), 1–15. https://doi.org/10.1016/j.neuroimage.2010.06.010

Dijkstra, E. W. (1959). A note on two problems in connexion with graphs. *Numerische Mathematik*, *1*(1), 269–271. https://doi.org/10.1007/BF01386390

Diwakar, M., Huang, M.-X., Srinivasan, R., Harrington, D. L., Robb, A., Angeles, A., … Lee, R. R. (2011). Dual-Core Beamformer for obtaining highly correlated neuronal networks in MEG. *NeuroImage*, *54*(1), 253–263. https://doi.org/10.1016/j.neuroimage.2010.07.023

Doesburg, S. M., Roggeveen, A. B., Kitajo, K., & Ward, L. M. (2008). Large-scale gamma-band phase synchronization and selective attention. *Cerebral Cortex*, *18*(2), 386–396. https://doi.org/10.1093/cercor/bhm073

Dougherty, K., Cox, M. A., Ninomiya, T., Leopold, D. A., & Maier, A. (2017). Ongoing alpha activity in V1 regulates visually driven spiking responses. *Cerebral Cortex*, *27*(2), 1113–1124. https://doi.org/10.1093/cercor/bhv304

Drakesmith, M., Caeyenberghs, K., Dutt, A., Lewis, G., David, A. S., & Jones, D. K. (2015). Overcoming the effects of false positives and threshold bias in graph theoretical analyses of neuroimaging data. *NeuroImage*, *118*, 313–333. https://doi.org/10.1016/j.neuroimage.2015.05.011

Eickhoff, S. B., Stephan, K. E., Mohlberg, H., Grefkes, C., Fink, G. R., Amunts, K., & Zilles, K. (2005). A new SPM toolbox for combining probabilistic cytoarchitectonic maps and functional imaging data. *NeuroImage*, *25*(4), 1325–1335. https://doi.org/10.1016/j.neuroimage.2004.12.034

Elbert, T., Pantev, C., Wienbruch, C., Rockstroh, B., & Taub, E. (1995). Increased Cortical Representation of the Fingers of the Left Hand in String Players. *Science*, *270*(5234), 305–307. https://doi.org/10.1126/science.270.5234.305

Ellens, W., Spieksma, F. M., Van Mieghem, P., Jamakovic, A., & Kooij, R. E. (2011). Effective graph resistance. *Linear Algebra and Its Applications*, *435*(10), 2491–2506. https://doi.org/10.1016/j.laa.2011.02.024

Engel, A. K., Gerloff, C., Hilgetag, C. C., & Nolte, G. (2013). Intrinsic Coupling Modes: Multiscale Interactions in Ongoing Brain Activity. *Neuron*, *80*(4), 867–886. https://doi.org/10.1016/j.neuron.2013.09.038

Evans, T. S. (2004). Complex networks. *Contemporary Physics*, *45*(6), 455–474. https://doi.org/10.1080/00107510412331283531

Florin, E., & Baillet, S. (2015). The brain's resting-state activity is shaped by synchronized cross-frequency coupling of neural oscillations. *NeuroImage*, *111*, 26–35. https://doi.org/10.1016/j.neuroimage.2015.01.054

Fox, P. T., Mintun, M. A., Raichle, M. E., & Herscovitch, P. (1984). A noninvasive approach to quantitative functional brain mapping with H2O15 and positron emission tomography. *Journal of Cerebral Blood Flow and Metabolism*, *4*(3), 329–333. https://doi.org/10.1038/jcbfm.1984.49

Frey, J. N., Ruhnau, P., & Weisz, N. (2015). Not so different after all: The same oscillatory processes support different types of attention. *Brain Research*, *1626*, 183–197. https://doi.org/10.1016/j.brainres.2015.02.017

Fries, P. (2005). A mechanism for cognitive dynamics: Neuronal communication through neuronal coherence. *Trends in Cognitive Sciences*, *9*(10), 474–480. https://doi.org/10.1016/j.tics.2005.08.011

Fries, P. (2009). Neuronal Gamma-Band Synchronization as a Fundamental Process in Cortical Computation. *Annual Review of Neuroscience*, *32*(1), 209–224. https://doi.org/10.1146/annurev.neuro.051508.135603

Friston, K. J. (2011). Functional and effective connectivity: A review. *Brain Connectivity*, *1*(1), 13–36. https://doi.org/10.1089/brain.2011.0008

Friston, K. J., Ashburner, J., Frith, C. D., Poline, J. B., Heather, J. D., & Frackowiak, R. S. J. (1995). Spatial registration and normalization of images. *Human Brain Mapping*, *2*(1995), 165–189.

Friston, K. J., Harrison, L., Daunizeau, J., Kiebel, S. J., Phillips, C., Trujillo-Barreto, N., …

Mattout, J. (2008). Multiple sparse priors for the M/EEG inverse problem. *NeuroImage*, *39*(3), 1104–1120. https://doi.org/10.1016/j.neuroimage.2007.09.048

Friston, K. J., Holmes, A. P., Worsley, K. J., Poline, J.-P., Frith, C. D., & Frackowiak, R. S. J. (1995). Statistical parametric maps in functional imaging: A general linear approach. *Human Brain Mapping*, *2*, 189–210. https://doi.org/10.1002/hbm.460020402

Fujita, A., Vidal, M. C., & Takahashi, D. Y. (2017). A statistical method to distinguish functional brain networks. *Frontiers in Neuroscience*, *11*(FEB). https://doi.org/10.3389/fnins.2017.00066

Garas, A. (2016). *Interconnected Networks* (1st ed.). Springer. https://doi.org/10.1007/978-3-319-23947-7

Garcés, P., Pereda, E., Hernández-Tamames, J. A., Del-Pozo, F., Maestú, F., & Ángel Pineda-Pardo, J. (2016). Multimodal description of whole brain connectivity: A comparison of resting state MEG, fMRI, and DWI. *Human Brain Mapping*, *37*(1), 20–34. https://doi.org/10.1002/hbm.22995

Garcia, J. O., Ashourvan, A., Muldoon, S., Vettel, J. M., & Bassett, D. S. (2018). Applications of Community Detection Techniques to Brain Graphs: Algorithmic Considerations and Implications for Neural Function. *Proceedings of the IEEE*, *106*(5), 846–867. https://doi.org/10.1109/JPROC.2017.2786710

Garrido, M. I., Barnes, G. R., Kumaran, D., Maguire, E. A., & Dolan, R. J. (2015). Ventromedial prefrontal cortex drives hippocampal theta oscillations induced by mismatch computations. *NeuroImage*, *120*, 362–370. https://doi.org/10.1016/j.neuroimage.2015.07.016

Gascoyne, L., Furlong, P. L., Hillebrand, A., Worthen, S. F., & Witton, C. (2016). Localising the auditory N1m with event-related beamformers: localisation accuracy following bilateral and unilateral stimulation. *Scientific Reports*, *6*, 31052. https://doi.org/10.1038/srep31052

Gaser, C., & Schlaug, G. (2003). Brain structures differ between musicians and non-musicians. *The Journal of Neuroscience*, *23*(27), 9240–9245. https://doi.org/10.1523/JNEUROSCI.23-27-09240.2003

Golub, G. H., & Van Loan, C. F. (1996). *Matrix Computations* (3rd ed., Vol. 10). Baltimore, Maryland: The Johns Hopkins University Press. https://doi.org/10.1063/1.3060478

Gómez, S., Guilera-Díaz, A., Gardeñes-Gòmez, J., Vicente-Pérez, C. J., Moreno, Y., & Arenas, A. (2013). Diffusion Dynamics on Multiplex Networks. *Physical Review Letters*, *028701*,

1–5. https://doi.org/10.1103/PhysRevLett.110.028701

Gong, G., He, Y., Concha, L., Lebel, C., Gross, D. W., Evans, A. C., & Beaulieu, C. (2009). Mapping anatomical connectivity patterns of human cerebral cortex using in vivo diffusion tensor imaging tractography. *Cerebral Cortex*, *19*(3), 524–536. https://doi.org/10.1093/cercor/bhn102

Goñi, J., van den Heuvel, M., Avena-Koenigsberger, A., Velez de Mendizabal, N., Betzel, R. F., Griffa, A., … Sporns, O. (2014). Resting-brain functional connectivity predicted by analytic measures of network communication. *Proceedings of the National Academy of Sciences*, *111*(2), 833–838. https://doi.org/10.1073/pnas.1315529111

Gordon, E. M., Laumann, T. O., Gilmore, A. W., Newbold, D. J., Greene, D. J., Berg, J. J., … Dosenbach, N. U. F. (2017). Precision Functional Mapping of Individual Human Brains. *Neuron*, *95*(4), 791–807. https://doi.org/10.1016/j.neuron.2017.07.011

Grahn, J. A., & Rowe, J. B. (2009). Feeling the Beat: Premotor and Striatal Interactions in Musicians and Nonmusicians during Beat Perception. *Journal of Neuroscience*, *29*(23), 7540–7548. https://doi.org/10.1523/JNEUROSCI.2018-08.2009

Granell, C., Gómez, S., & Arenas, A. (2013). Dynamical interplay between awareness and epidemic spreading in multiplex networks. *Physical Review Letters*, *111*(12), 1–5. https://doi.org/10.1103/PhysRevLett.111.128701

Gross, J., Baillet, S., Barnes, G. R., Henson, R. N., Hillebrand, A., Jensen, O., … Schoffelen, J.-M. (2013). Good practice for conducting and reporting MEG research. *NeuroImage*, *65*, 349–363. https://doi.org/10.1016/j.neuroimage.2012.10.001

Guillon, J., Attal, Y., Colliot, O., La Corte, V., Dubois, B., Schwartz, D., … De Vico Fallani, F. (2017). Loss of brain inter-frequency hubs in Alzheimer's disease. *Scientific Reports*, *7*(1), 10879. https://doi.org/10.1038/s41598-017-07846-w

Haegens, S., Osipova, D., Oostenveld, R., & Jensen, O. (2010). Somatosensory working memory performance in humans depends on both engagement and disengagement of regions in a distributed network. *Human Brain Mapping*, *31*(1), 26–35. https://doi.org/10.1002/hbm.20842

Halu, A., Mondragón, R. J., Panzarasa, P., & Bianconi, G. (2013). Multiplex PageRank. *PloS One*, *8*(10), e78293. https://doi.org/10.1371/journal.pone.0078293

Hämäläinen, M., Hari, R., Ilmoniemi, R. J., Knuutila, J., & Lounasmaa, O. V. (1993). Magnetoencephalography theory, instrumentation, and applications to noninvasive studies of the working human brain. *Reviews of Modern Physics*, *65*(2), 413–497.

https://doi.org/10.1103/RevModPhys.65.413

Hari, R., Aittoniemi, K., Järvinen, M.-L., Katila, T., & Varpula, T. (1980). Auditory Evoked Transient and Sustained Magnetic Fields of the Human Brain. *Experimental Brain Research*, *40*, 237–240. https://doi.org/10.1007/BF00237543

Hari, R., & Puce, A. (2017). *MEG-EEG Primer*. Oxford University Press. https://doi.org/10.1093/med/9780190497774.001.0001

Hari, R., & Salmelin, R. (2012). Magnetoencephalography: From SQUIDs to neuroscience. Neuroimage 20th anniversary special edition. *NeuroImage*, *61*(2), 386–396. https://doi.org/10.1016/j.neuroimage.2011.11.074

Hauk, O. (2004). Keep it simple: A case for using classical minimum norm estimation in the analysis of EEG and MEG data. *NeuroImage*, *21*(4), 1612–1621. https://doi.org/10.1016/j.neuroimage.2003.12.018

Hauk, O., Wakeman, D. G., & Henson, R. N. (2011). Comparison of noise-normalized minimum norm estimates for MEG analysis using multiple resolution metrics. *NeuroImage*, *54*(3), 1966–1974. https://doi.org/10.1016/j.neuroimage.2010.09.053

He, Y., Chen, Z. J., & Evans, A. C. (2007). Small-world anatomical networks in the human brain revealed by cortical thickness from MRI. *Cerebral Cortex*, *17*(10), 2407–2419. https://doi.org/10.1093/cercor/bhl149

Herholz, S. C., & Zatorre, R. J. (2012). Musical Training as a Framework for Brain Plasticity: Behavior, Function, and Structure. *Neuron*, *76*(3), 486–502. https://doi.org/10.1016/j.neuron.2012.10.011

Hernandez, J. M., & Van Mieghem, P. (2011). Classification of graph metrics, 1–20.

Hillebrand, A., & Barnes, G. R. (2002). A quantitative assessment of the sensitivity of whole-head MEG to activity in the adult human cortex. *NeuroImage*, *16*(3), 638–650. https://doi.org/10.1006/nimg.2002.1102

Hillebrand, A., & Barnes, G. R. (2005). Beamformer analysis of MEG data. *International Review of Neurobiology*, *68*(05), 149–171. https://doi.org/10.1016/S0074-7742(05)68006-3

Hillebrand, A., Barnes, G. R., Bosboom, J. L., Berendse, H. W., & Stam, C. J. (2012). Frequency-dependent functional connectivity within resting-state networks: an atlas-based MEG beamformer solution. *NeuroImage*, *59*(4), 3909–3921. https://doi.org/10.1016/j.neuroimage.2011.11.005

Hillebrand, A., Singh, K. D., Holliday, I. E., Furlong, P. L., & Barnes, G. R. (2005). A new

approach to neuroimaging with magnetoencephalography. *Human Brain Mapping*, *25*(2), 199–211. https://doi.org/10.1002/hbm.20102

Hincapié, A. S., Kujala, J., Mattout, J., Pascarella, A., Daligault, S., Delpuech, C., … Jerbi, K. (2017). The impact of MEG source reconstruction method on source-space connectivity estimation: A comparison between minimum-norm solution and beamforming. *NeuroImage*, *156*, 29–42. https://doi.org/10.1016/j.neuroimage.2017.04.038

Hipp, J. F., Hawellek, D. J., Corbetta, M., Siegel, M., & Engel, A. K. (2012). Large-scale cortical correlation structure of spontaneous oscillatory activity. *Nature Neuroscience*, *15*(6), 884–890. https://doi.org/10.1038/nn.3101

Hlinka, J., & Coombes, S. (2012). Using computational models to relate structural and functional brain connectivity. *European Journal of Neuroscience*, *36*(2), 2137–2145. https://doi.org/10.1111/j.1460-9568.2012.08081.x

Hobson, J. A., & Pace-Schott, E. F. (2002). The cognitive neuroscience of sleep: Neuronal systems, consciousness and learning. *Nature Reviews Neuroscience*, *3*(9), 679–693. https://doi.org/10.1038/nrn915

Hsiao, F. J., Wu, Z. A., Ho, L. T., & Lin, Y. Y. (2009). Theta oscillation during auditory change detection: An MEG study. *Biological Psychology*, *81*(1), 58–66. https://doi.org/10.1016/j.biopsycho.2009.01.007

Huang, M.-X., Lee, R. R., Miller, G. A., Thoma, R. J., Hanlon, F. M., Paulson, K. M., … Canive, J. M. (2005). A parietal-frontal network studied by somatosensory oddball MEG responses, and its cross-modal consistency. *NeuroImage*, *28*(1), 99–114. https://doi.org/10.1016/j.neuroimage.2005.05.036

Huang, M.-X., Mosher, J. C., & Leahy, R. M. (1999). A sensor-weighted overlapping-sphere head model and exhaustive head model comparison for MEG. *Physics in Medicine and Biology*, *44*(2), 423–440. https://doi.org/10.1088/0031-9155/44/2/010

Huettel, S., Song, A., & McCarthy, G. (2009). *Functional Magnetic Resonance Imaging* (2nd ed.). Sunderland: Sinauer.

Hunt, B. A. E., Tewarie, P. K., Mougin, O. E., Geades, N., Jones, D. K., Singh, K. D., … Brookes, M. J. (2016). Relationships between cortical myeloarchitecture and electrophysiological networks. *Proceedings of the National Academy of Sciences*, *113*(47), 13510–13515. https://doi.org/10.1073/pnas.1608587113

Iacovacci, J., Rahmede, C., Arenas, A., & Bianconi, G. (2016). Functional Multiplex PageRank. *Europhysics Letters*, *116*, 1–7. https://doi.org/10.1209/0295-5075/116/28004

Ishii, R., Canuet, L., Herdman, A., Gunji, A., Iwase, M., Takahashi, H., … Takeda, M. (2009). Cortical oscillatory power changes during auditory oddball task revealed by spatially filtered magnetoencephalography. *Clinical Neurophysiology*, *120*(3), 497–504. https://doi.org/10.1016/j.clinph.2008.11.023

Ishii, R., Canuet, L., Ishihara, T., Aoki, Y., Ikeda, S., Hata, M., … Takeda, M. (2014). Frontal midline theta rhythm and gamma power changes during focused attention on mental calculation: an MEG beamformer analysis. *Frontiers in Human Neuroscience*, *8*(June), 406. https://doi.org/10.3389/fnhum.2014.00406

Iturria-Medina, Y., Sotero, R. C., Canales-Rodríguez, E. J., Alemán-Gómez, Y., & Melie-García, L. (2008). Studying the human brain anatomical network via diffusion-weighted MRI and Graph Theory. *NeuroImage*, *40*(3), 1064–1076. https://doi.org/10.1016/j.neuroimage.2007.10.060

Jalili, M. (2016). Functional brain networks: Does the choice of dependency estimator and binarization method matter? *Scientific Reports*, *6*, 29780. https://doi.org/10.1038/srep29780

Jäncke, L. (2009a). The Architecture of the Golfer's Brain. *PLoS ONE*, *101*(11), 1435–1439. https://doi.org/10.1371/journal.pone.0004785

Jäncke, L. (2009b). The plastic human brain. *Restorative Neurology and Neuroscience*, *27*(5), 521–538. https://doi.org/10.3233/RNN-2009-0519

Jäncke, L. (2012). The dynamic audio-motor system in pianists. *Annals of the New York Academy of Sciences*, *1252*(1), 246–252. https://doi.org/10.1111/j.1749-6632.2011.06416.x

Jensen, O., & Colgin, L. L. (2007). Cross-frequency coupling between neuronal oscillations. *Trends in Cognitive Sciences*, *11*(7), 267–269. https://doi.org/10.1016/j.tics.2007.05.003

Jensen, O., & Mazaheri, A. (2010). Shaping functional architecture by oscillatory alpha activity: Gating by inhibition. *Frontiers in Human Neuroscience*, *4*, 1–8. https://doi.org/10.3389/fnhum.2010.00186

Jensen, O., & Tesche, C. D. (2002). Frontal theta activity in humans increases with memory load in a working memory task. *European Journal of Neuroscience*, *15*(8), 1395–1399. https://doi.org/10.1046/j.1460-9568.2002.01975.x

Jobst, C., Ferrari, P., Isabella, S., & Cheyne, D. (2018). BrainWave: A matlab toolbox for beamformer source analysis of MEG data. *Frontiers in Neuroscience*, *12*(AUG), 1–17.

https://doi.org/10.3389/fnins.2018.00587

Jones, E. G. (1999). Golgi, Cajal and the Neuron Doctrine. *Journal of the History of the Neurosciences*, *8*(2), 170–178. https://doi.org/10.1076/jhin.8.2.170.1838

Josephson, B. D. (1962). Possible new effects in superconductive tunnelling. *Physics Letters*, *1*(7), 251–253. https://doi.org/10.1016/0031-9163(62)91369-0

Jurkiewicz, M. T., Gaetz, W. C., Bostan, A. C., & Cheyne, D. (2006). Post-movement beta rebound is generated in motor cortex: Evidence from neuromagnetic recordings. *NeuroImage*, *32*(3), 1281–1289. https://doi.org/10.1016/j.neuroimage.2006.06.005

Kandel, E., Schwartz, J., Jessell, T. (2000). *Principles of Neural Science* (4th ed.). New York: McGraw-Hill.

Karrer, B., & Newman, M. E. J. (2011). Stochastic blockmodels and community structure in networks. *Physical Review E*, *83*(1), 1–11. https://doi.org/10.1103/PhysRevE.83.016107

Kiehl, K. A., Laurens, K. R., Duty, T. L., Forster, B. B., & Liddle, P. F. (2001). Neural sources involved in auditory target detection and novelty processing: an event-related fMRI study. *Psychophysiology*, *38*, 133–142. https://doi.org/10.1111/1469-8986.3810133

Kivelä, M., Arenas, A., Barthelemy, M., Gleeson, J. P., Moreno, Y., & Porter, M. A. (2014). Multilayer networks. *Journal of Complex Networks*, *2*(3), 203–271. https://doi.org/10.1093/comnet/cnu016

Klein, C., Liem, F., Hänggi, J., Elmer, S., & Jäncke, L. (2016). The "silent" imprint of musical training. *Human Brain Mapping*, *37*(2), 536–546. https://doi.org/10.1002/hbm.23045

Klimesch, W., Doppelmayr, M., Schimke, H., & Ripper, B. (1997). Theta synchronization and alpha desynchronization in a memory task. *Psychophysiology*, *34*(2), 169–176. https://doi.org/10.1111/j.1469-8986.1997.tb02128.x

Knight, R. T., Scabini, D., Woods, D. L., & Clayworth, C. C. (1989). Contributions of temporal-parietal junction to the human auditory P3. *Brain Research*, *502*(1), 109–116. https://doi.org/10.1016/0006-8993(89)90466-6

Kok, A. (2001). On the utility of P3 amplitude as a measure of processing capacity. *Psychophysiology*, *38*, 557–577. https://doi.org/10.1016/S0167-8760(98)90168-4

Krause, C. M., Sillanmäki, L., Koivisto, M., Saarela, C., Häggqvist, A., Laine, M., & Hämäläinen, H. (2000). The effects of memory load on event-related EEG desynchronization and synchronization. *Clinical Neurophysiology*, *111*(11), 2071–2078. https://doi.org/10.1016/S1388-2457(00)00429-6

Kruskal, J. B. (1956). On the Shortest Spanning Subtree of a Graph and the Traveling Salesman Problem. *Proceedings of the American Mathematical Society*, *7*(1), 48. https://doi.org/10.1090/S0002-9939-1956-0078686-7

Langer, N., von Bastian, C. C., Wirz, H., Oberauer, K., & Jäncke, L. (2013). The effects of working memory training on functional brain network efficiency. *Cortex*, *49*(9), 2424–2438. https://doi.org/10.1016/j.cortex.2013.01.008

Lappe, C., Steinsträter, O., & Pantev, C. (2013). Rhythmic and melodic deviations in musical sequences recruit different cortical areas for mismatch detection. *Frontiers in Human Neuroscience*, *7*, 260–268. https://doi.org/10.3389/fnhum.2013.00260

Larson-Prior, L. J., Oostenveld, R., Della Penna, S., Michalareas, G., Prior, F., Babajani-Feremi, A., … Snyder, A. Z. (2013). Adding dynamics to the Human Connectome Project with MEG. *NeuroImage*, *80*, 190–201. https://doi.org/10.1016/j.neuroimage.2013.05.056

Lauterbur, P. C. (1973). Image formation by induced local interactions: Examples employing nuclear magnetic resonance. *Nature*, *242*, 190–191. https://doi.org/10.1038/242190a0

Lega, B. C., Jacobs, J., & Kahana, M. (2012). Human hippocampal theta oscillations and the formation of episodic memories. *Hippocampus*, *22*(4), 748–761. https://doi.org/10.1002/hipo.20937

Litvak, V., Mattout, J., Kiebel, S., Phillips, C., Henson, R., Kilner, J., … Friston, K. J. (2011). EEG and MEG data analysis in SPM8. *Computational Intelligence and Neuroscience*, *2011*, 1–32. https://doi.org/10.1155/2011/852961

Liuzzi, L., Gascoyne, L. E., Tewarie, P. K., Barratt, E. L., Boto, E., & Brookes, M. J. (2017). Optimising experimental design for MEG resting state functional connectivity measurement. *NeuroImage*, *155*(November 2016), 565–576. https://doi.org/10.1016/j.neuroimage.2016.11.064

Lopez, J. D., Penny, W. D., Espinosa, J. J., & Barnes, G. R. (2012). A general Bayesian treatment for MEG source reconstruction incorporating lead field uncertainty. *NeuroImage*, *60*(2), 1194–1204. https://doi.org/10.1016/j.neuroimage.2012.01.077

Lord, A., Ehrlich, S., Borchardt, V., Geisler, D., Seidel, M., Huber, S., … Walter, M. (2016). Brain parcellation choice affects disease-related topology differences increasingly from global to local network levels. *Psychiatry Research: Neuroimaging*, *249*, 12–19.

Luck, S. J. (2005). *An introduction to the event-related potential technique* (2nd ed.). Cambridge, MA: MIT Press.

Luckhoo, H., Hale, J. R., Stokes, M. G., Nobre, A. C., Morris, P. G., Brookes, M. J., & Woolrich,

M. W. (2012). Inferring task-related networks using independent component analysis in magnetoencephalography. *NeuroImage*, *62*(1), 530–541. https://doi.org/10.1016/j.neuroimage.2012.04.046

Luo, C., Guo, Z.-W., Lai, Y., Liao, W., Liu, Q., Kendrick, K. M., … Li, H. (2012). Musical training induces functional plasticity in perceptual and motor networks: Insights from resting-state fMRI. *PLoS ONE*, *7*(5), 1–10. https://doi.org/10.1371/journal.pone.0036568

Maguire, E. A., Gadian, D. G., Johnsrude, I. S., Good, C. D., Ashburner, J., Frackowiak, R. S. J., & Frith, C. D. (2000). Navigation-related structural change in the hippocampi of taxi drivers. *Proceedings of the National Academy of Sciences*, *97*(8), 4398–4403. https://doi.org/10.1073/pnas.070039597

Mäkelä, J. P., Hari, R. (1990). Long-latency auditory evoked magnetic fields. *Advances in Neurology*, *54*, 177–191.

Mandke, K., Meier, J. M., Brookes, M. J., O'Dea, R. D., Van Mieghem, P., Stam, C. J., … Tewarie, P. K. (2018). Comparing multilayer brain networks between groups: Introducing graph metrics and recommendations. *NeuroImage*, *166*, 371–384. https://doi.org/10.1016/j.neuroimage.2017.11.016

Mansfield, P. (1977). Multi-planar image-formation using nmr spin echoes. *Journal of Physics C-Solid State Physics*, *10*(3), L55–L58. https://doi.org/10.1088/0022-3719/10/3/004

Mansfield, P., & Grannell, P. K. (1973). NMR diffraction in solids. *Journal of Physics C-Solid State Physics*, *6*(22), L422–L426. https://doi.org/10.1088/0022-3719/6/22/007

Marcus, C., Mena, E., & Subramaniam, R. M. (2014). Brain PET in the diagnosis of Alzheimer's disease. *Clinical Nuclear Medicine*, *39*(10), e413–e426. https://doi.org/10.1097/RLU.0000000000000547

Maris, E., & Oostenveld, R. (2007). Nonparametric statistical testing of EEG- and MEG-data. *Journal of Neuroscience Methods*, *164*(1), 177–190. https://doi.org/10.1016/j.jneumeth.2007.03.024

Märtens, M., Meier, J., Hillebrand, A., Tewarie, P., & Van Mieghem, P. (2017). Brain network clustering with information flow motifs. *Applied Network Science*, *2*(25), 1–18. https://doi.org/10.1007/s41109-017-0046-z

Martín-Hernández, J., Wang, H., Van Mieghem, P., & D'Agostino, G. (2014). Algebraic connectivity of interdependent networks. *Physica A: Statistical Mechanics and Its Applications*, *404*, 92–105. https://doi.org/10.1016/j.physa.2014.02.043

Mehta-Pandejee, G., Robinson, P. A., Henderson, J. A., Aquino, K. M., & Sarkar, S. (2017).

Inference of direct and multistep effective connectivities from functional connectivity of the brain and of relationships to cortical geometry. *Journal of Neuroscience Methods*, *283*, 42–54. https://doi.org/10.1016/j.jneumeth.2017.03.014

Meier, J. M., Märtens, M., Hillebrand, A., Tewarie, P. K., & Van Mieghem, P. (2017). Motif-Based Analysis of Effective Connectivity in Brain Networks. In H. Cherifi, S. Gaito, W. Quattrociocchi, & A. Sala (Eds.), *Complex Networks & Their Applications V* (pp. 685–696). Cham: Springer International Publishing.

Meier, J. M., Tewarie, P. K., Hillebrand, A., Douw, L., van Dijk, B. W., Stufflebeam, S. M., & Van Mieghem, P. (2016). A mapping between structural and functional brain networks. *Brain Connectivity*, *6*(4), 298–311.

Meier, J. M., Tewarie, P. K., & Van Mieghem, P. (2015). The Union of Shortest Path Trees of Functional Brain Networks. *Brain Connectivity*, *5*(9), 575–581. https://doi.org/10.1089/brain.2014.0330

Meunier, D., Lambiotte, R., Fornito, A., Ersche, K. D., & Bullmore, E. T. (2009). Hierarchical modularity in human brain functional networks. *Frontiers in Human Neuroscience*, *3*(October), 1–12. https://doi.org/10.3389%2Fneuro.11.037.2009

Meyer, S. S., Bonaiuto, J., Lim, M., Rossiter, H., Waters, S., Bradbury, D., … Barnes, G. R. (2017). Flexible head-casts for high spatial precision MEG. *Journal of Neuroscience Methods*, *276*, 38–45. https://doi.org/10.1016/j.jneumeth.2016.11.009

Micheloyannis, S., Pachou, E., Stam, C. J., Vourkas, M., Erimaki, S., & Tsirka, V. (2006). Using graph theoretical analysis of multi channel EEG to evaluate the neural efficiency hypothesis. *Neuroscience Letters*, *402*(3), 273–277. https://doi.org/10.1016/j.neulet.2006.04.006

Milgram, S. (1967). The small world problem. *Psychology Today*, *2*(1), 61–67. https://doi.org/10.1007/BF02717530

Missonnier, P., Deiber, M. P., Gold, G., Millet, P., Gex-Fabry Pun, M., Fazio-Costa, L., … Ibáñez, V. (2006). Frontal theta event-related synchronization: Comparison of directed attention and working memory load effects. *Journal of Neural Transmission*, *113*(10), 1477–1486. https://doi.org/10.1007/s00702-005-0443-9

Mohamed, W. (2008). The Edwin Smith Surgical Papyrus: Neuroscience in Ancient Egypt. Retrieved July 1, 2018, from http://www.ibro.info/Pub/Pub_Main_Display.asp?LC_Docs_ID=3199

Moiseev, A., & Herdman, A. T. (2013). Multi-core beamformers: Derivation, Limitations and

improvements. *NeuroImage*, *71*, 135–146. https://doi.org/10.1016/j.neuroimage.2012.12.072

Mosher, J. C., Baillet, S., & Leahy, R. M. (2003). Equivalence of linear approaches in bioelectromagnetic inverse solutions. *IEEE Workshop on Statistical Signal Processing Proceedings*, (5), 294–297. https://doi.org/10.1109/SSP.2003.1289402

Mucha, P. J., Richardson, T., Macon, K., Porter, M. A., & Onnela, J.-P. (2010). Community structure in time-dependent, multiscale, and multiplex networks. *Science*, *328*(5980), 876–878.

Näätänen, R. N., Paavilainen, P., Rinne, T., & Alho, K. (2007). The mismatch negativity (MMN) in basic research of central auditory processing: A review. *Clinical Neurophysiology*, *118*(12), 2544–2590. https://doi.org/10.1016/j.clinph.2007.04.026

Newman, M. E. J. (2006). Modularity and community structure in networks. *Proceedings of the National Academy of Sciences*, *103*(23), 8577–8582. https://doi.org/10.1073/pnas.0601602103

Nichols, T. E., & Holmes, A. P. (2001). Nonparametric permutation tests for (PET) functional neuroimaging experiments: A primer with examples. *Human Brain Mapping*, *15*(1), 1–25. https://doi.org/10.1002/hbm.1058

Nicosia, V., Bianconi, G., Latora, V., & Barthelemy, M. (2013). Growing multiplex networks. *Physical Review Letters*, *111*(5), 58701. https://doi.org/10.1103/PhysRevLett.111.058701

Nicosia, V., Bianconi, G., Latora, V., & Barthelemy, M. (2014). Nonlinear growth and condensation in multiplex networks. *Physical Review E - Statistical, Nonlinear, and Soft Matter Physics*, *90*(4), 1–13. https://doi.org/10.1103/PhysRevE.90.042807

Nicosia, V., & Latora, V. (2015). Measuring and modeling correlations in multiplex networks. *Physical Review E - Statistical, Nonlinear, and Soft Matter Physics*, *92*, 32805. https://doi.org/10.1103/PhysRevE.92.032805

Nishitani, N., Nagamine, T., Fujiwara, N., Yazawa, S., & Shibasaki, H. (1998). Cortical-hippocampal auditory processing identified by magnetoencephalography. *Journal of Cognitive Neuroscience*, *10*(2), 231–247. https://doi.org/10.1162/089892998562672

Niso, G., Rogers, C., Moreau, J. T., Chen, L. Y., Madjar, C., Das, S., … Baillet, S. (2016). OMEGA: The Open MEG Archive. *NeuroImage*, *124*, 1182–1187. https://doi.org/10.1016/j.neuroimage.2015.04.028

O'Donnell, B. F., Cohen, R. A., Hokama, H., Cuffin, B. N., Lippa, C., Shenton, M. E., &

Drachman, D. A. (1993). Electrical source analysis of auditory ERPs in medial temporal lobe amnestic syndrome. *Electroencephalography and Clinical Neurophysiology*, *87*(6), 394–402. https://doi.org/10.1016/0013-4694(93)90153-M

O'Neill, G. C., Barratt, E. L., Hunt, B. A. E., Tewarie, P. K., & Brookes, M. J. (2015). Measuring electrophysiological connectivity by power envelope correlation: a technical review on MEG methods. *Physics in Medicine and Biology*, *60*(21), R271–R295. https://doi.org/10.1088/0031-9155/60/21/R271

O'Neill, G. C., Tewarie, P., Vidaurre, D., Liuzzi, L., Woolrich, M. W., & Brookes, M. J. (2018). Dynamics of large-scale electrophysiological networks: A technical review. *NeuroImage*, *180*(15), 559–576. https://doi.org/10.1016/j.neuroimage.2017.10.003

Öniz, A., & Başar, E. (2009). Prolongation of alpha oscillations in auditory oddball paradigm. *International Journal of Psychophysiology*, *71*(3), 235–241. https://doi.org/10.1016/j.ijpsycho.2008.10.003

Palomar-García, M. Á., Zatorre, R. J., Ventura-Campos, N., Bueichekú, E., & Ávila, C. (2017). Modulation of Functional Connectivity in Auditory-Motor Networks in Musicians Compared with Nonmusicians. *Cerebral Cortex*, *27*(5), 2768–2778. https://doi.org/10.1093/cercor/bhw120

Palva, S., & Palva, J. M. (2007). New vistas for α-frequency band oscillations. *Trends in Neurosciences*, *30*(4), 150–158. https://doi.org/10.1016/j.tins.2007.02.001

Pfurtscheller, G., & Lopes da Silva, F. H. (1999). Event-related EEG/MEG synchronization and desynchronization: basic principles. *Clinical Neurophysiology*, *110*(11), 1842–1857. https://doi.org/10.1016/S1388-2457(99)00141-8

Pfurtscheller, G., Neuper, C., Brunner, C., & Lopes Da Silva, F. (2005). Beta rebound after different types of motor imagery in man. *Neuroscience Letters*, *378*(3), 156–159. https://doi.org/10.1016/j.neulet.2004.12.034

Poldrack, R. A., Baker, C. I., Durnez, J., Gorgolewski, K. J., Matthews, P. M., Munafò, M., … Yarkoni, T. (2016). Scanning the Horizon: Towards transparent and reproducible neuroimaging research. https://doi.org/10.1038/nrn.2016.167

Polich, J. (2007). Updating P300: an integrative theory of P3a and P3b. *Clinical Neurophysiology*, *118*(10), 2128–2148. https://doi.org/10.1016/j.clinph.2007.04.019

Polich, J., & Squire, L. R. (1993). P300 from amnesic patients with bilateral hippocampal lesions. *Electroencephalography and Clinical Neurophysiology*, *86*(6), 408–417. https://doi.org/10.1016/0013-4694(93)90136-J

Power, J. D., Cohen, A. L., Nelson, S. M., Wig, G. S., Barnes, K. A., Church, J. A., … Petersen, S. E. (2011). Functional Network Organization of the Human Brain. *Neuron*, *72*(4), 665–678. https://doi.org/10.1016/j.neuron.2011.09.006

Proix, T., Spiegler, A., Schirner, M., Rothmeier, S., Ritter, P., & Jirsa, V. K. (2016). How do parcellation size and short-range connectivity affect dynamics in large-scale brain network models? *NeuroImage*, *142*, 135–149. https://doi.org/10.1016/j.neuroimage.2016.06.016

Proverbio, A. M., Calbi, M., Manfredi, M., & Zani, A. (2014). Audio-visuomotor processing in the Musician's brain: An ERP study on professional violinists and clarinetists. *Scientific Reports*, *4*, 5866. https://doi.org/10.1038/srep05866

Robinson, P. A. (2012). Interrelating anatomical, effective, and functional brain connectivity using propagators and neural field theory. *Physical Review E*, *85*(1), 11912. https://doi.org/10.1103/PhysRevE.85.011912

Robinson SE, V. J. (2002). Functional Neuroimaging by Synthetic Aperture Magnetometry. In *Yoshimoto, T., Kotani M, Kuriki S, Karibe H, Nkasato N (Eds), Recent Advances in Biomagnetism* (pp. 302–305). Sendai: Tohuku University Press.

Rubinov, M., & Sporns, O. (2010). Complex network measures of brain connectivity: Uses and interpretations. *NeuroImage*, *52*(3), 1059–1069. https://doi.org/10.1016/j.neuroimage.2009.10.003

Sahneh, F. D., & Caterina, S. (2014). Competitive epidemic spreading over arbitrary multilayer networks. *Physical Review E - Statistical, Nonlinear, and Soft Matter Physics*, *89*(6), 1–15. https://doi.org/10.1103/PhysRevE.89.062817

Sahneh, F. D., Scoglio, C., & Van Mieghem, P. (2015). Exact coupling threshold for structural transition reveals diversified behaviors in interconnected networks. *Physical Review E - Statistical, Nonlinear, and Soft Matter Physics*, *92*(4), 1–5. https://doi.org/10.1103/PhysRevE.92.040801

Sarvas, J. (1987). Basic mathematical and electromagnetic concepts of the biomagnetic inverse problem. *Physics in Medicine and Biology*, *32*(1), 11–22. https://doi.org/10.1088/0031-9155/32/1/004

Schlaug, G. (2015). Musicians and music making as a model for the study of brain plasticity. *Progress in Brain Research*, *217*, 37–55. https://doi.org/10.1016/bs.pbr.2014.11.020

Schlaug, G., Jäncke, L., Huang, Y., Staiger, J. F., & Steinmetz, H. (1995). Increased corpus callosum size in musicians. *Neuropsychologia*, *33*(8), 1047–1055.

https://doi.org/10.1016/0028-3932(95)00045-5

Schneider, P., Scherg, M., Dosch, H. G., Specht, H. J., Gutschalk, A., & Rupp, A. (2002). Morphology of Heschl's gyrus reflects enhanced activation in the auditory cortex of musicians. *Nature Neuroscience*, *5*(7), 688–694. https://doi.org/10.1038/nn871

Schoffelen, J.-M., & Gross, J. (2009). Source connectivity analysis with MEG and EEG. *Human Brain Mapping*, *30*(6), 1857–1865. https://doi.org/10.1002/hbm.20745

Scholz, J., Klein, M. C., Behrens, T. E. J., & Johansen-Berg, H. (2010). Training induces changes in white matter architecture. *Nature Neuroscience*, *12*(11), 1370–1371. https://doi.org/10.1038/nn.2412

Sejnowski, T. J., Churchland, P. S., & Movshon, J. A. (2014). Putting big data to good use in neuroscience. *Nature Neuroscience*, *17*(11), 1440–1441. https://doi.org/10.1038/nn.3839

Senkowski, D., & Gallinat, J. (2015). Dysfunctional prefrontal gamma-band oscillations reflect working memory and other cognitive deficits in schizophrenia. *Biological Psychiatry*, *77*(12), 1010–1019. https://doi.org/10.1016/j.biopsych.2015.02.034

Shahin, A., Bosnyak, D. J., Trainor, L. J., & Roberts, L. E. (2003). Enhancement of Neuroplastic P2 and N1c Auditory Evoked Potentials in Musicians. *Journal of Neuroscience*, *23*(13), 5545–5552. https://doi.org/10.1523/JNEUROSCI.23-13-05545.2003

Singer, W., & Gray, C. M. (1995). Visual Feature Integration and the Temporal Correlation Hypothesis. *Annual Review of Neuroscience*, *18*(1), 555–586. https://doi.org/10.1146/annurev.neuro.18.1.555

Singh, K. D., Barnes, G. R., & Hillebrand, A. (2003). Group imaging of task-related changes in cortical synchronisation using nonparametric permutation testing. *NeuroImage*, *19*(4), 1589–1601. https://doi.org/10.1016/S1053-8119(03)00249-0

Smit, D. J. A., Stam, C. J., Posthuma, D., Boomsma, D. I., & De Geus, E. J. C. (2008). Heritability of "small-world" networks in the brain: A graph theoretical analysis of resting-state EEG functional connectivity. *Human Brain Mapping*, *29*(12), 1368–1378. https://doi.org/10.1002/hbm.20468

Smith, K., Azami, H., Parra, M. A., Starr, J. M., & Escudero, J. (2015). Cluster-span threshold: An unbiased threshold for binarising weighted complete networks in functional connectivity analysis. In *Proceedings of the Annual International Conference of the IEEE Engineering in Medicine and Biology Society, EMBS* (Vol. 2015, pp. 2840–2843). IEEE. https://doi.org/10.1109/EMBC.2015.7318983

Smith, S. M. (2002). Fast robust automated brain extraction. *Human Brain Mapping*, *17*(3), 143–155. https://doi.org/10.1002/hbm.10062

Smith, S. M., Jenkinson, M., Woolrich, M. W., Beckmann, C. F., Behrens, T. E. J., Johansen-Berg, H., … Matthews, P. M. (2004). Advances in Functional and Structural MR Image Analysis and Implementation as FSL Technical. *Neuroimage*, *23(S1)*(SUPPL. 1), 208–219. https://doi.org/10.1016/j.neuroimage.2004.07.051

Solá, L., Romance, M., Criado, R., Flores, J., García del Amo, A., & Boccaletti, S. (2013). Eigenvector centrality of nodes in multiplex networks. *Chaos*, *23*, 33131–11. https://doi.org/https://doi.org/10.1063/1.4818544

Solé-Ribalta, A., De Domenico, M., Gómez, S., & Arenas, A. (2014). Centrality rankings in multiplex networks. In *Proceedings of the 2014 ACM conference on Web science - WebSci '14* (pp. 149–155). ACM. https://doi.org/10.1145/2615569.2615687

Sporns, O., & Betzel, R. F. (2016). Modular brain networks. *Annual Review of Psychology*, *67*(1), 613–640. https://doi.org/10.1146/annurev-psych-122414-033634

Stam, C. J. (2014). Modern network science of neurological disorders. *Nature Reviews Neuroscience*, *15*(10), 683–695. https://doi.org/10.1038/nrn3801

Stam, C. J., Jones, B. F., Nolte, G., Breakspear, M., & Scheltens, P. (2007). Small-world networks and functional connectivity in Alzheimer's disease. *Cerebral Cortex*, *17*(1), 92–99. https://doi.org/10.1093/cercor/bhj127

Stam, C. J., Montez, T., Jones, B. F., Rombouts, S. A. R. B., Van Der Made, Y., Pijnenburg, Y. A. L., & Scheltens, P. (2005). Disturbed fluctuations of resting state EEG synchronization in Alzheimer's disease. *Clinical Neurophysiology*, *116*(3), 708–715. https://doi.org/10.1016/j.clinph.2004.09.022

Stam, C. J., Tewarie, P. K., Van Dellen, E., van Straaten, E. C. W., Hillebrand, A., & Van Mieghem, P. (2014). The trees and the forest: Characterization of complex brain networks with minimum spanning trees. *International Journal of Psychophysiology*, *92*(3), 129–138. https://doi.org/10.1016/j.ijpsycho.2014.04.001

Stam, C. J., & van Straaten, E. C. W. (2012). The organization of physiological brain networks. *Clinical Neurophysiology*, *123*(6), 1067–1087. https://doi.org/10.1016/j.clinph.2012.01.011

Stampfer, H. G., & Başar, E. (1985). Does frequency analysis lead to better understanding of human event related potentials. *The International Journal of Neuroscience*, *26*(3–4), 181–196. https://doi.org/10.3109/00207458508985616

Steinsträter, O., Wollbrink, A., & Pantev, C. (2007). Localisation of auditory evoked responses by SAM and event-related SAM. *International Congress Series*, *1300*, 177–180. https://doi.org/10.1016/j.ics.2007.03.013

Stewart, L. (2008). Do musicians have different brains? *Clinical Medicine*, *8*(3), 304–308. https://doi.org/10.7861/clinmedicine.8-3-304

Strait, D. L., & Kraus, N. (2011). Can you hear me now? Musical training shapes functional brain networks for selective auditory attention and hearing speech in noise. *Frontiers in Psychology*, *2*, 1–10. https://doi.org/10.3389/fpsyg.2011.00113

Strait, D. L., & Kraus, N. (2014). Biological impact of auditory expertise across the life span: Musicians as a model of auditory learning. *Hearing Research*, *308*, 109–121. https://doi.org/10.1016/j.heares.2013.08.004

Sutton, S., Braren, M., Zubin, J., & John, E. R. (1965). Evoked-potential correlates of stimulus uncertainty. *Science*, *150*(3700), 1187–1188. https://doi.org/10.1126/science.150.3700.1187

Tanaka, S., & Kirino, E. (2017). Reorganization of the thalamocortical network in musicians. *Brain Research*, *1664*, 48–54. https://doi.org/10.1016/j.brainres.2017.03.027

Taylor, J. R., Williams, N., Cusack, R., Auer, T., Shafto, M. A., Dixon, M., … Henson, R. N. (2017). The Cambridge Centre for Ageing and Neuroscience (Cam-CAN) data repository: Structural and functional MRI, MEG, and cognitive data from a cross-sectional adult lifespan sample. *NeuroImage*, *144*, 262–269. https://doi.org/10.1016/j.neuroimage.2015.09.018

Tewarie, P. K., Bright, M. G., Hillebrand, A., Robson, S. E., Gascoyne, L. E., Morris, P. G., … Brookes, M. J. (2016). Predicting haemodynamic networks using electrophysiology: The role of non-linear and cross-frequency interactions. *NeuroImage*, *130*, 273–292. https://doi.org/10.1016/j.neuroimage.2016.01.053

Tewarie, P. K., Hillebrand, A., van Dijk, B. W., Stam, C. J., O'Neill, G. C., Van Mieghem, P., … Brookes, M. J. (2016). Integrating cross-frequency and within band functional networks in resting-state MEG: A multi-layer network approach. *NeuroImage*, *142*, 324–336. https://doi.org/10.1016/j.neuroimage.2016.07.057

Tewarie, P. K., van Dellen, E., Hillebrand, A., & Stam, C. J. (2015). The minimum spanning tree: An unbiased method for brain network analysis. *NeuroImage*, *104*, 177–188. https://doi.org/10.1016/j.neuroimage.2014.10.015

Traud, A. L., Kelsic, E. D., Mucha, P. J., & Porter, M. A. (2008). Comparing Community

Structure to Characteristics in Online Collegiate Social Networks, *53*(3), 526–543. https://doi.org/10.1137/080734315

Tzourio-Mazoyer, N., Landeau, B., Papathanassiou, D., Crivello, F., Etard, O., Delcroix, N., … Joliot, M. (2002). Automated anatomical labeling of activations in SPM using a macroscopic anatomical parcellation of the MNI MRI single-subject brain. *NeuroImage*, *15*(1), 273–289. https://doi.org/10.1006/nimg.2001.0978

van den Heuvel, M., de Lange, S. C., Zalesky, A., Seguin, C., Yeo, T. B. T., & Schmidt, R. (2017). Proportional thresholding in resting-state fMRI functional connectivity networks and consequences for patient-control connectome studies: Issues and recommendations. *NeuroImage*, *152*, 437–449. https://doi.org/10.1016/j.neuroimage.2017.02.005

van Diepen, R. M., Miller, L., Mazaheri, A., & Geng, J. J. (2016). The role of alpha activity in spatial and feature-based attention. *ENeuro*, *3*(5), e0204-16.2016. https://doi.org/10.1523/ENEURO.0204-16.2016

Van Essen, D. C., Smith, S. M., Barch, D. M., Behrens, T. E. J., Yacoub, E., & Ugurbil, K. (2013). The WU-Minn Human Connectome Project: An overview. *NeuroImage*, *80*, 62–79. https://doi.org/10.1016/j.neuroimage.2013.05.041

Van Mieghem, P. (2011). *Graph spectra for complex networks*. Cambridge, UK: Cambridge University Press. https://doi.org/10.1016/S0065-2113(08)60505-2

Van Mieghem, P. (2016). Interconnectivity structure of a general interdependent network. *Physical Review E*, *93*(4), 1–11. https://doi.org/10.1103/PhysRevE.93.042305

Van Mieghem, P., Devriendt, K., & Cetinay, H. (2017). Pseudoinverse of the Laplacian and best spreader node in a network. *Physical Review E*, *96*(3), 032311. https://doi.org/10.1103/PhysRevE.96.032311

Van Veen, B. D., van Drongelen, W., Yuchtman, M., & Suzuki, a. (1997). Localization of brain electrical activity via linearly constrained minimum variance spatial filtering. *IEEE Transactions on Bio-Medical Engineering*, *44*(9), 867–880. https://doi.org/10.1109/10.623056

van Wijk, B. C. M. (2014). Thalamo-cortical cross-frequency coupling detected with MEG. *Frontiers in Human Neuroscience*, *15*(6), 884–890. https://doi.org/10.1038/nn.3101

van Wijk, B. C. M., Stam, C. J., & Daffertshofer, A. (2010). Comparing brain networks of different size and connectivity density using graph theory. *PLoS ONE*, *5*(10). https://doi.org/10.1371/journal.pone.0013701

Verleger, R. (1988). Event-related potentials and cognition: A critique of the context updating

hypothesis and an alternative interpretation of P3. *Behavioral and Brain Sciences*, *11*(03), 343–427. https://doi.org/10.1017/S0140525X00058015

Verleger, R. (2008). P3b: Towards some decision about memory. *Clinical Neurophysiology*, *119*(4), 968–970. https://doi.org/10.1016/j.clinph.2007.11.175

Verleger, R., Heide, W., Butt, C., & Kömpf, D. (1994). Reduction of P3b in patients with temporo-parietal lesions. *Cognitive Brain Research*, *2*(2), 103–116. https://doi.org/10.1016/0926-6410(94)90007-8

Verleger, R., Jaśkowski, P., & Wascher, E. (2005). Evidence for an integrative role of P3b in linking reaction to perception. *Journal of Psychophysiology*, *19*(3), 165–181. https://doi.org/10.1027/0269-8803.19.3.165

Vidaurre, D., Abeysuriya, R. G., Becker, R., Quinn, A. J., Alfaro-Almagro, F., Smith, S. M., & Woolrich, M. W. (2017). Discovering dynamic brain networks from big data in rest and task. *NeuroImage*, 1–11. https://doi.org/10.1016/j.neuroimage.2017.06.077

Vidaurre, D., Quinn, A. J., Baker, A. P., Dupret, D., Tejero-Cantero, A., & Woolrich, M. W. (2016). Spectrally resolved fast transient brain states in electrophysiological data. *NeuroImage*, *126*, 81–95. https://doi.org/10.1016/j.neuroimage.2015.11.047

Vrba, J., & Robinson, S. E. (2001). Signal processing in magnetoencephalography. *Methods (San Diego, Calif.)*, *25*(2), 249–271. https://doi.org/10.1006/meth.2001.1238

Walter, W. G. (1936). The location of cerebral tumors by electroencephalography. *Lancet*, *2*, 305–308. https://doi.org/10.1016/S0140-6736(01)05173-X

Wang, H, Douw, L., Hernández, J. M., Reijneveld, J. C., Stam, C. J., & Van Mieghem, P. (2010). Effect of tumor resection on the characteristics of functional brain networks. *Physical Review E - Statistical, Nonlinear, and Soft Matter Physics*, *82*(2), 21924. https://doi.org/10.1103/PhysRevE.82.021924

Wang, Huijuan, Li, Q., D'Agostino, G., Havlin, S., Stanley, H. E., & Van Mieghem, P. (2013). Effect of the interconnected network structure on the epidemic threshold. *Physical Review E*, *88*(2), 22801. https://doi.org/10.1103/PhysRevE.88.022801

Wang, Z., Wang, L., & Perc, M. (2014). Degree mixing in multilayer networks impedes the evolution of cooperation. *Physical Review E*, *89*(5), 52813. https://doi.org/10.1103/PhysRevE.89.052813

Ward, L. M. (2003). Synchronous neural oscillations and cognitive processes. *Trends in Cognitive Sciences*, *7*(12), 553–559. https://doi.org/10.1016/j.tics.2003.10.012

Watts, D. J., & Strogatz, S. H. (1998). Collective dynamics of'small-world' networks. *Nature*,

393(6684), 440–442. https://doi.org/Doi 10.1038/30918

Winterer, G., Mulert, C., Mientus, S., Gallinat, J., Schlattmann, P., Dorn, H., & Herrmann, W. M. (2001). P300 and LORETA: Comparison of normal subjects and schizophrenic patients. *Brain Topography*, *13*(4), 299–313. https://doi.org/10.1023/A:1011184814194

Wipf, D., & Nagarajan, S. (2009). A unified Bayesian framework for MEG/EEG source imaging. *NeuroImage*, *44*(3), 947–966. https://doi.org/10.1016/j.neuroimage.2008.02.059

Woolrich, M. W., Hunt, L. T., Groves, A., & Barnes, G. R. (2011). MEG beamforming using Bayesian PCA for adaptive data covariance matrix regularization. *NeuroImage*, *57*(4), 1466–1479. https://doi.org/10.1016/j.neuroimage.2011.04.041

Worsley, K. J., Marrett, S., Neelin, P., Vandal, A. C., Friston, K. J., & Evans, A. C. (1996). A unified statistical approach for determining significant voxels in images of cerebral activation. *Human Brain Mapping*, *4*, 58–73. https://doi.org/10.1162/NECO_a_00006-Arleo

Yeo, T. B. T., Krienen, F. M., Sepulcre, J., Sabuncu, M. R., Lashkari, D., Hollinshead, M., … Buckner, R. L. (2011). The organization of the human cerebral cortex estimated by intrinsic functional connectivity. *Journal of Neurophysiology*, *106*(3), 1125–1165. https://doi.org/10.1152/jn.00338.2011

Yordanova, J., & Kolev, V. (1998a). Event-related alpha oscillations are functionally associated with P300 during information processing. *Neuroreport*, *9*(14), 3159–3164. https://doi.org/10.1097/00001756-199810050-00007

Yordanova, J., & Kolev, V. (1998b). Single-sweep analysis of the theta frequency band during an auditory oddball task. *Psychophysiology*, *35*(1), 116–126. https://doi.org/10.1111/1469-8986.3510116

Yoshiura, T., Zhong, J., Shibata, D. K., Kwok, W. E., Shrier, D. A., & Numaguchi, Y. (1999). Functional MRI study of auditory and visual oddball tasks. *Neuroreport*, *10*(8), 1683–1688. https://doi.org/10.1097/00001756-199906030-00011

Yu, M., Engels, M. M. A., Hillebrand, A., Van Straaten, E. C. W., Gouw, A. A., Teunissen, C., … Stam, C. J. (2017). Selective impairment of hippocampus and posterior hub areas in Alzheimer's disease: An MEG-based multiplex network study. *Brain*, *140*(5), 1466–1485. https://doi.org/10.1093/brain/awx050

Yu, M., Hillebrand, A., Tewarie, P., Meier, J., van Dijk, B., Van Mieghem, P., & Stam, C. J. (2015). Hierarchical clustering in minimum spanning trees. *Chaos*, *25*(2), 1–10.

https://doi.org/10.1063/1.4908014

Zalesky, A., Fornito, A., & Bullmore, E. T. (2010). Network-based statistic: Identifying differences in brain networks. *NeuroImage*, *53*(4), 1197–1207. https://doi.org/10.1016/j.neuroimage.2010.06.041

Zatorre, R. J., Fields, R. D., & Johansen-Berg, H. (2012). Plasticity in gray and white: Neuroimaging changes in brain structure during learning. *Nature Neuroscience*, *15*(4), 528–536. https://doi.org/10.1038/nn.3045

Zatorre, R. J., & McGill, J. (2005). Music, the food of neuroscience? *Nature*, *434*(7031), 312–315. https://doi.org/10.1038/434312a

Zimmerman, J. E., Thiene, P., & Harding, J. T. (1970). Design and operation of stable rf-biased superconducting point-contact quantum devices, and a note on the properties of perfectly clean metal contacts. *Journal of Applied Physics*, *41*(4), 1572–1580. https://doi.org/10.1063/1.1659074

***